# POLITECNICO DI TORINO

**Master's Degree in Mechanical Engineering**


**Master's Degree Thesis**

# High-fidelity modeling of flight control actuators in the presence of degradations in the rod-end

**Supervisors**

**Prof. Massimo SORLI**

**Prof. Antonio Carlo BERTOLINO**

**Prof. Andrea DE MARTIN**

**Candidate**

**Ciro STAITI SELLITTO**

**April 2024**

**Abstract**

Rod-ends are mechanical components widely used in various mechanical applications, such as automotive and aerospace industries. In the aerospace field, they are of crucial importance for safety as they play a fundamental role in controlling flight surfaces. They are part of the kinematic chain responsible for moving the flight surfaces of airplanes or helicopters. Being vital for safety, numerous studies aim to calculate and measure their wear. In the specific case of this thesis, an analysis is conducted on a rod-end responsible for moving an airplane's flight surface. Aircraft flight control surfaces are essential for maneuverability in flight, allowing aircraft to perform roll, pitch, and yaw movements. In modeling, rod-ends can be considered as two concentric spheres with clearance between them. The inner sphere is free to move and come into contact with the outer sphere. During contact, the two spheres exchange a force perpendicular to the contact plane, known as the contact force, and a friction force parallel to the contact plane. The modeling of the contact force in this thesis utilizes the modeling studied by Lankarani and Nikravesh. The mechanism used to move the flight surface consists of an actuator, controlled by a jet-pipe servo-valve, which will actuate a connecting rod-crank mechanism. In particular, the connecting rod will be responsible for moving the outer ring of the rod-end. By moving, it will come into contact with the inner sphere, which is connected to the crank which is connect to the control surface, allowing it to rotate clockwise or counterclockwise. The modeling of the rod-end and its actuation system (excluding the actuator) have been the focal points of this thesis. Once the model was created, the operation of the model was first tested without considering the presence of the actuator, which was then added later to simulate more realistic operating conditions and to validate the complete model.

# Table of Contents

# List of Figures

# Chapter 1

# Flight control systems introduction

To control the direction of an aircraft, mobile surfaces, known as control surfaces, are utilized. Control surfaces are aircraft control systems, which allow to maneuver the aircraft with precision and reliability. A control system consist of:

- cockpit control
- sensors
- actuators which can be hydraulic, mechanical or electrical
- computers.

Control surfaces are used to deflect the air flow around the aircraft, facilitating rotations around the plane's center of mass. Aircraft control system consist in primary and secondary flight control, in figure number 1.1 the primary control surfaces are highlighted in red, while the secondary control surfaces are marked in blue. Primary control surfaces are the ailerons, the elevators and the rudder.

- Ailerons are used to rotate the plane, this movement is commonly referred to as *roll*, which describes the angle of this movement. The combination of roll and yaw (which is an aircraft movement described below) causes the aircraft to lean into turns. When the pilot want to turn right the right aileron moves up and the left aileron moves down, this action generates more lift on the left wing and less lift on the right wing, creating an imbalance in forces that enables the plane to roll to the right.
- Elevators allow the aircraft to climb or dive by an angle called *pitch* angle. To climb the elevators deflect the air flow to force the tail down and nose up

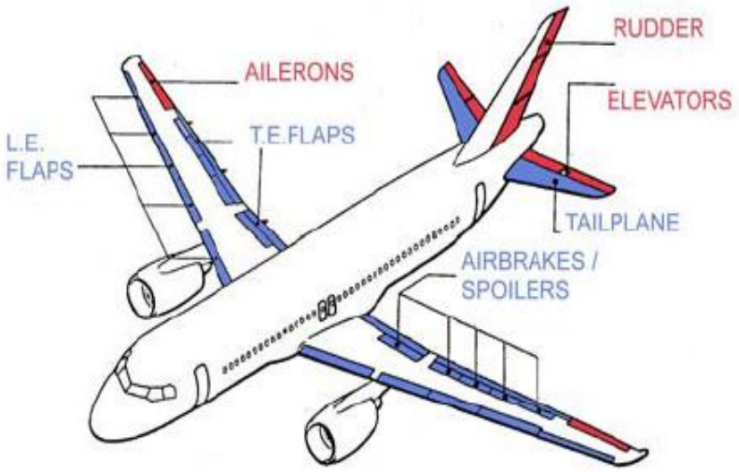


**Figure 1.1:** Control surface in an modern aircraft

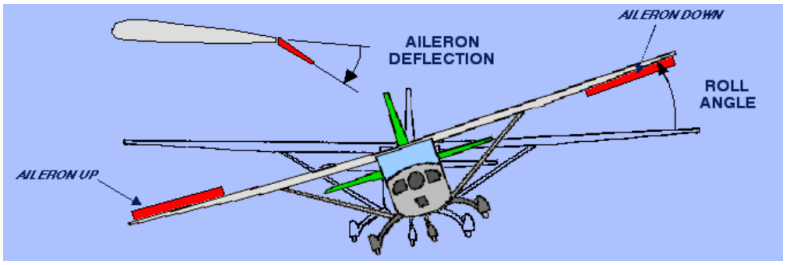


**Figure 1.2:** Roll angle

with an increasing pitch angle. Vice versa, to dive the elevators deflect the air flow to force the tail up and the nose down with a decreasing pitch angle.

- Rudders turn the aircraft right or left of an angle called *yaw* angle. The air flow causes a force which turns the aircraft in the direction of the rudder deflection. The pilot when he have to turns the plane use at the same time rudder and ailerons to produce a coordinate turn.

Meanwhile secondary flight controls consist of wing flaps, spoilers and trim systems.

- Flaps are the most common lift devices used in aerospace, they offer the advantage of achieving both high cruising speeds and low landing speeds, and they can be extended only when required. These surfaces are attached to edge of the wing and they increase lift and drag for any angle of attack.

- Spoilers are high drag devices used for reducing lift. they are deployed from the wing to spoil the smooth airflow. They are used for a more accurate

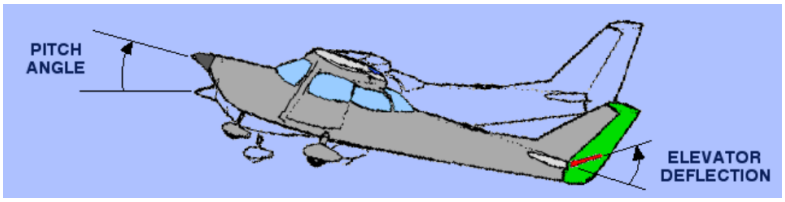


**Figure 1.3:** Pitch angle

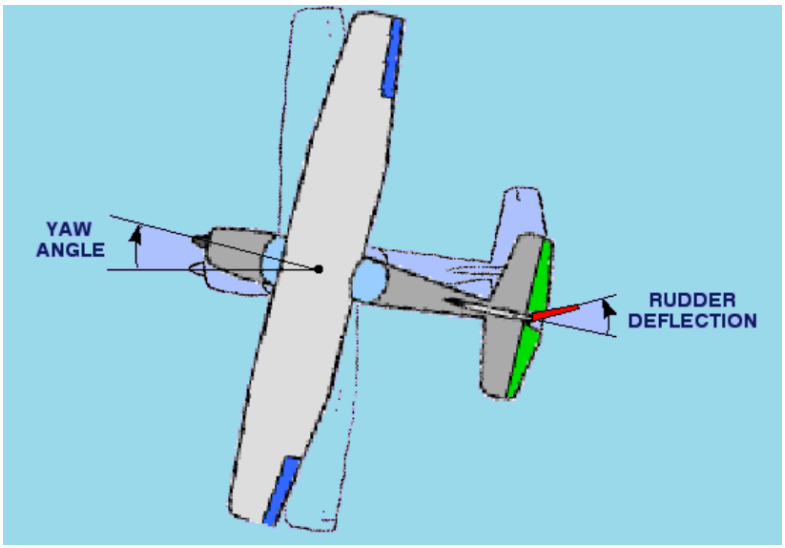


**Figure 1.4:** Yaw angle

landing and often they are used also for roll control because they eliminated adverse yaw.

- Trim systems are used to reduce the constant pressure that the pilot have to maintain on flight controls. They usually consist in a flight deck controls and small hinged devices attached to the trailing edge of one or more primary flight control.

The flight control surfaces are essential for maneuvering aircraft and are part of the so-called flight controls. These controls can be either fully manual or automatic. Currently, there is a growing trend towards having exclusively automatic flight controls, although they are also often used in conjunction with manual controls. Automatic controls allow the pilot to rest and reduce stress during less demanding flight phases or assist the pilot in maneuvering the aircraft in adverse weather conditions. The flight phase where automatic controls are primarily used is the cruise phase, which typically accounts for more than half of the total flight time. To ensure the correct positioning of flight control surfaces, each aircraft is equipped

with sensors that monitor their position, providing visual feedback to the pilot through dedicated instruments or to the automatic controller when the autopilot is engaged. A flight control system generally consists of the following elements: pilot input elements, system output elements, and intervening linkages.

- The pilot input elements, also known as primary flight controls, are the controls manipulated by the pilot to effect changes. There are three primary flight controls, corresponding to the main flight control surfaces, known as pitch, roll, and yaw control. In small aircraft, the pilot has a cockpit at their disposal, which includes a series of instruments, prominently featuring the aircraft's "yoke" and the pedal assembly located below it. The yoke has two modes of movement: it can be rotated left or right, similar to a steering wheel, to adjust the ailerons and thus the aircraft's roll angle. Additionally, the yoke can be pushed forward or pulled back to adjust the elevator and tilt the aircraft's nose up or down. Finally, under the yoke, there is the pedal assembly, whose movement allows for the adjustment of the rudder and thus the yaw angle.

- The system output elements are the flight surfaces that are controlled to maneuver the aircraft.

- The intervening linkages are all those elements that enable the actuation of the flight surfaces through the controls present in the pilot's cockpit. These systems can be entirely mechanical, hydraulic, or, the most modern ones, *fly-by-wire*.

All the possible intervening linkages are described below:

- Mechanical control systems: the control devices, which are in the aircraft cockpit, are directly connected to the control surfaces by a systems of rods, levers, cables and pulleys. According to the pilot control system changes angles of the control surfaces change in a proportional way, allowing for pitch, roll, and yaw maneuvers. This system is used only in small aircrafts because the complexity and the weight of the mechanical flight control system increases with the size of the aircraft. This system is shown in figure 1.5.

- Hydromechanical control systems: they are used to overcome the limitations of mechanical systems. The speed boost made more difficult to move the control surfaces due to the high aerodynamics forces. In these systems there are two main parts: a mechanical circuit which is very similar as in mechanical control systems and a hydraulic circuit which aim is to generate a bigger force in order to be able to move the control surface. The hydraulic circuit main component consist in a mechanically operated servo-valve. This system is shown in figure 1.6.

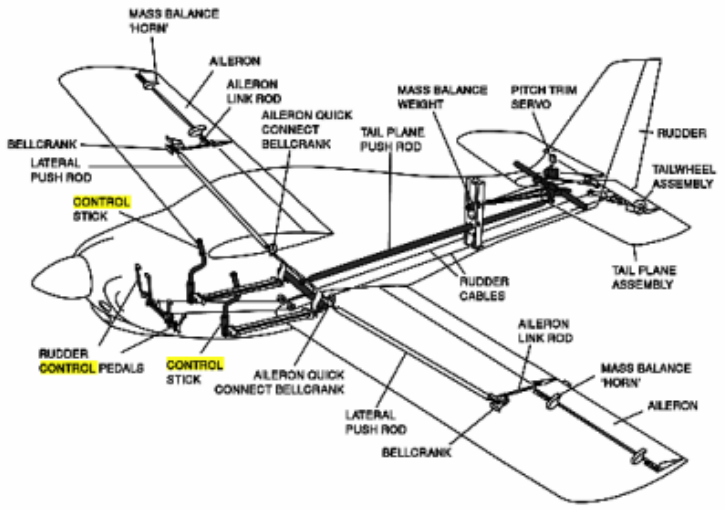


**Figure 1.5:** Mechanical flight control system

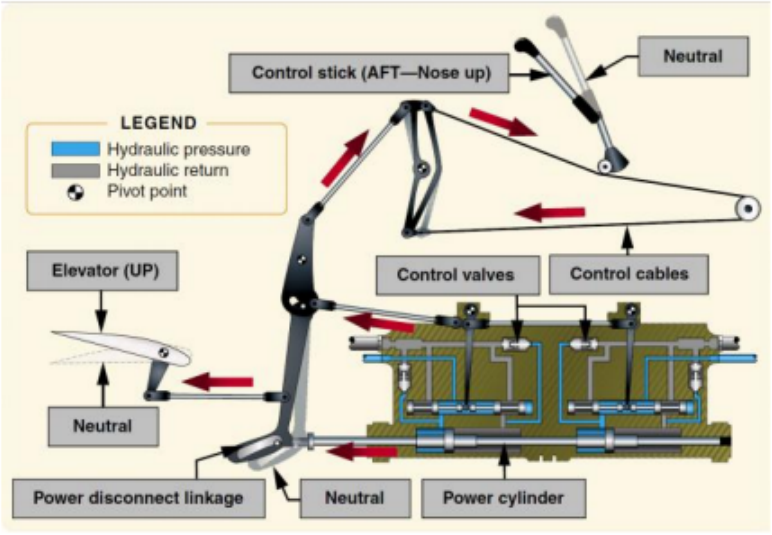


**Figure 1.6:** Hydromechanical flight control system

- Fly by wire control systems: They replaced all the conventional manual flight controls. The movement of the flight control is converted to an electronic signal which is transmitted by wire to an electronic interface that converts the signal to the actuator connected to the control surface. In the electronic interface there is a computer which is able to read the electronic signal and understand how to move the actuators to have the control surfaces as the pilot has ordered

at the system. The fly-by-wire technology is currently being surpassed by another technology called "fly-by-light," which utilizes optical fiber. Optical fiber offers several advantages over traditional electrical wiring, including immunity to electromagnetic fields commonly found in aircraft, higher data transmission capacity (essential in modern aircraft where the amount of data sent to actuators is increasing), lower maintenance costs, and reduced weight, resulting in lower fuel consumption for the aircraft. The elements that can be found in both fly-by-wire and fly-by-light systems are shown in figure 1.7.

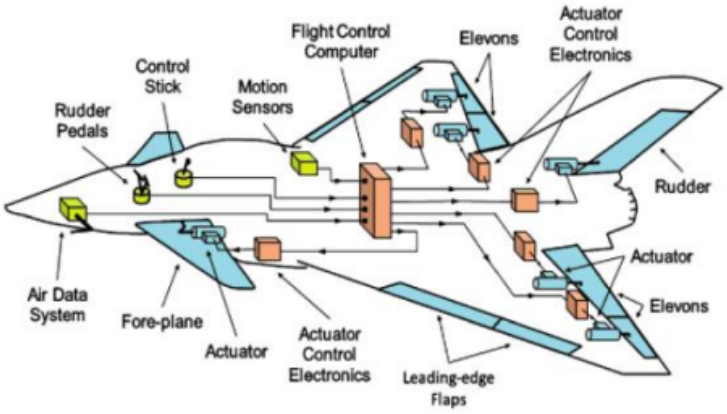


**Figure 1.7:** Main element of a fly-by-wire and fly-by-light flight control system

# Chapter 2

# Rod-ends introduction

Rod-ends are crucial mechanical components in flight control surfaces, they connect the actuator with the kinematics of the surface. They are widely used also in other mechanical applications such as automotive. So they often perform critical operations which directly impact safety, therefore it's very important to study them in order to prevent failure and potential incidents. Before start seeing the failure modes of rod-ends it's important to see how they can be subdivided. Although they may appear all the same at first glance, this it's not true. Initially they can be classified into two and three pieces rod-end[1]:

- Two pieces rod-end: the body is formed around the sphere so the race is part of the body. They are generally less expensive.
- Three pieces rod-end: they have better precision and they are called "aircraft" rod-ends for the field they are used in. Here the housing is formed around the sphere and then the housing is forced into the body.

Rod-ends have different failure modes and the most common are[2]:

- Crack opening: a crack is generated in the weak part and, then during the normal operation of the system, can growth till the complete component failure.
- Lubricant degradation: this mode lead to metal metal contact which increase the force friction in the rod-end, due to the increase of the friction the piston rod can be affected by plastic deformation. There are two different type of lubrication available[3]:
  - grease: provides a lubrication meatus but there may be leakage through the rod-end.

**Figure 2.1:** Two pieces rod-end

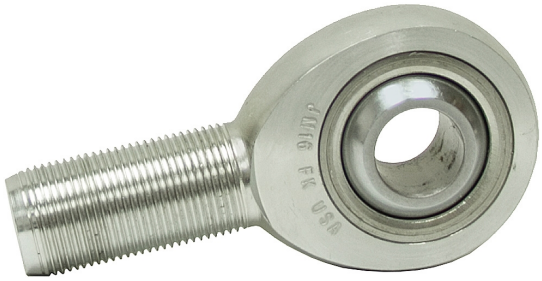

**Figure 2.2:** Three pieces rod-end

  - fabric liner: this allow rod-end to be self-lubricated. Normally a first fiber ensure strength and bounding properties and then a second component (like polymer) is used to reduce wear and friction.

- Wear of the internal surface: is the most common mode which leads to the increasing of the backlash. The increasing of the backlash cause an accuracy reduction in the positioning of the control surface.

- Surface denting.

In literature there are a lot of studies on rod-ends because of their versatility of use. There are also a lot of articles which investigate the failure causes such their important role in safety. Below there are some articles regarding studies conducted in order to provide a brief state of the art.

Before their commissioning rod-ends should be tested in order to understand the service life time and prevent failure, it's important to keep in mind that activate control surfaces of both airplane and helicopters are crucial during the flight. Wang et al.[4] developed a new testing machine for testing rod-ends used in helicopters. These particular rod-ends are known as self-lubricating due to their solid lubrication. In the context of helicopters, rod-ends are utilized to control the movement of the main rotor. In their work, Wang employs a novel type of life testing machine based on the 3-(R)RSS-(R)RRS-PS parallel mechanism. The pitch link, which connects the swash plate to the pitch swing arm, has two rod-ends attached to its terminal parts, allowing for movement in space. Controlling both pitching and flapping motion makes the movement of the rod-end complex and diverse.

Therefore, a machine capable of evaluating the lifetime of the testing bearing is essential. To create this testing machine, a mechanism was developed to simulate the movement that occurs within the main rotor structure, as illustrated in the figure 2.3. To calculate the lifetime of the tested rod-end and obtain information

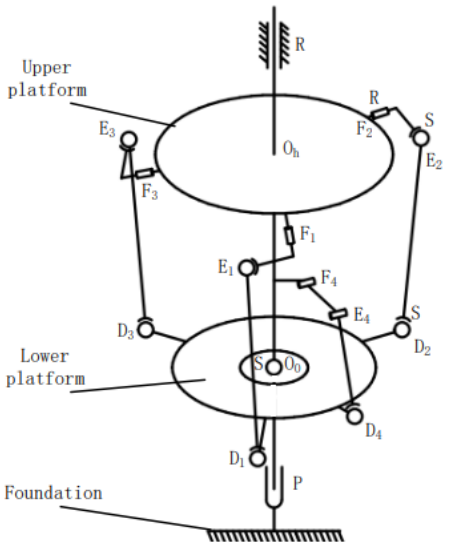


**Figure 2.3:** Scheme of the testing machine

about wear, a temperature sensor is used. This temperature sensor is inserted inside the connecting pin of the rod-end to measure the temperature at the center of the system. By monitoring the temperature trend, it becomes possible to identify excessive wear when the temperature rises abruptly, indicating that the solid lubricant has been depleted and the testing bearing is at risk of failure.

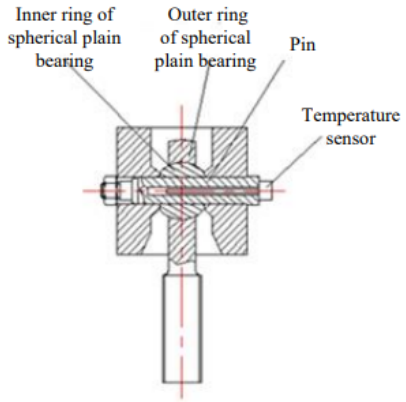


**Figure 2.4:** Housing of the temperature sensor

Wear in rod-ends is of great significance, and historically, it was a closely monitored parameter, as evident here [5]. The method for detecting wear was rudimentary and involved a pin mechanically inserted into the outer ring so that it could come into contact with the inner ring, as shown in the figure 2.5. The lower

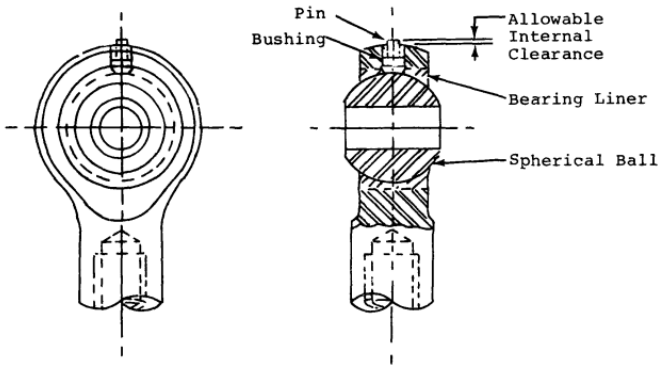


**Figure 2.5:** Scheme of the pin inserted in the rod-end

end of the pin was made of a softer material, and once the pin no longer protruded, it indicated that the rod-end needed replacement.

Wear affects not only the function of the movement of the two sphere of the rod-end but also the operating condition of oil seals as it can be seen form the article written by Zhang et al[6]. In his work, Zhang studies the operation of grease-lubricated rod-end seals. The operating conditions of the seals are greatly influenced by wear and temperature increase. Temperature, as well as vibrations, are caused by the operation of rod-ends, and in his study, Zhang correlates seal wear with the performance of rod-ends. The friction between the oil seal and the rotating ring is the primary factor in the temperature rise.

Another important thing in rod-ends is how the friction reduction between the two ring is made, as said before the lubrication can be made with grease or can be solid and for each situation one can be chosen over the other. An example is shown in the article written by Kim[7]. Kim in his work analyze a rod-end present in the elevation driving mechanism of a battle tank. For this application rod-end must be self-lubricated because at very low operating speed it can't be possible generate the necessary pressure for a non solid lubrication. The conventional metal spherical bearing on the race surface has $MoS_2$ as a solid lubricant, but due to the heavy load and low speed all the coating gets removed lead to a metal to metal contact (shown in figure 2.6). To replace the conventional steel spherical bearing material was selected the carbon-phenolic composite material. To avoid the need for machining and assembly procedures for the composite race, a custom compression mold was engineered. This mold allowed the direct molding of the composite race onto the

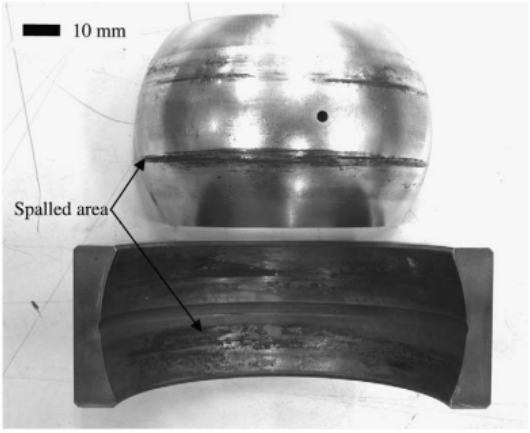


**Figure 2.6:** Damage of the sphere caused by the metal to metal contact

ball's surface with an exact clearance, eliminating the necessity for machining. This was crucial as machining the composite material not only increased manufacturing costs due to excessive tool wear but also compromised the material's mechanical properties through fiber breakage.

About the failure modes of rod-end there are a lot of studies and analysis about failures happened during operating condition in various applications. An example, happened in aerospace sector, is the analysis conducted by Asi and Yesil[8]. They examined a failed piston rod-end employed in a hydraulic actuating system for a civil landing gear. The rod-end under consideration fails due to a stress raiser owing to an incorrect assembly which leads to a fatigue failure. To underscore the diverse application of Rod-ends in various industries, there is also a paper written by Narvydas et al.[9] which talk about a company producing hydraulic cylinders for live floor installations who reported several failure in the rod-end.

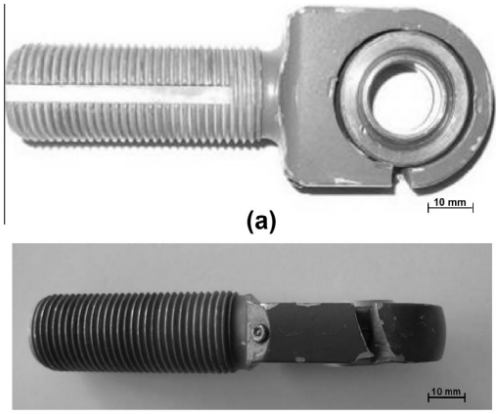


**Figure 2.7:** Failed rod-end of the civil landing gear

# Chapter 3

# Contact and kinematic model

Rod-ends can be modeled as spherical joints; in fact, they are spherical joints with a threaded rod used to connect them to actuators. In this thesis, the modeled spherical joint has clearance, which means that the two bodies become free to move relative to each other. Unlike the ideal joint, a spherical joint with clearance does not constrain any degree of freedom. The dynamics of the joint are controlled by contact-impact forces, which result from the collision between the connected bodies. Therefore, this type of joint is also referred to as a 'force-interaction joint.' These joints consist of two spheres, one inside the other, where the inner sphere, called the 'ball,' can move freely, and the outer sphere is known as the 'socket.' More precisely, the ball can have three motion modes[10]:

- Permanent contact or following mode
- Free flight mode
- Impact mode.

In the following and impact mode, the ball and the socket are in contact, and there is a sliding motion relative to each other. For a clearer understanding, refer to the figure 3.1.

So a model of a spherical joint should be divided in two parts, a kinematics part and a contact part, a simple representation of the model is shown in the figure 3.2. The kinematic block is employed to calculate all the parameters necessary for determining the positions and orientations of both the ball and the socket. These parameters are essential for assessing whether there is contact and for determining the magnitude of the forces involved during the contact. As a result, the model developed for this thesis comprises two kinematic blocks, one for the socket and

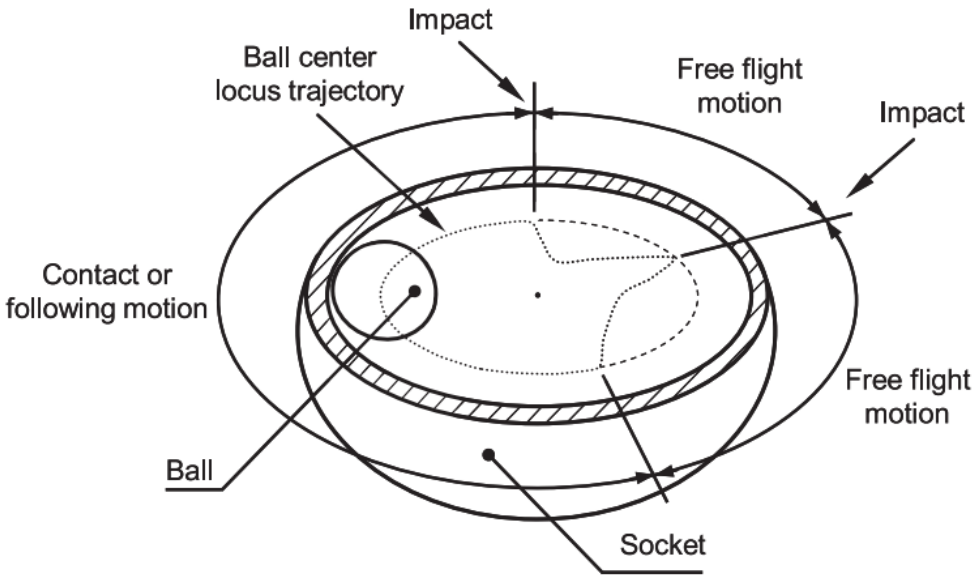


**Figure 3.1:** Motion modes of a spherical joint with clearance

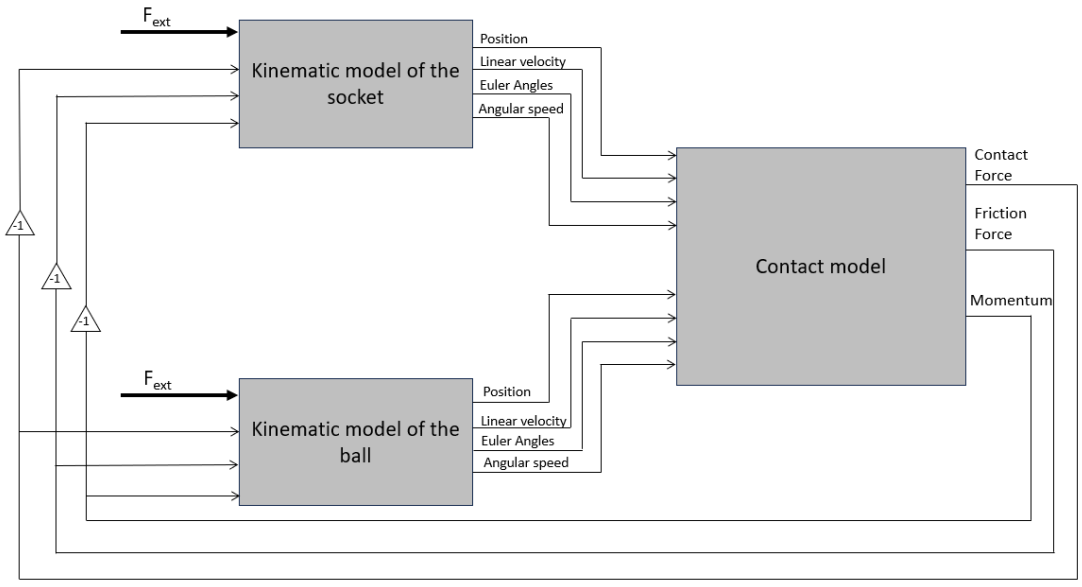


**Figure 3.2:** Simple representation of the model

one for the ball, and a contact block. In this section, we will describe the contact block first, followed by the kinematic blocks, which are identical.

## 3.1 Contact model

To model a spherical joint, as is shown before, it's important to understand in which motion mode the ball is. First of all, it is essential to comprehend the conditions that lead to contact between the two spheres. These conditions depend on the clearance and the joint's eccentricity at any given time. Eccentricity is a vector that defines the distance between the center of the ball and the center of the socket, as illustrated in the figure 3.3. The red sphere is the ball and the black sphere is

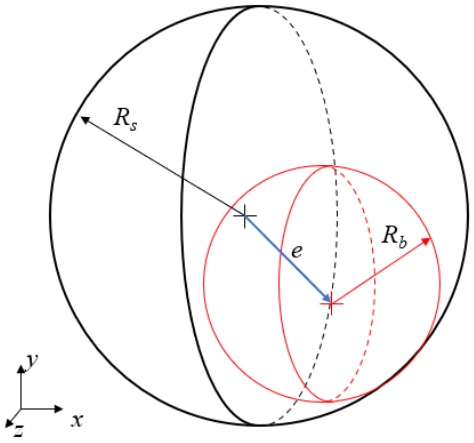


**Figure 3.3:** Eccentricity vector

the socket, the eccentricity vector is shown in blue and as can be seen from the figure 3.3, the magnitude can be calculated as follows:

$$e = \sqrt{(x_s - x_b)^2 + (y_s - y_b)^2 + (z_s - z_b)^2} \tag{3.1}$$

where the subscript '$s$' indicates the socket and the subscript '$b$' indicates the ball. If the clearance is defined by $\epsilon$ than there is contact when:

$$F_N \begin{cases} > 0 & \text{if} \quad e \geq \epsilon \\ = 0 & \text{if} \quad e < \epsilon \end{cases} \tag{3.2}$$

With the two spheres in contact, a contact force and a frictional force are developed as shown in the figure 3.4, for simplicity of representation in 2D. The most simple theory that describe the contact force is the Hertz theory [11]. The contact analyzed in the Hertz theory is a problem of non linear elasticity, it means that there isn't permanent deformation during contact and the formulation is as follow:

$$F = K\delta^n \tag{3.3}$$

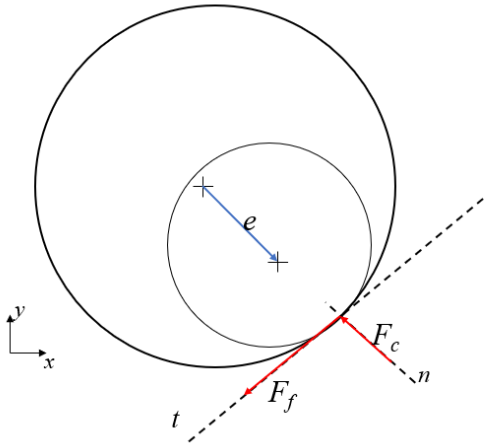


**Figure 3.4:** Contact and friction force

Where $\delta$ is the relative penetration of the two sphere, $n$ is equal to 3/2 since the contact can be model between two sphere and $K$ is a parameter that depends on the material property and it's calculate as follow:

$$K = \frac{4}{3\pi(\sigma_i - \sigma_j)} \left[ \frac{R_i - R_j}{R_i + R_j} \right]^{1/2} \tag{3.4}$$

where the material parameters $\sigma$ are:

$$h = \frac{1 - \nu^2}{\pi E} \tag{3.5}$$

$\nu$ and $E$ are respectively the Poisson's Ratio and the Young modulus. Use equation number (3.3) to calculate the contact force, however, it's not correct because this would suggest that there isn't dissipated energy during the impact process. The energy loss can be assumed that is caused by a linear damping function, so the contact force became:

$$F = K\delta^n + D\dot{\delta} \tag{3.6}$$

where

$$D = \mu\delta^n. \tag{3.7}$$

The parameter $\mu$ can be called as "hysteresis damping factor". An impact can generally be considered to occur in two phases: the compression phase and the restitution phase. During the compression phase, the two solids deform theirself along the normal direction, and the relative velocity of the contact point along the contact direction is reduced to zero. This marks the end of the compression phase

and the occurrence of maximum compression. Subsequently, the restitution phase commences and continues until the two solids are separated. Equation number (3.6) can be employed to describe both phases of an impact, as studied by Lankarani and Nikravesh[12]. When equation number (3.6) is plotted with penetration on the x-axis, it results in a hysteresis loop, as depicted in the figure 3.5. In this figure the

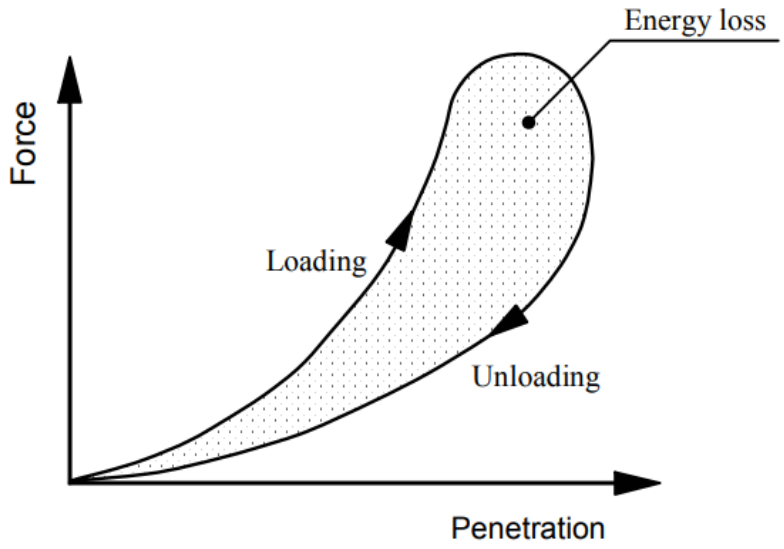


**Figure 3.5:** Hysteretic loop

area of the loop is equal to the energy loss during an impact. So the damping factor calculated by Lankarani and Nikravesh, which is used in this thesis, is formulated as follow:

$$\mu = \frac{3K(1-e^2)}{4\dot{\delta}^{(-)}} \tag{3.8}$$

where $e$ is a coefficient of restitution which is defined as the ratio of relative departure velocity to the relative approach velocity of the sphere in the direction of the contact, $\dot{\delta}^{(-)}$ is the initial indentation velocity. All the calculus done to reach the formulation of the "hysteresis damping factor" of the equation number (3.8) are shown in the appendix A where a short review of the article in the reference [12] is done in order to have a motivation of the use of a damping factor which is not constant.

For the friction force the thesis work carried out by Bertolino[13] is followed. In his PHD Thesis he presented two models to calculate the friction force, an empirical model and a lubrication model. For this thesis, the empirical model was selected due to its lower computational requirements, given that an overly detailed and complex description of friction was not needed. The empirical model consists of an a equivalent function which relates the sliding velocity to the friction coefficient.

The formulation is as follow:

$$\mu = \begin{cases} \text{step}(\nu_{rel}, \nu_{st}, -(\mu_{st} - \mu_v \nu_{st}), \nu_{st}, \mu_{st} - \mu_v \nu_{st}) + \mu_v \nu_{rel} & \text{if} \quad 0 \leq \nu_{rel} \leq \nu_{st} \\ \text{step}(\nu_{rel}, \nu_{st}, \mu_{st} - \mu_v \nu_{st}, \nu_{dyn}, \mu_{dyn} - \mu_v \nu_{dyn}) + \mu_v \nu_{rel} & \text{if} \quad \nu_{rel} > \nu_s t \end{cases} \tag{3.9}$$

where the step function is:

$$\text{step}(x, x_0, f_0, x_1, f_1) = \begin{cases} f_0 + (f_1 - f_0)\left[3\left(\frac{x-x_0}{x_1-x_0}\right)^2 - 2\left(\frac{x-x_0}{x_1-x_0}\right)^3\right] & \text{if} \quad x_0 < x < x_1 \\ f_0 & \text{if} \quad x \leq x_0 \\ f_1 & \text{if} \quad x \geq x_1 \end{cases} \tag{3.10}$$

$\nu_{rel}$ is the magnitude of the relative sliding speed, $\nu_{st}$ is the static friction threshold speed, $\nu_{dyn}$ is the dynamic friction threshold speed and $\mu_v$ is the viscous coefficient. The friction force is so calculated as:

$$F_{fric} = \mu F_c \tag{3.11}$$

where $F_c$ is the contact force found in the equation number (3.6). The magnitude of the relative sliding speed is calculated as it can be seen in the figure number 3.6 where $P$ is the contact point between the two sphere, $\omega$ is the angular velocity and $V$ is the linear velocity. The sliding speed is the combination of the linear velocity of the sphere and the tangential velocity caused by the angular velocity, however the relative speed required to have the friction coefficient is only the the tangential component so a further step it's necessary. All the calculus are reported below for clarity:

$$\vec{v_{rel}} = \vec{\omega} \times \vec{r} + \vec{v} \tag{3.12}$$

$$\vec{v_{rel,t}} = \vec{v_{rel}} - v_{rel}\vec{n} \tag{3.13}$$

The effective sliding velocity is the sliding velocity of the inside sphere minus the sliding velocity of the outside sphere because the socket is free to move and it's not constrained.

### 3.1.1 Simulink contact model

In this subsection the model made on Simulink is shown in order to see how the contact equations of the previous section are integrated into the software; the complete contact model is shown in the figure 3.7. The green box show the subsystem used to calculate eccentricity and $\delta$ of the equation number 3.6 needed then for the calculation of the "spring" part of the contact force highlight with the red box. Eccentricity and $\delta$ are also inputs for the block used to calculated the "damping" part of the contact force shown in the blue box. Before adding the two

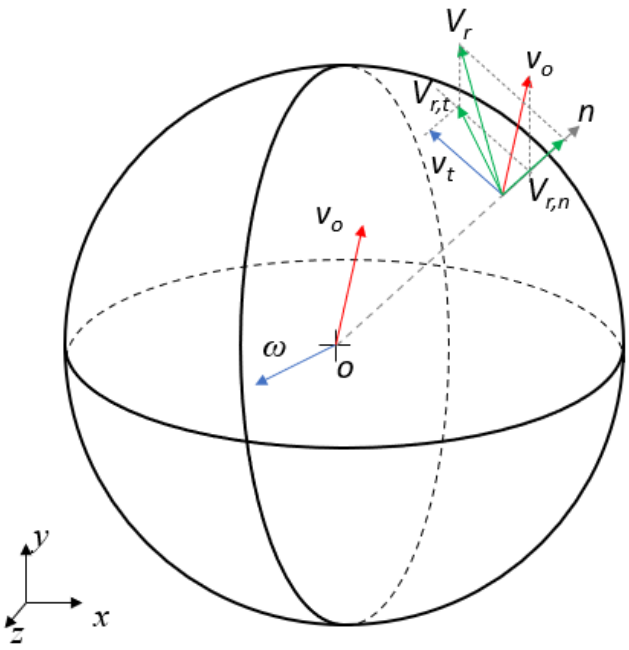


**Figure 3.6:** Diagram for calculating the sliding speed

contributions of the contact force, an additional step is required. It is necessary to ensure that the damping contribution does not generate a contact force when contact is not actually present. Indeed, even in the absence of contact, a force can be generated by the difference in velocity between the two spheres. To avoid this issue, a block has been introduced that returns the minimum value of the two force contributions. This implies that in the absence of contact, both the spring force contribution and the damping contribution are null. To express this step in the form of an equation, see below:

$$F = k\delta^n + \min\left(c\dot{\delta}, k\delta^n\right) \tag{3.14}$$

The last two boxes, the purple one and the orange one, represent respectively the subsystem used to found the relative speed of the two sphere and the subsystem where the friction force is calculated. So in the purple box there are all the blocks necessary to compute the relative sliding speed of the equation number 3.12 and 3.13 and in the orange box, instead, there are all the blocks needed to calculate the friction coefficient, here there is the Lookup-table used to have in Simulink the friction formulation of the equation number 3.9 and 3.10. It should be noted that in this model there is one output for the friction force and two output for the momentum generated by the friction force because the two sphere have different

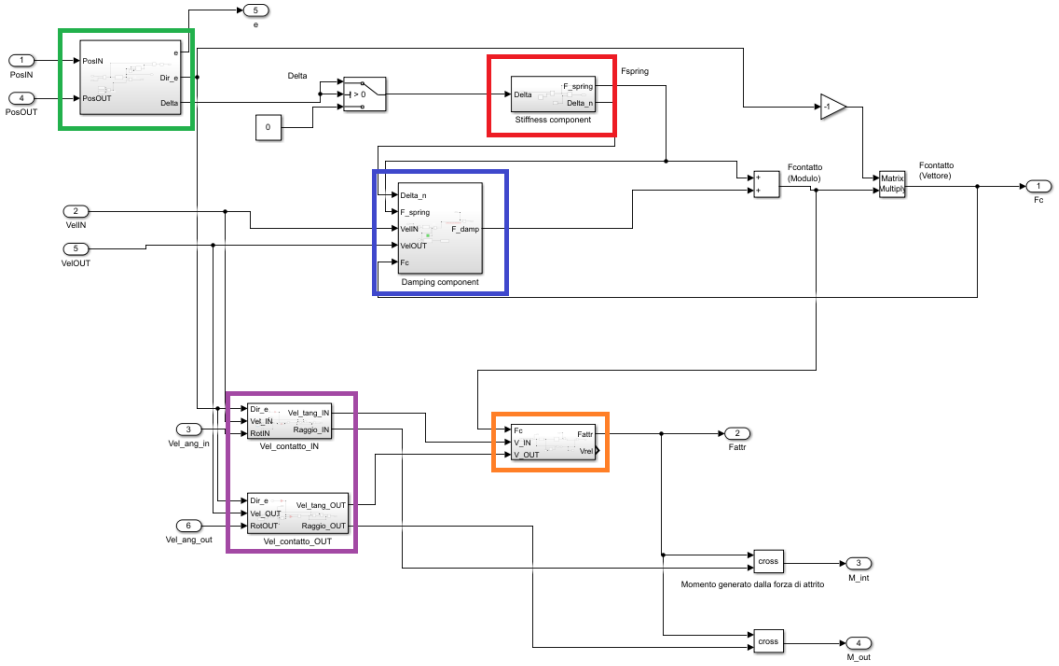


**Figure 3.7:** Simulink contact model

radii. In figure 3.7, once $\delta$ is obtained there is a switch which role is to compute the force only when there is contact, the switch pass the value of $\delta$ only when $\delta > 0$ otherwise the switch allow 0 to pass. The expression $\delta > 0$ means the presence of contact because its formulation is the following according to the equation number 3.2:

$$\delta = e - \epsilon \tag{3.15}$$

$\dot{\delta}$ used in the equation number 3.6 is calculated inside the subsystem highlight with the blue box. Here there is a subsystem, highlighted in red, where the damping factor is found (figure 3.8). The subsystem of the damping factor can be seen in figure 3.9 and 3.10. The system shown in figure 3.10 is used to calculated $\dot{\delta}^{(-)}$ which is the relative velocity the instant just before the impact. The system, when the contact force is zero, store into the variable `"Delta_d0"` the value of the velocity; the value is stored until the contact end, in fact when the contact force is not zero the switch allow to store for each time step the same value of `"Delta_d0"`. Then the value of `"Delta_d0"` is used in the figure 3.9 to calculate the damping factor subsequently used to calculated the damping part of the contact force.

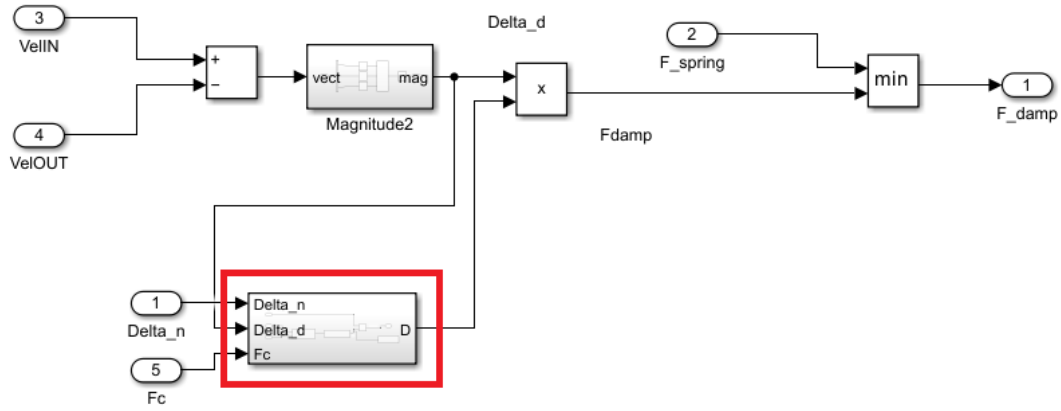


**Figure 3.8:** Damping force subsystem

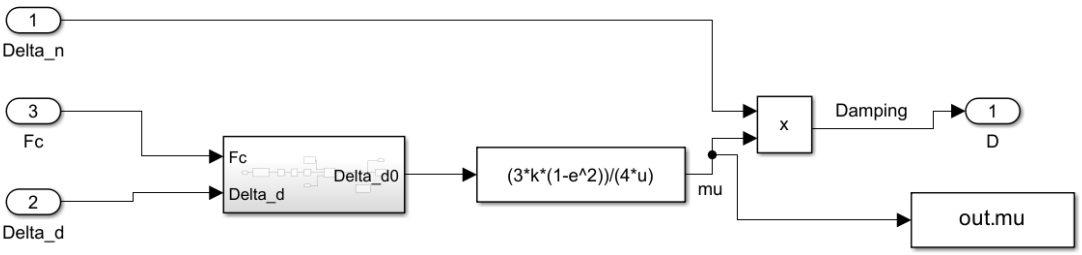


**Figure 3.9:** Damping factor block

## 3.2 Kinematic model

Everything we've talked about so far is present in the contact block of the Simulink model created for this thesis. However, all the outcomes from this block cannot be achieved without the involvement of a kinematics block. There are two kinematics blocks in the model, one for each sphere, and they allow for the calculation of the position and velocity of the solids, which are subsequently used in the contact block.

All the kinematic quantities for a 3D rigid body can be expressed using two or more reference systems, usually the body quantities are expressed related to an inertial frame and to a body frame. An inertial frame is a reference systems that doesn't change during time, it's called also "fixed frame", meanwhile a body frame is a frame which follow the orientation of the body in the spatial orientation, typically the origin of the frame is in the center of mass of the body. To make it clear there

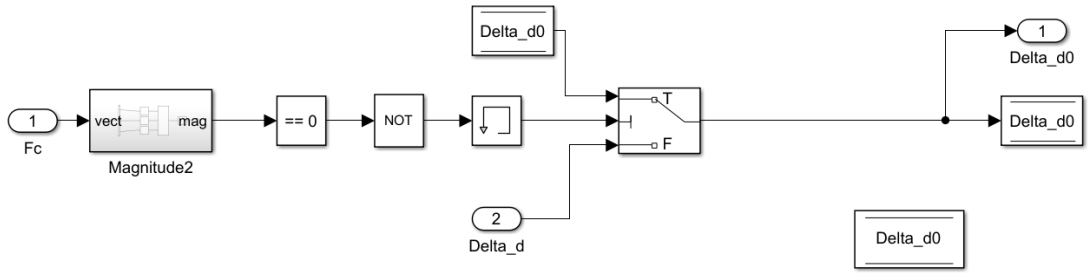


**Figure 3.10:** Damping factor block

is a representation of the two frame in the figure 3.11 where $\hat{b}$ is the body frame and $\hat{n}$ is the inertial frame. It is important, therefore, to describe the kinematic

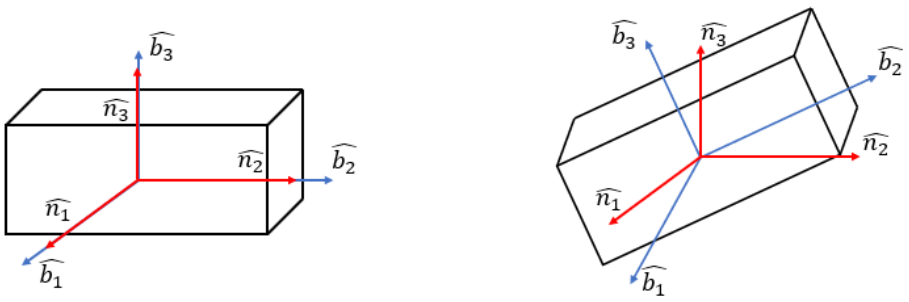


**Figure 3.11:** Inertial and body frame for a 3D body

quantities in both reference systems and be able to pass from one reference system to the other. To do so, it is necessary to project the mobile reference system onto the fixed one, as illustrated in the figure 3.12. Mathematically, this is expressed in the following way:

$$\hat{b_1} = \underbrace{(\hat{b_1} \cdot \hat{n_1})}_{\cos\alpha_{11}} \hat{n_1} + \underbrace{(\hat{b_1} \cdot \hat{n_2})}_{\cos\alpha_{12}} \hat{n_2} + \underbrace{(\hat{b_1} \cdot \hat{n_3})}_{\cos\alpha_{13}} \hat{n_3} \tag{3.16}$$

which expressed in vector form became:

$$\hat{b_1} = \begin{bmatrix} \cos\alpha_{11} & \cos\alpha_{12} & \cos\alpha_{13} \end{bmatrix} \begin{bmatrix} \hat{n_1} \\ \hat{n_2} \\ \hat{n_3} \end{bmatrix} \tag{3.17}$$

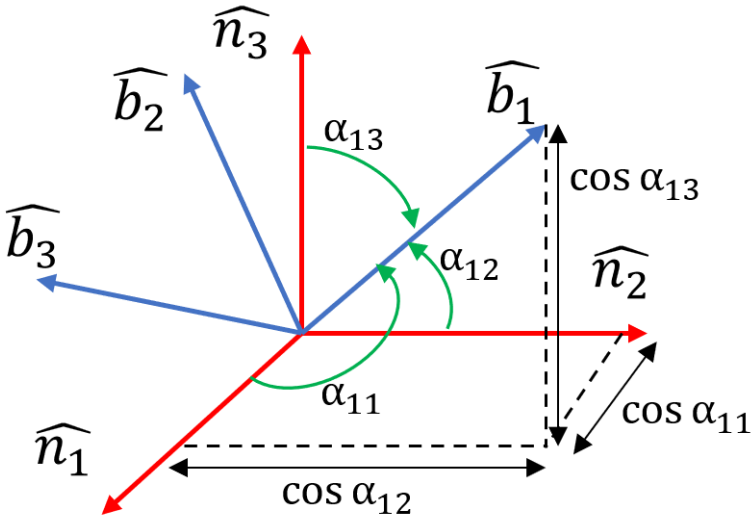


**Figure 3.12:** Projection of the mobile reference system onto the fixed one

Repeating the same steps for $\hat{b_2}$ and $\hat{b_3}$ a matrix is obtained.

$$\begin{bmatrix} \hat{b_1} \\ \hat{b_2} \\ \hat{b_3} \end{bmatrix} = \underbrace{\begin{bmatrix} \cos\alpha_{11} & \cos\alpha_{12} & \cos\alpha_{13} \\ \cos\alpha_{21} & \cos\alpha_{22} & \cos\alpha_{23} \\ \cos\alpha_{31} & \cos\alpha_{32} & \cos\alpha_{33} \end{bmatrix}}_{=[C]} \begin{bmatrix} \hat{n_1} \\ \hat{n_2} \\ \hat{n_3} \end{bmatrix} \tag{3.18}$$

The obtained matrix is called as "direction cosine matrix" or as "rotational matrix". In equation number 3.18 the matrix is used to pass from the body frame to the inertial frame, to achieve the reverse step the inverse of the matrix must be computed which is equal to the transpose matrix $[C]^{-1} = [C]^T$.

$$\left\{\hat{b}\right\} = \left[C\right]\left\{\hat{n}\right\} \tag{3.19}$$

As the matrix in equation number 3.18 is defined, it has nine different entries which are a lot, so it's important to parametrize the direction cosine matrix with the three Euler angles. Euler angles are three successive rotation of the body around the x,y and z axis, this three rotation allow to define the orientation of the body. In aerospace the three Euler angles are usually called as Yaw, Pitch and Roll and correspond respectively to a first rotation around the third axes, a second rotation around the second axis and a third rotation around the first axis. Each rotation generates a rotation matrix as it can be seen below. The initial configuration can be seen in the figure 3.13, here the blue frame is the body frame while the red frame is the Earth frame, it should be specified that the drawing represents only

the unit vectors even if they have different lengths which have been made to have a better view. The first rotation around the third axis change the body frame

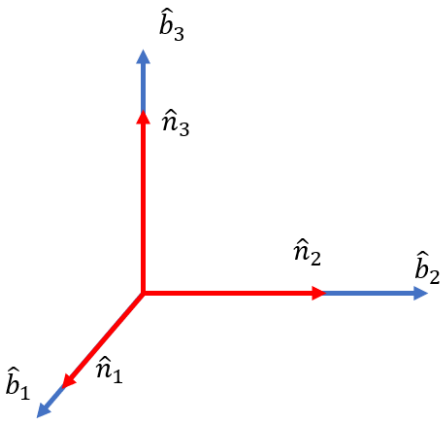


**Figure 3.13:** Body and Earth frame

orientation as in figure 3.14 and this rotation generate the following matrix.

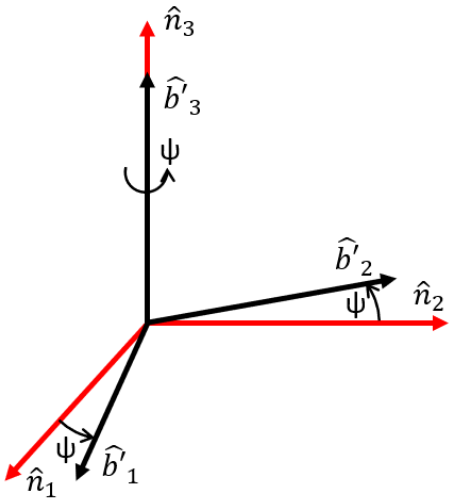


**Figure 3.14:** Rotation around the third axes

$$\begin{Bmatrix} \hat{b}'_1 \\ \hat{b}'_2 \\ \hat{b}'_3 \end{Bmatrix} = \underbrace{\begin{bmatrix} \cos\psi & \sin\psi & 0 \\ -\sin\psi & \cos\psi & 0 \\ 0 & 0 & 1 \end{bmatrix}}_{[M_3(\psi)]} \begin{Bmatrix} \hat{n}_1 \\ \hat{n}_2 \\ \hat{n}_3 \end{Bmatrix} \tag{3.20}$$

Doing the same steps with the second rotation we obtained the orientation show in figure 3.15 and the following matrix.

$$\begin{Bmatrix} \hat{b}_1'' \\ \hat{b}_2'' \\ \hat{b}_3'' \end{Bmatrix} = \underbrace{\begin{bmatrix} \cos\theta & 0 & -\sin\theta \\ 0 & 1 & 0 \\ \sin\theta & 0 & \cos\theta \end{bmatrix}}_{[M_2(\theta)]} \begin{Bmatrix} \hat{b}_1' \\ \hat{b}_2' \\ \hat{b}_3' \end{Bmatrix} \tag{3.21}$$

Lastly, with the third and last rotation the orientation is figure 3.16 is obtained

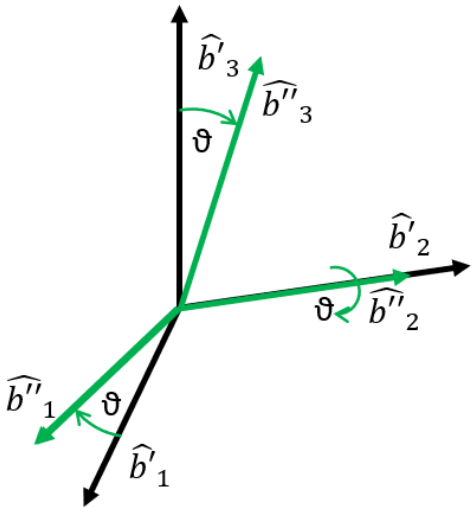


**Figure 3.15:** Rotation around the second axes

and the following matrix describe the rotation.

$$\begin{Bmatrix} \hat{b}_1 \\ \hat{b}_2 \\ \hat{b}_3 \end{Bmatrix} = \underbrace{\begin{bmatrix} 1 & 0 & 0 \\ 0 & \cos\phi & \sin\phi \\ 0 & -\sin\phi & \cos\phi \end{bmatrix}}_{[M_1(\phi)]} \begin{Bmatrix} \hat{b}_1'' \\ \hat{b}_2'' \\ \hat{b}_3'' \end{Bmatrix} \tag{3.22}$$

The product of the three rotation matrix obtained with the three rotation generates a rotation matrix which describe every orientation of the body in the 3D space, this means also that the product of the three matrix is also the rotational matrix that can be used to pass from the inertial frame to the body frame; all the calculus are reported below.

$$\left\{\hat{b}'\right\} = \left[M_3(\psi)\right]\left\{\hat{n}\right\} \tag{3.23}$$

$$\left\{\hat{b}''\right\} = \left[M_2(\theta)\right]\left\{\hat{b}'\right\} \tag{3.24}$$

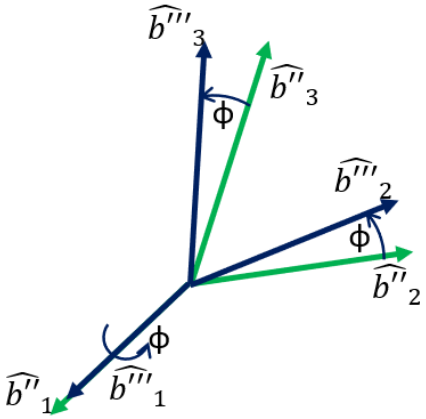


**Figure 3.16:** Rotation around the first axes

$$\begin{aligned}\left\{\hat{b}\right\} &= \left[M_1(\phi)\right]\left\{\hat{b''}\right\} \\ &= \left[M_1(\phi)\right]\left[M_2(\theta)\right]\left\{\hat{b'}\right\} \\ &= \underbrace{\left[M_1(\phi)\right]\left[M_2(\theta)\right]\left[M_3(\phi)\right]}_{[C(\psi,\theta,\phi)]}\left\{\hat{n}\right\}\end{aligned} \tag{3.25}$$

Where the $[C(\psi, \theta, \phi)]$ matrix is:

$$\begin{bmatrix} \cos\psi\cos\theta & \sin\psi\cos\theta & -\sin\theta \\ \cos\psi\sin\theta\sin\phi - \cos\phi\sin\psi & \sin\psi\sin\theta\sin\phi + \cos\phi\cos\psi & \cos\theta\sin\phi \\ \cos\phi\sin\theta\cos\psi + \sin\phi\sin\psi & \sin\psi\sin\theta\cos\phi - \sin\phi\cos\psi & \cos\theta\cos\phi \end{bmatrix} \tag{3.26}$$

To calculate kinematics quantities of every body, and, in this case, of the two sphere, it's useful to start with Newton's Second Law $\sum \vec{F} = m\vec{a}$. The forces acting on the body, as seen before, are the contact and the friction force calculated in the equation number (3.6) and (3.11), the second one also generate a moment because it's not direct towards the center of mass. For a reason that will become clear later, the forces inputted into the kinematics block are considered in the body-fixed frame of the ball and the socket. Since the forces are expressed in a body-fixed frame, the formulation of the Newton's Second Law is:

$$\vec{F} = m(\dot{\vec{v}} + \vec{\omega} \times \vec{v}) \tag{3.27}$$

from this can be easily calculated the acceleration in the body frame. Subsequently, by employing a rotational matrix, which it's discussed in detail in equation number

(3.26), both the velocity and position, following integration, can be obtained in the Earth-fixed frame. It is also important to determine kinematic quantities such as angular velocity and angular orientation of the body. Angular velocity is utilized in equation number (3.12) to calculate the sliding speed, while angular orientation will prove valuable in the upcoming chapter. In 3D bodies, the three angular velocities projected onto the three planes are interdependent, necessitating the application of the Euler equation provided below[14]:

$$\dot{\vec{H}}_c = \vec{M}_c \tag{3.28}$$

$H_c$ is the angular momentum, $M_c$ is the torque vector or moment, the subscript $c$ indicates that the quantities are calculate respect to the center of mass of the body, that in this case is generated by the friction force calculated in the equation number (3.11). The friction force is not direct towards the center of mass of the sphere so generates a momentum calculated as $\vec{M}_c = \vec{F_{fric}} \times \vec{r}$; $\vec{r}$ is the radius of the sphere, so there are two different momentum for the two sphere due to the different radius. The Euler equation usually is written respect to the body frame so, due to the transport theorem became:

$$^B\frac{d}{dt}(\vec{H}_c) + {}^B\vec{\omega} \times {}^B\vec{H}_c = {}^B\vec{M}_c \tag{3.29}$$

here the apex $B$ means that all the quantities are referred to the body-fixed frame, the angular momentum is equal to:

$${}^B\vec{H}_c = {}^B[I_c]\,{}^B\vec{\omega} \tag{3.30}$$

Where $I$ is the inertia matrix. In the end the Euler equation, considering the inertia as a constant, became as follow:

$${}^B[I_c]\,{}^B\dot{\vec{\omega}} + {}^B\vec{\omega} \times {}^B\vec{H}_c = {}^B\vec{M}_c \tag{3.31}$$

In this thesis the moment of inertia of the body are calculated along the principal axis in order to have an inertia matrix with only the diagonal input, like this:

$$[I] = \begin{bmatrix} I_{11} & 0 & 0 \\ 0 & I_{22} & 0 \\ 0 & 0 & I_{33} \end{bmatrix} \tag{3.32}$$

Having an inertia matrix with only the diagonal input allows to re-write the equation number 3.31 to have three equation and no more a matrix equation.

$$\sum M_x = I_x\dot{\omega_x} - (I_y - I_z)\omega_y\omega_z \tag{3.33}$$

$$\sum M_y = I_y\dot{\omega}_y - (I_z - I_x)\omega_z\omega_x \tag{3.34}$$

$$\sum M_z = I_z\dot{\omega}_z - (I_x - I_y)\omega_x\omega_y \tag{3.35}$$

From the previous equations can be easily found the angular acceleration and, by integrating one times, the angular velocity; it should be noted that these quantities are expressed in the body-frame. So it's necessary to refer the angular velocity to the Earth-frame and to do this a rotational matrix should be used, but the rotational matrix change with time due to the angular velocity. So the rotational kinematic equation has to be used, below there is the matrix form of the equation:

$$\begin{bmatrix}\dot{\psi(t)}\\ \dot{\theta(t)}\\ \dot{\phi(t)}\end{bmatrix} = \underbrace{\begin{bmatrix}* & * & *\\ * & * & *\\ * & * & *\end{bmatrix}}_{B(\psi,\theta,\phi)} \begin{bmatrix}\omega_1(t)\\ \omega_2(t)\\ \omega_3(t)\end{bmatrix} \tag{3.36}$$

where the B matrix has to be calculated for a 3-2-1 rotation of the body-frame respect to the Earth-frame. A rotation 3-2-1 is used and this means having a rotation around the third axes, then around the second axes and lastly around the first axes, as in the steps done before to calculate the rotation matrix of the equation 3.26. The starting situation is the same reported in the figure number 3.13 and The first rotation is around the third axes of angle $\psi$ with an angular velocity $\vec{\omega_{B'/N}} = \dot{\psi}\hat{b'_3}$, this rotation is shown in the figure number 3.14 and its rotation matrix is calculated in the equation 3.20. The second rotation is around the second axes of angle $\theta$ with an angular velocity $\vec{\omega_{B''/B'}} = \dot{\theta}\hat{b''_2}$, this rotation is shown in the figure number 3.15 and its rotation matrix is in the equation 3.21. Finally, the third rotation is around the first axes of angle $\phi$ with an angular velocity $\vec{\omega_{B'''/B''}} = \dot{\phi}\hat{b_1}$, this rotation is shown in the figure number 3.16 and its rotation matrix is in the equation number 3.22. The angular velocity is therefore equal to:

$$\vec{\omega_{B/N}} = \vec{\omega_{B/B''}} + \vec{\omega_{B''/B'}} + \vec{\omega_{B'/N}} = \dot{\psi}\hat{b_1} + \dot{\theta}\hat{b''_2} + \dot{\psi}\hat{b'_3} \tag{3.37}$$

expressing all the calculus to the body frame before the rotation, the angular velocity became:

$$\vec{\omega_{B/N}} = (-\sin\dot{\psi}+\dot{\phi})\hat{b_1}+(\sin\phi\cos\theta\dot{\psi}+\cos phi\dot{\theta})\hat{b_2}+(\cos\phi\cos\theta\dot{\psi}-\sin\phi\dot{\theta})\hat{b_3} \tag{3.38}$$

which in matrix shape is:

$$\begin{bmatrix}\omega_1\\ \omega_2\\ \omega_3\end{bmatrix} = \begin{bmatrix}-\sin\theta & 0 & 1\\ \sin\phi\cos\theta & \cos\phi & 0\\ \cos\phi\cos\theta & -\sin\phi & 0\end{bmatrix} \begin{bmatrix}\dot{\psi}\\ \dot{\theta}\\ \dot{\phi}\end{bmatrix} \tag{3.39}$$

making the inverse of the matrix just written finally it's possible to found the matrix cited in the equation number (3.36).

$$\begin{bmatrix} \dot{\psi} \\ \dot{\theta} \\ \dot{\phi} \end{bmatrix} = \begin{bmatrix} 0 & \frac{\sin\phi}{\cos\theta} & \frac{\cos\phi}{\cos\theta} \\ 0 & \cos\phi & -\sin phi \\ 1 & \sin\phi\tan\theta & \cos\phi\tan\theta \end{bmatrix} \begin{bmatrix} \omega_1 \\ \omega_2 \\ \omega_3 \end{bmatrix} \tag{3.40}$$

Having the matrix now it's possible to found the Euler angle, by one integration, which are used in the following chapter.

### 3.2.1 Simulink kinematic model

In this subsection the model made on Simulink is shown in order to see how the kinematic equations of the previous section are integrated in the software; the complete kinematic model is shown in the figure 3.17, the figure refer to the inner sphere. In the figure 3.17 each colored box represents an equation which has been

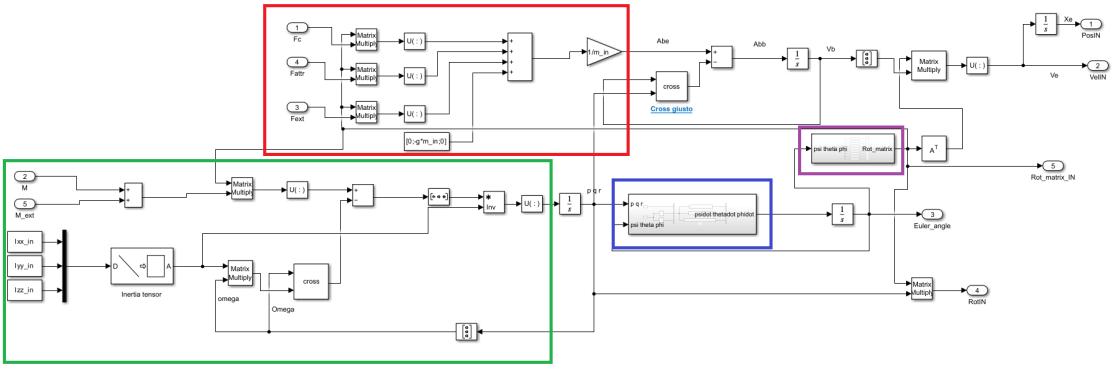


**Figure 3.17:** Simulink kinematic model

discussed in the previous section. The red box is the implementation on Simulink of the Newton's Second Law where the forces are the contact and the friction forces generated during the contact and a "external" force which is related to the controlled surface for the inner sphere and to the actuator for the outer sphere. The forces are expressed in the inertial frame so in order to be elaborated in the kinematic block they have to be converted in the body frame as it can be seen by the multiplication with the rotation matrix. The green box represents the Simulink implementation of the Euler's equation number 3.31. From this it's possible to see that the inertial matrix is diagonal but the calculus are made considering the matrix form of the Euler's equation due to the minor computational cost. In this green box there is a moment called "external moment" which is the moment generated by the frictional force as it is not applied in the direction of the center of mass. The

purple box is the implementation of the rotation matrix written in the equation number 3.26 and the subsystem can be seen in the figure number 3.18. Lastly, the

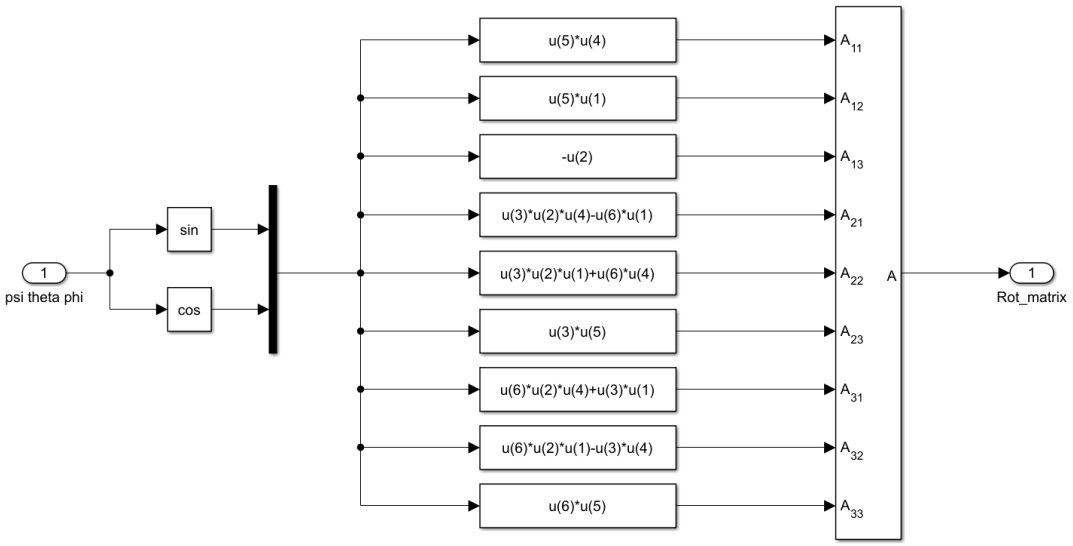


**Figure 3.18:** Simulink implementation of the rotation matrix

blue box is the representation of the kinematic differential equation done from the equation number 3.36, a more detailed image is in the figure number 3.19. All the

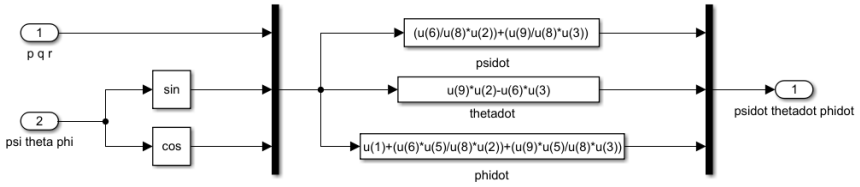


**Figure 3.19:** Kinematic differential equation

other Simulink block that are not highlighted with a colored box are block useful for the functioning but that are not seen in any equation of the previous section.

## 3.3 Model validation

Now that all the quantities required to the contact are found it's necessary to understand if the model created does work or not. To do this, simple operating situations are created, this procedure is called "validation". The first thing which has been validated is the kinematic block. His validation it has be done using

a block already present in Matalab which is called *"6DOF"*. This block has the same purpose of the kinematic block creating for this thesis. To comprehend how the model's operation works properly the results obtained with the kinematic block have been compared to the ones obtained by the 6DOF block. For the same input forces in the two block we are looking for the same results and this is what happened for the model creating in this work. The first test conducted to verify the

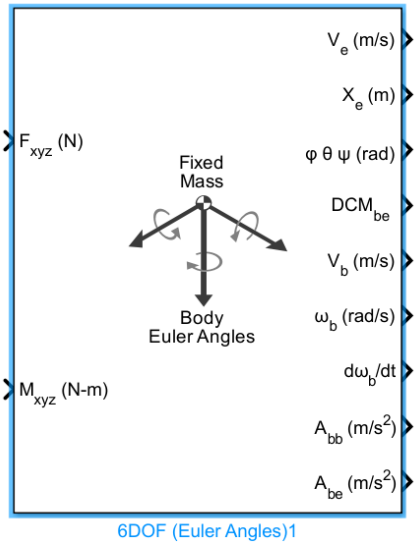


**Figure 3.20:** 6DOF block

correct functioning of the model is carried out using constant force and moment inputs. From the kinematics model shown in figure number 3.17, the initial part where all the forces acting on the two spheres are summed is removed. The same is done for the sum between the friction-generated moment and the moment due to the rotational part of the three-dimensional spring (which is explain in the following chapter), so that the force and moment input are relative to the sum of forces and moments acting on the body. Therefore, as mentioned, the first test is performed with constant inputs, specifically using the vector [3,6,9] as input for both force and moment. The obtained results are shown in Figure number 3.21. This figure shows the difference between the results of the 6DOF block and those of the model created for this thesis. The quantities examined are linear position and linear velocity, angular velocity and, finally, the Euler angles. Regarding the Euler angles, a clarification is necessary: instead of showing the difference in value for all three angles, it is decided to create a "magnitude" so that the difference between the two blocks is grouped under a single value to make the graph reading clearer and more intuitive. The absolute value of the 3 Euler angles is not important in this analysis, so applying the "magnitude" does not compromise the quality of

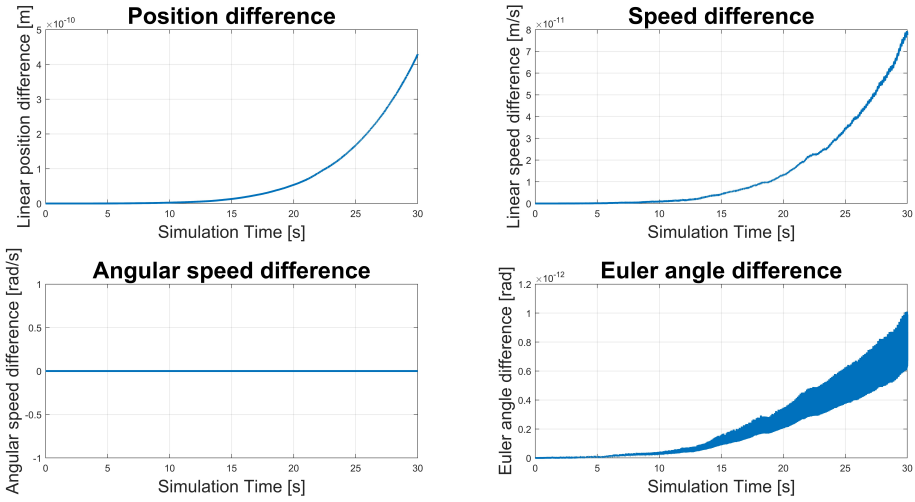


**Figure 3.21:** Model validation with a constant input

the analysis. Analyzing the results shown in the figure immediately reveals that the difference between the two models is very small and therefore negligible; the peak of precision is reached for the angular velocity, which is identical for both models. The difference between the quantities is of an order of magnitude much smaller than the absolute value of the results expected, which is why it is considered negligible. With a constant force and moment input, the "error" between the two models tends to increase over time during the simulation, but this is what we expect because there is an error present at each iteration that adds to the errors calculated in the previous iterations. Furthermore, the analysis was carried out over a simulation time of 30 seconds, which is much longer than the one used to obtain the results of the complete model. A second test was carried out with a sinusoidal input, the results of which are shown in Figure number 3.22. From the figure, it can be seen that here too the error has an entirely acceptable order of magnitude; it can be noted that the error of the various quantities considered is not monotonically increasing, which may be due to the fact that the sinusoidal input has both negative and positive forces and the same goes for moments, so it is likely that the negative part of forces and moments balances the error created by the positive part. A third test was conducted with a ramp input for both forces and moments, and the results are shown in Figure number 3.23. As can be seen, the results are also good for this type of input and take on a much more similar trend to the constant input, as was easily imaginable.

After seeing that the kinematic part is working properly then the contact should be tested in fact there may be some errors, for example it's possible to have that the two bodies interprenetrate each other as if they are not "solid". Another thing

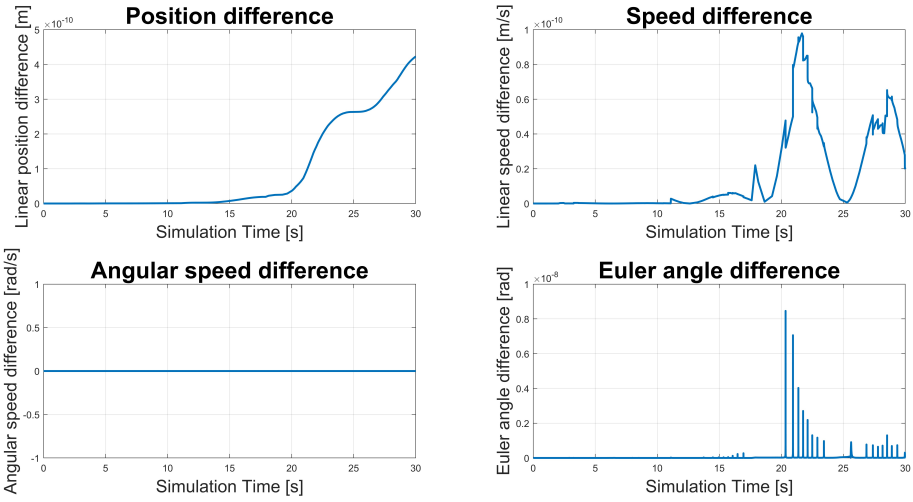


**Figure 3.22:** Model validation with a sinusoidal input

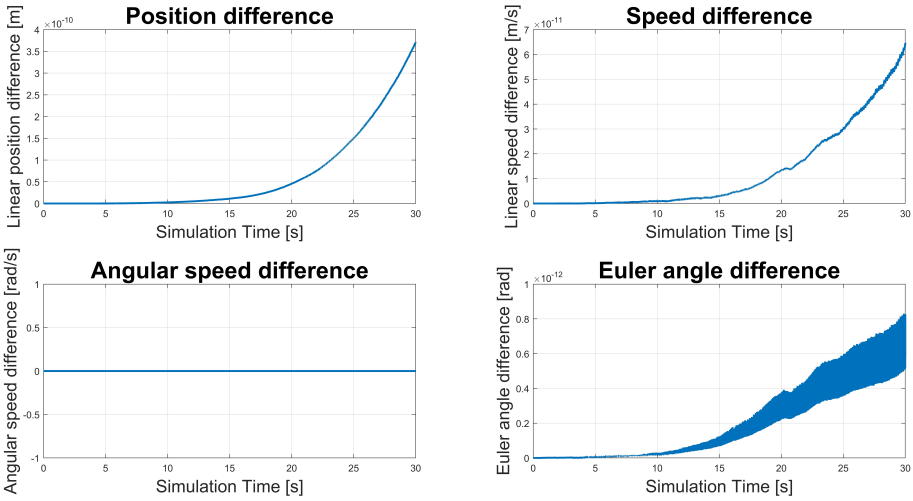


**Figure 3.23:** Model validation with a ramp input

that may happened is that the two bodies does not interprenetarte but after the contact the inside sphere start to move in an uncontrolled manner. So the first test consists of constrain the socket, so he can't move, and do not apply any forces to the ball in order to have only the gravity. The ball should move in the direction of the gravity until it touch the socket and it has to stop there without friction force and with a constant contact force, it's possible that little bounces can happen due to the damping of the contact force. The results of this test are shown in the

figure number 3.24. From the figure can be seen that the Position of the inner

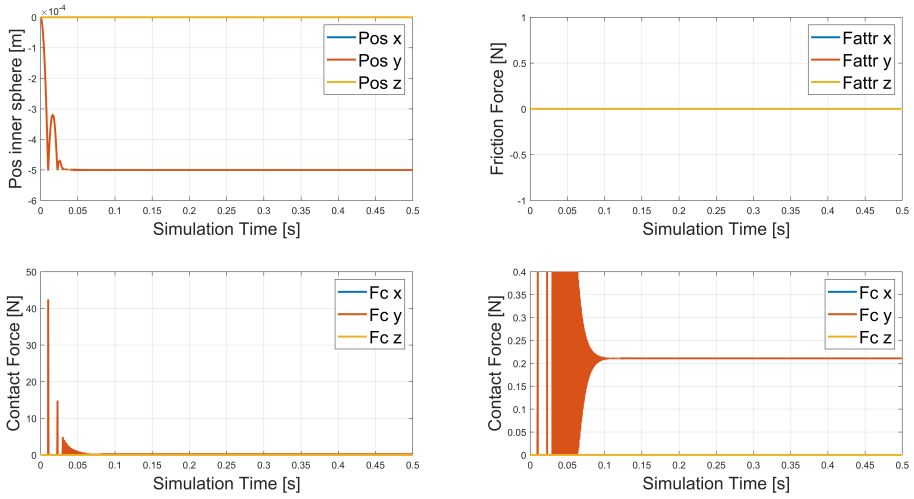


**Figure 3.24:** Result of the gravity test

sphere changes only along the y-direction, which it's the gravity direction, with some "bounces" that are caused by the stiffness and by the damping of the contact model. The final value of the inner sphere position is 0.0005 m which is the value of the joint clearance; this means also that the two sphere does not interprenetrate each other and that they are "solid". From the figure can be also seen that the friction force is null, as expected, and that the contact force, when the maximum eccentricity is reached, is equal to only the gravity force which is 0.2 N for a mass equal to 0.2 kg of the inner sphere. This is the most simple test that should be done on the model to verify the contact, but it's also important to do more complicated test in order to understand if any other problem can happened.

As a more complex test we realize the situation shown in the figure 3.25 (the difference in diameter between the two spheres has been exaggerated for the sake of clarity in the illustration), here the socket is constrained with a three-dimensional spring to the ground in order to have the socket that tends to stay in the initial position. Instead the ball is connect to a three-dimensional spring where the motion is applied in one hand. The working principle is the following one:

- A force, which generates a motion, is applied to one hand of the spring connect to ball,
- The spring transmits motion to the center of the sphere which, in turn, sets itself in motion,
- The ball is free to move until it comes into contact with the socket,

- At this point the contact force between the the ball and the socket try to set the constrained socket in motion

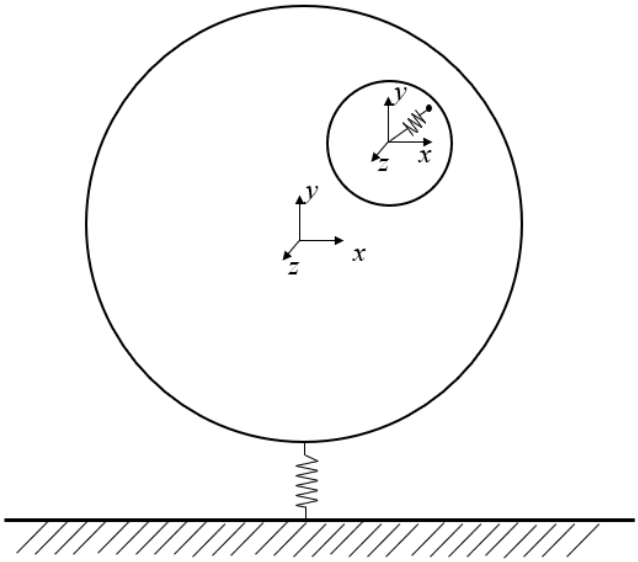


**Figure 3.25:** Test contact model

The results of this test can be seen in the figure number 3.26, the input position applied to the free hand of the inner sphere spring is a ramp input. When the ramp input is applied, the inner sphere start immediately to move and the eccentricity begin to increase its value, in the zoom box of the first subplot it's shown how the spring work. When the eccentricity has not reach the value of the joint clearance the spring force of the inner sphere goes up and down, in fact the sphere is not constraint and does not oppose resistance. Then the maximum value of eccentricity is reached and the outer sphere start to move trying to follow the inner sphere, the outer sphere spring try to force the outer sphere to stay in the original position with a negative force.

These two are therefore the two "tests" used to validate the contact model in this thesis, both has given positive results so the contact model can be considered validated as also the kinematic model which has been tested with the *6DOF* block.

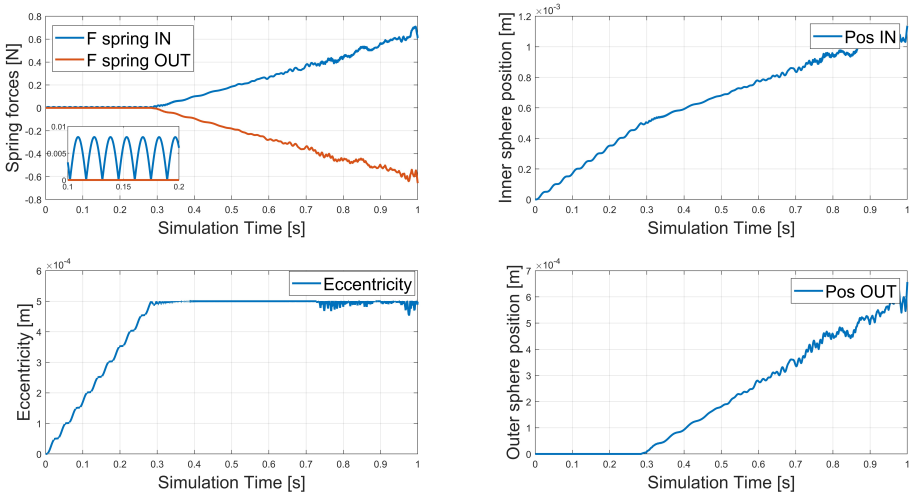


**Figure 3.26:** Contact test results with springs

# Chapter 4

# Rod-end implementation

In order to simulate the correct working condition of the rod-end there must be something that sets one of the two spheres in motion, to do this a kinematics is used. The kinematics lead in motion one of the two sphere, then there will be the contact force between the two sphere that lead in motion the other sphere. The choice of the kinematics is done in order to have a simple mechanism which is easy to analyzed but is also realistic; every airplane has its own mechanism for the control surface so in this thesis no reference has been made. The only parameter sought to be respected is the transmission ratio $\Delta L/\Delta\theta$ in order to take from a previous thesis the Simulink model of the dynamics of the actuator and not doing it from zero. The chosen mechanism is a simple slider-crank mechanism as it shown in figure number 4.1. The crank is connect to the control surface while the the slider is an actuator, based on the linear position of the actuator the crank generate an angle $\theta$ which is also the angle of rotation of the control flight surface. To comply with the constraint imposed by the transmission ratio, the links of the mechanism are of the following lengths:

- $s = 0.11$ m which is the length of crank;
- $t = 0.38$ m which is the length of the frame;
- $l = 0.37$ m which is the length on the slider with the actuator in the zero position, the actuator stroke is 0.06 m So as to have a control surface angle equal to $\pm 35°$.

The mechanism, as it's defined before, is shown in the figure number 4.2. Looking the scheme of the mechanism, corresponding to the point P it's positioned the rod-end, on the link $\overline{OP}$ of the scheme there is the actuator which it's not represented for a better comprehension. The horizontal line at the right of the point Q is a schematic representation of the control surface. So, based on the extension of the

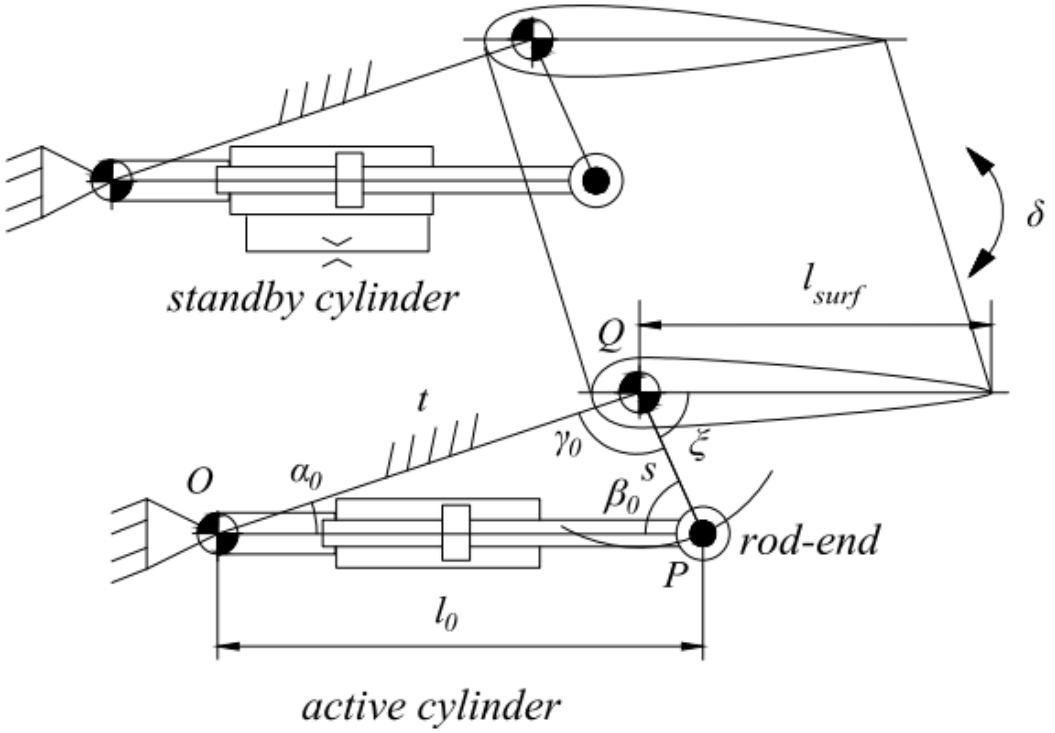


**Figure 4.1:** Kinematics

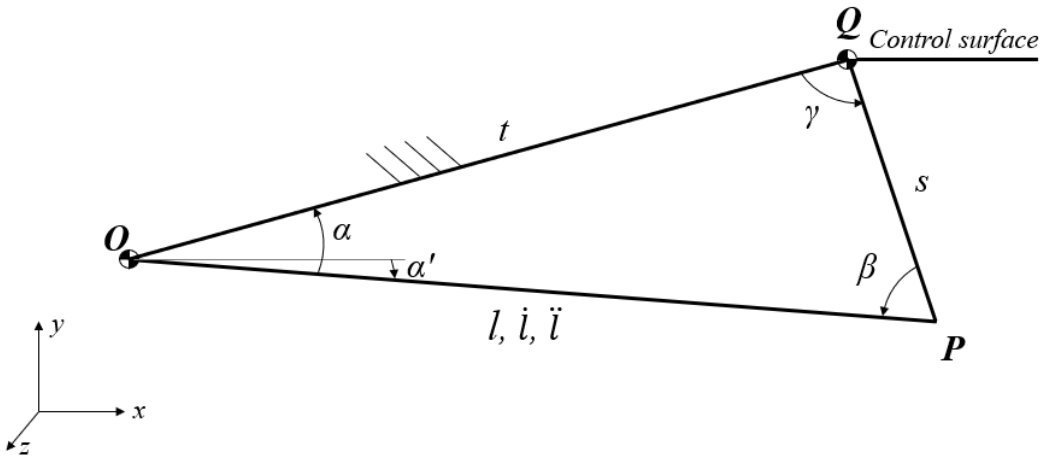


**Figure 4.2:** Scheme of the mechanism

actuator, positioned on the slider, the angle of the mechanism and the control flight surface changes. Knowing the length of all three link of the mechanism it's possible to find all the angle using the law of cosine as follows:

$$l^2 = t^2 + s^2 - 2st\cos\gamma$$
$$\rightarrow \gamma = \arccos\left(\frac{t^2 + s^2 - l^2}{2st}\right) \tag{4.1}$$

$$s^2 = t^2 + l^2 - 2lt\cos\alpha$$
$$\rightarrow \alpha = \arccos\left(\frac{l^2 + t^2 - s^2}{2lt}\right) \tag{4.2}$$

$$t^2 = l^2 + s^2 - 2ls\cos\beta$$
$$\rightarrow \beta = \arccos\left(\frac{l^2 + s^2 - t^2}{2ls}\right) \tag{4.3}$$

In order to model the mechanism in a more realistic way, between the links, the slider and the crank, of the mechanism and the rod-end a three-dimension spring is inserted, so between the slider and the outer sphere of the rod-end and between the crank and the inner sphere of the rod-end there is a spring. The three dimensional spring has both a stiffness factor and a damping factor so in a more detailed manner it can be represent by a spring and a damping. The spring it's called "three dimension" because it has a linear component and a rotational component. The linear component is insert in order to have not a rigid connection between the rod-end and the link of the mechanism while the rotational component is useful to constrain the rotation, around the three axis, of both the sphere of the joint which without it are free to rotate around their center of mass. A schematic draw of the connecting spring can be seen in the figure number 4.3. When the

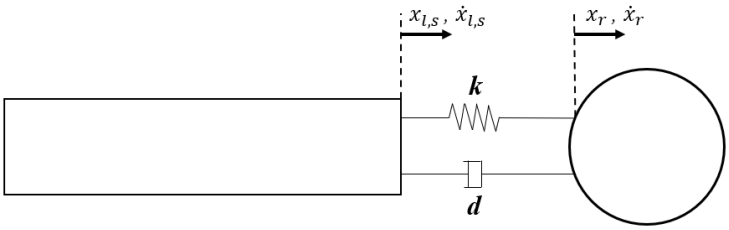


**Figure 4.3:** Schematic representation of the three dimensional spring

spring contracts or extends, it transmits a force to the rod-end spheres. In this case, to provide a clearer example, between the outer sphere and the crank, the

transmitted force is equal to the stiffness multiplied by the difference in position between the inner sphere and the end of the crank. To this force is added the damping multiplied by the difference between the linear velocity of the center of gravity of the inner sphere and the end of the crank. So the linear force formula between the inner sphere and the end of the crank is:

$$F_{spring} = k(x_r - x_s) + d(\dot{x_r} - \dot{x_s}) \tag{4.4}$$

where $k$ is the stiffness, $d$ is the damping factor, $x_r$ and $\dot{x_r}$ are respectively the position and the velocity of the sphere, $x_s$ and $\dot{x_s}$ are the position and the velocity at the end of the crank. For the spring which connects the slider with the outer sphere of the rod-end there is a different situation. In fact, as can be seen from figure number 4.2, the mechanism used to simulate the behavior of the rod-end is a two-dimensional mechanism. This would imply that the joint, even though modeled in three dimensions, functions like a joint modeled in two dimensions. Therefore, to achieve a "three-dimensional" operation, a decision was made to impose an initial position of the outer sphere that is offset from the z-axis, which is the axis coming out of the drawing. In this way, it is expected that the joint will function by simulating a three-dimensional behavior rather than a two-dimensional one. The outer sphere is positioned as if there is a small assembly error, so its initial position is as follows $[0; 0; 0.0001]$ for example (respectively along x, y, and z axes), where 0 indicates a perfect concentric assembly of the two spheres. The assembly error has been deliberately assumed to be very small and is a hypothetical value. So the spring force became:

$$F_{spring} = k(x_r - x_l - x_i) + d(\dot{x}_r - \dot{x}_l) \tag{4.5}$$

where $x_i$ is the initial position of the sphere and $x_l$ and $\dot{x}_l$ are the position and the speed of the end of the slider. Below is the Simulink diagram used to find the linear force of both springs. More specifically, in Figure 4.4, there is the diagram for the spring connecting the actuator to the outer sphere, while in Figure 4.5, there is the diagram of the spring present on the flight control surface and inner sphere. The calculation of the force exerted by the spring on the actuator and the outer sphere, performed using Simulink, has been configured such that compression of the spring generates a positive force, as highlighted in the diagram. For instance, when the actuator extends and its position increases towards positive values while keeping the sphere's position constant, a positive spring force is obtained. This choice is motivated by the fact that the force exerted by the spring on the sphere acts as an external force inducing motion. Therefore, with a positive spring force, the sphere moves towards higher coordinates, whereas with a negative spring force, it moves towards lower coordinates. Conversely, examining the Simulink diagram of the spring between the surface and the inner sphere, it is observed that compression of

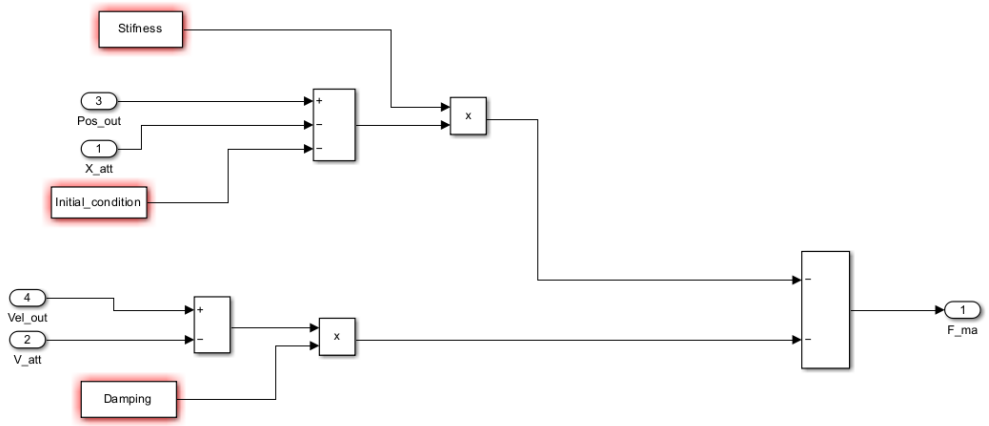


**Figure 4.4:** Simulink scheme of the actuator-outer sphere spring

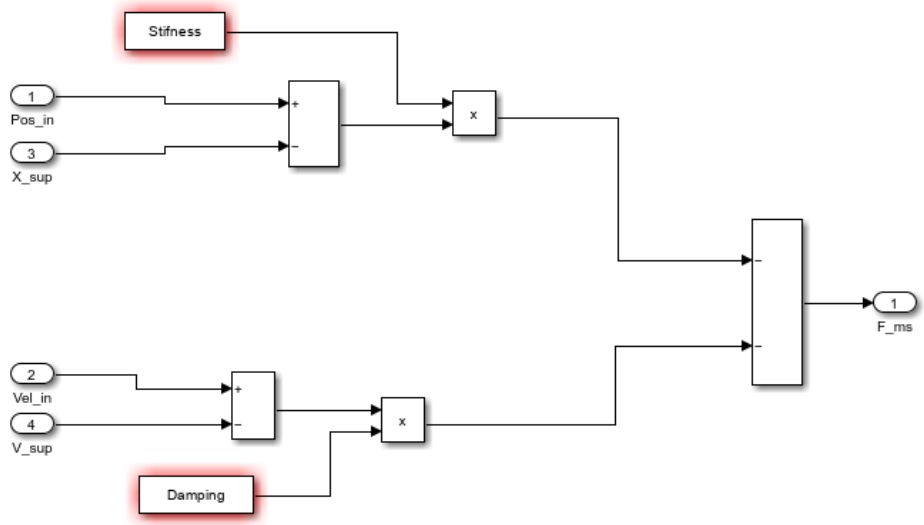


**Figure 4.5:** Simulink scheme of the inner sphere-control surface spring

the spring generates a negative force, whereas the force is positive when the spring is stretched. When the spring is compressed, the sphere tends to move towards lower coordinates, hence a negative force has been chosen. Regarding the rotational

component of the spring, as mentioned earlier, its role is to prevent rotation around the center of gravity of the rod-end spheres. Exiting the kinematics subsystem of both spheres, as described in the previous chapter, Euler angles are obtained. Euler angles correspond to three successive rotations, while for the calculation of the spring force, the rotation angles, with respect to the three axes describing how much the sphere has rotated, are required. However, it is possible, by knowing the Euler angles, to describe the rotation as a "pure" rotation around an axis unit vector $\hat{e}$ of an angle $\Phi$. In the figure number 4.6 can be seen the rotation from the inertial frame to the body frame, realized with the three successive rotation by the three Euler angle, that can be described by a "pure" rotation. From the cosine

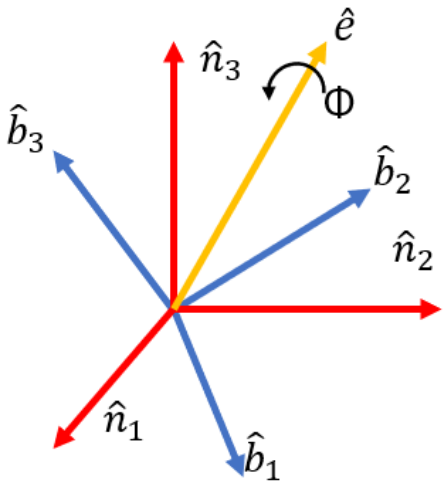


**Figure 4.6:** Arbitrary rotation written as a pure rotation

direction matrix, which has the information of the three Euler angle, is possible to calculate the angle of rotation $\Phi$ and the unit vector $\hat{e}$ as follows:

$$\Phi = \arccos\left(\frac{1}{2}(C_{11} + C_{22} + C_{33} - 1)\right) \tag{4.6}$$

$$\hat{e} = \frac{1}{2\sin\Phi}\begin{pmatrix} C_{23} - C_{32} \\ C_{31} - C_{13} \\ C_{12} - C_{21} \end{pmatrix} \tag{4.7}$$

Now having the angle of rotation around the unit vector $\hat{e}$ it's possible to projecting the angle to the axis x,y,z to find the rotation of the sphere around the x,y and z axes. Actually, contrary to what was stated earlier, the two spheres of the rod-end

must have the ability to rotate around their own center of gravity. By looking at Figure 4.7, the reason becomes immediately clear. Looking at the figure, it becomes

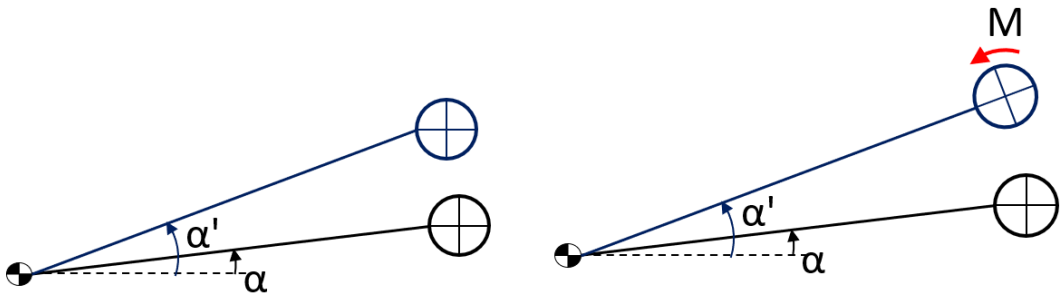


**Figure 4.7:** Scheme used to describe the function of the rotational part of the spring

clear that the two spheres must be able to rotate in order to remain attached to the actuator and the flight control surface when their inclination changes. In fact, if the sphere were to remain fixed without rotating, and we consider the viewpoint above the actuator, we would observe that as the inclination changes, the sphere actually undergoes clockwise or counterclockwise rotation. The goal is to have no rotation of the sphere from this reference frame attached to the actuator. Therefore, it is necessary to apply a clockwise or counterclockwise moment depending on whether the inclination of the actuator is decreasing or increasing. The same applies to the inner sphere and the flight control surface. In Figure 4.8, you can see the implementation in Simulink of what has been described for the outer sphere. Once the rotation of the sphere due to the applied forces is calculated, using equations (4.6) and (4.7), the change in the actuator's inclination angle needs to be subtracted from the z-coordinate value. The actuator's rotation angle is subtracted because, as seen earlier, the sphere must also rotate as the actuator's inclination changes. If the sphere, around the z-axis, is rotating counterclockwise and due to the increase in the actuator's inclination, a counterclockwise moment is required, then the counterclockwise rotation possessed by the sphere will already cause the sphere to rotate to compensate for the increase in the actuator's inclination. Therefore, the change in the actuator's inclination angle is subtracted. The spring also has a damping component without which it would exhibit unstable behavior. For implementing the damping part in Simulink, it is necessary to subtract from the sphere's rotation velocity the rate at which the actuator's inclination angle changes, for the same reasons discussed earlier for the rigid part of the spring. The implementation in Simulink of the spring connecting the flight control surface

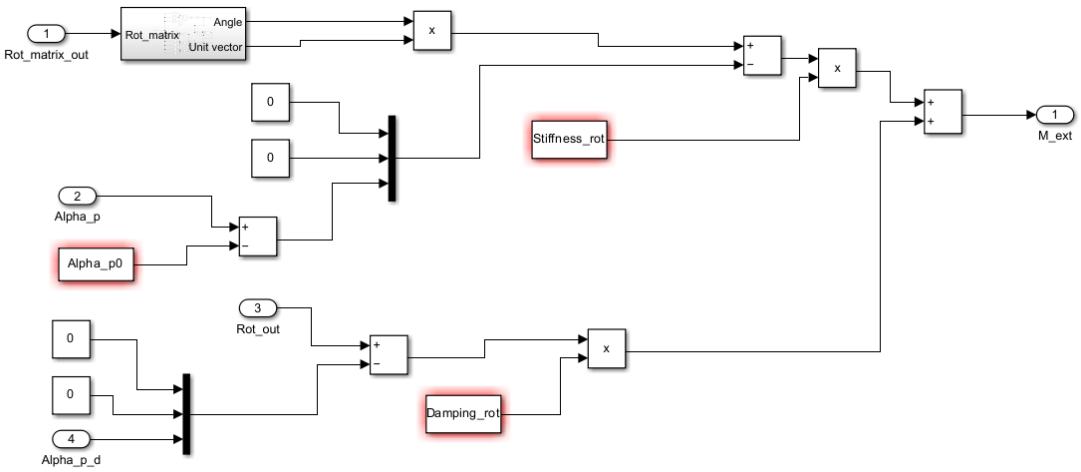


**Figure 4.8:** Simulink scheme of the outer sphere momentum

with the inner sphere can be seen in Figure 4.9. The diagram will not be further commented on since the reasoning is the same as that already discussed for the spring connecting the actuator with the outer sphere.

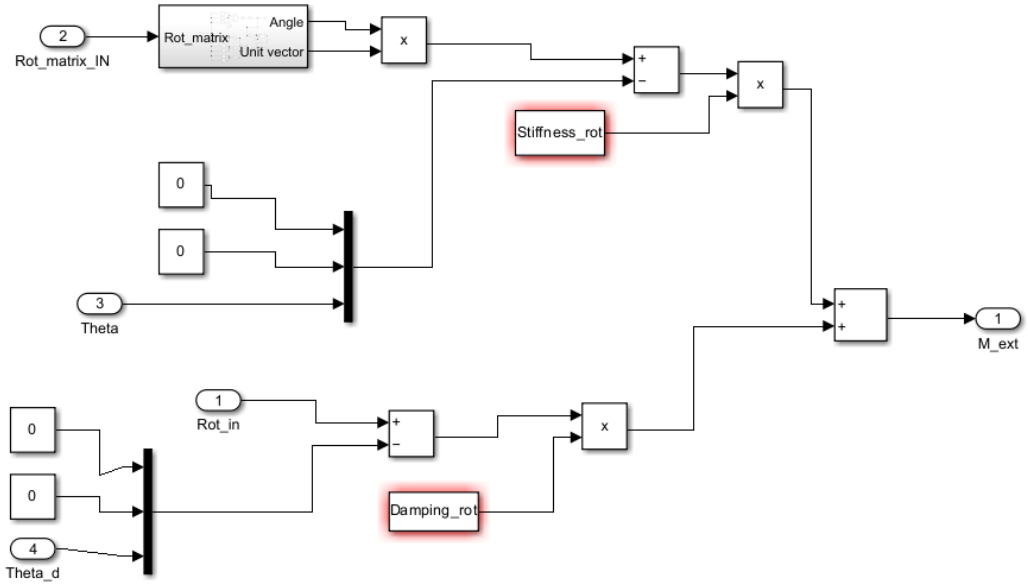


**Figure 4.9:** Simulink scheme of the inner sphere momentum

After describing the elements that form the mechanism in the figure number 4.2, let's now review the logical flow of information that allows simulating the behavior of the control surface actuation mechanism. First, we start from a resting position where, except for gravity, there are no other forces acting on the system. The first step is to impose an extension to the actuator located on the mechanism's slider. In the specific case of the model created in Simulink, a velocity for the actuator extension and retraction is imposed to then derive the position by integrating the velocity. Once the velocity and position of the actuator are set, the next step is to understand how the velocity and position at the end of the slider are influenced. Indeed, the extension or retraction of the actuator always follows the direction of the slider since it is positioned on it. However, the connecting rod has the ability to rotate around point O (figure 4.2), so the position and velocity of the end of the slider, where the spring is attached, do not correspond to the velocity and position imposed on the actuator. A scheme with for the calculus of the velocity is reported in the figure number 4.10 and 4.11. In the figure number 4.10 is represent the

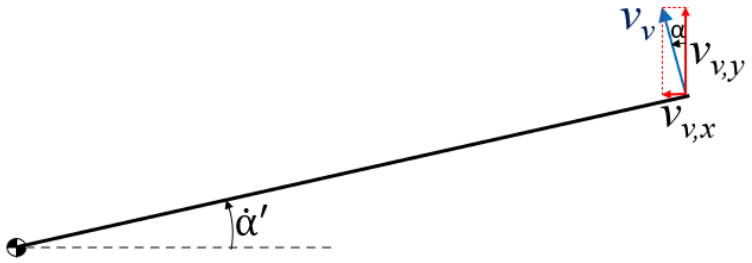


**Figure 4.10:** Scheme of the velocity due to the angular movement of the slider

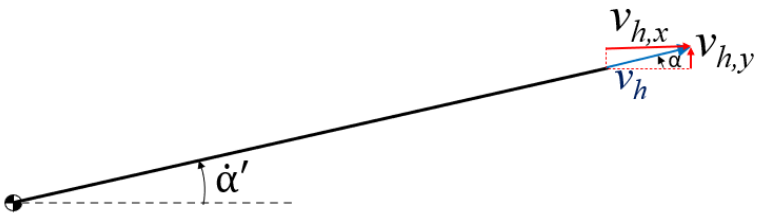


**Figure 4.11:** Scheme of the velocity due to the displacement of the actuator

velocity due to the angular velocity of the slider which generate a linear velocity $v$ at the end of the slider that is divided in the vertical and horizontal component respectively $v_y$ and $v_x$. In the figure number 4.11 is represent the velocity due to the actuator extension which is the same direction of the slider, also this velocity is divided into the vertical and horizontal component which are in the same direction

of the x and y axis. So the vertical velocity at the end of the slider is calculated as follows:

$$v_x = v_h \sin \alpha' + v_v \cos \alpha' \tag{4.8}$$

$$v_y = v_h \cos \alpha' + v_v \sin \alpha' \tag{4.9}$$

Regarding the position, instead, the position of the end of the slider relative to point O is calculated, subtracting the initial position of the end of the slider referenced to point O in initial conditions. This way, the initial position of the end of the slider in the Simulink model is considered as the zero position. As can be inferred, the position and velocity along the z-axis due to the actuator are zero, as the mechanism is two-dimensional. After finding the position and velocity of the slider, we move on to the three-dimensional spring that connects the slider to the outer sphere of the rod-end. Here, as described earlier, the difference in position and velocity generates a force that will set the sphere in motion. Once the outer sphere comes into contact with the inner sphere, there will be an exchange of forces that will set the inner sphere in motion. The inner sphere is connected with a three-dimensional spring to the crank. The crank, receiving a force from the three-dimensional spring, will rotate around point Q, causing the flight control surface, being solidly mounted, to rotate by the same amount as the crank. The force transmitted from the spring to the crank is a three-dimensional force, directed in space. Therefore, only the components projected onto the x-y plane are useful for the rotational movement of the crank, which is constrained to rotation only in the x-y plane. In the figure number 4.12 is illustrated the force of the spring projected onto the plane x-y acting on the crank. The force can be divided in two components, one parallel to the crank and one perpendicular to the crank, and only the component called as $F_1$ generates a rotation of the crank. In the Simulink model, the block where the force of the three-dimensional spring is calculated returns the force of the spring in the three directions of the plane. Therefore, starting from the forces along x and y, it is necessary to find the force component that generates the rotation of the crank, a scheme is reported in the figure 4.13. The blue vector is the force useful for the rotation of the crank while the green vector is the spring force along the x-axis, to pass from the green vector to the blue vector the angle between them has to be found. To find this angle, the blue and green vectors are translated to the point Q. In this position, it is easy to see that the angle between the two vectors is equal to 90° minus the $\epsilon$ angle. To find the epsilon angle, look at the triangle $Q\hat{R}P$, and you can see that the $\epsilon$ angle is equal to:

$$\epsilon = 90^\circ - \beta - \alpha' \tag{4.10}$$

so the angle between the two vector is:

$$\delta = \beta + \alpha' \tag{4.11}$$

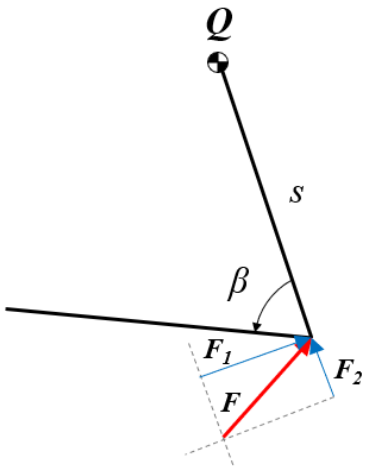


**Figure 4.12:** Force acting on the crank

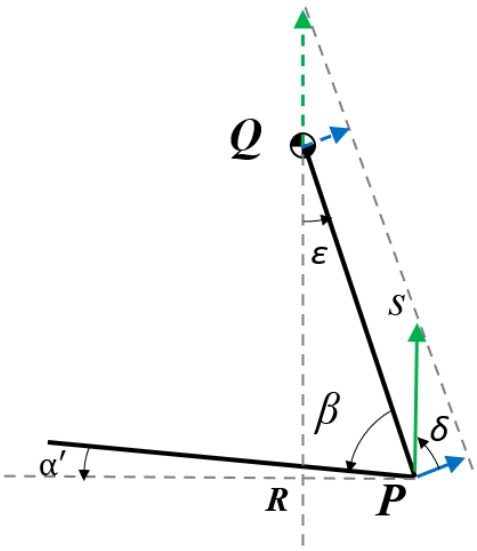


**Figure 4.13:** scheme of the force along y of the spring that generate a rotation of the crank

and the force component that allow the crank rotation is:

$$F_1 = F_y \sin(\beta + \alpha') \tag{4.12}$$

Now the same step should be done with the force along the y-axis as it can be seen in the figure number 4.14. From the figure can be easily found that the angle $\theta$

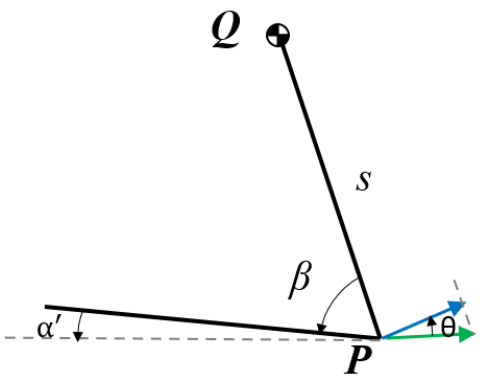


**Figure 4.14:** scheme of the force along x of the spring that generate a rotation of the crank

between the green and the blue vector is equal to:

$$\theta = \beta + \alpha' \tag{4.13}$$

and the force component that allow the crank rotation is:

$$F_1 = F_x \cos(\beta + \alpha') \tag{4.14}$$

Now that the spring force has been calculated, it is possible to achieve equilibrium for the rotation of the crank to find the angle theta by which it rotates. In the initial analysis, no external force acting on the flight surface is considered. Typically, an external force due to the air generating pressure and thus a force on the flight surface during flight should be indicated. Without the presence of the external force, the free-body diagram of the crank is represented in the figure 4.15. The

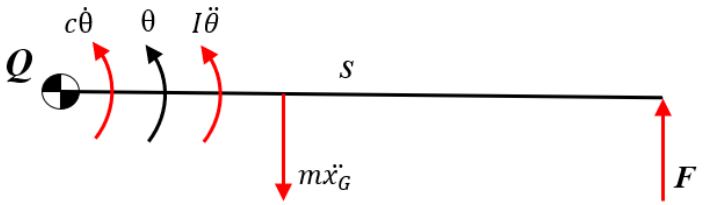


**Figure 4.15:** Equilibrium for the rotation of the crank

force $F$ is the force which it's calculated with the equation number 4.12 and 4.14,

the term $c\dot{\theta}$ is a rotational damping of the crank and the terms $I\ddot{\theta}$ and $m\ddot{x_G}$ are the inertia contributes. The inertia contribute $m\ddot{x_G}$ is positioned with a distance of $s/3$ from the point $Q$, this because the control surface is approximated with a triangular form as can be seen in the figure number 4.16, and the center of mass for that type of geometry is positioned there. So the force equilibrium of the crank

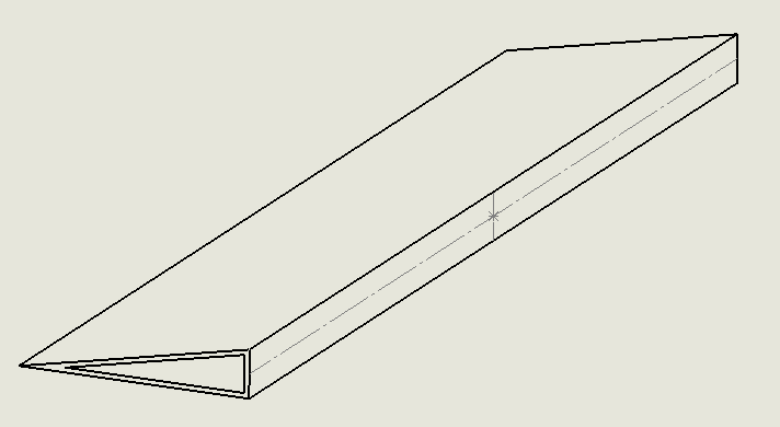

**Figure 4.16:** 3D draw of the flight control surface

around the point $Q$ is as follows:

$$Fs = mg\ddot{x_G}s/3 + I\ddot{\theta} + c\dot{\theta} \tag{4.15}$$

where $\ddot{x_g} = \ddot{\theta}s/3$ so the equation becomes:

$$Fs = mg\ddot{\theta}s^2/9 + I\ddot{\theta} + c\dot{\theta} \tag{4.16}$$

From this equation is possible to find the value of the angular acceleration of the crank and so also the value of the angular position of the crank. $\theta$ represent the angle of the deployment of the crank but referred to the initial position, it is not an absolute angular coordinate. Having the angular position of the crank allows to find the position of the end of the crank which is useful to compute the spring force of the three dimensional spring which connects the inner sphere to the crank; to do this some simple trigonometric calculus are needed. From the figure number 4.17 can be seen the scheme that allows to find the position and the velocity at the end of the crank. The Cartesian coordinates of the end point of the crank P' are found by considering the position when the mechanism is in the initial conditions as the zero position. To find the Cartesian coordinates necessary for the spring force calculation, the coordinates of point P are then subtracted from the coordinates of point P'. In this way, the result will be the $\Delta x$ and $\Delta y$ of the position between point P and point P'. The Cartesian coordinates for the point P are calculated

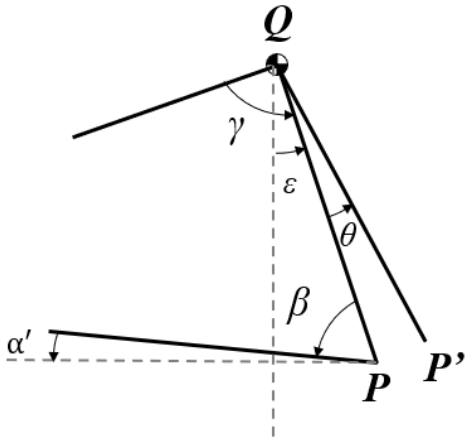


**Figure 4.17:** Scheme used to find the position of the end of the crank

respectively for x position e for the y position as follows:

$$P_x = s \sin \epsilon_0 \tag{4.17}$$

$$P_y = s \cos \epsilon_0 \tag{4.18}$$

where $\epsilon_0$ is calculated with initial condition. The Cartesian coordinates of the point P' are:

$$P_x = s \sin(\epsilon_0 + \theta) \tag{4.19}$$

$$P_y = s \cos(\epsilon_0 + \theta) \tag{4.20}$$

So the position of the end of the crank useful for the spring force is the difference between the x and y position of the two points. The last necessary thing is the velocity of the point P' of the crank which is calculated as follows:

$$v_P = \dot{\theta} s \tag{4.21}$$

Now we have all variables needed to run the model and verify the correct working, all this part it's written in the following chapter.

# Chapter 5

# Model Results

The first part of this chapter is composed of the analysis of the model results. Based on the results provided by the model, it is necessary to understand, through some examined quantities, whether the functioning can be considered correct. Within the model, it has been decided to use a parameter called "Initial condition", which defines the initial position of the inner sphere of the rod-end. The rod-end, as constructed in the model, has both spheres initially positioned with their center of mass at the initial position of [0;0;0]. The "Initial condition" parameter modifies the initial position of the inner sphere according to our needs; in our case, since the actuating mechanism is bidimensional with a connecting rod, without this parameter, the joint would always function as if it were a revolute joint, thus losing the three-dimensionality of the newly created model. Therefore, the "Initial condition" parameter will be used to simulate a misalignment along the z-axis, which can be like an assembly error, in order to observe the 3D behavior of the model; after all, the model has been created in three dimensions precisely to evaluate some of these possible scenarios. However, initially, in order to try to understand if the model works correctly, we put ourselves in the simplest condition to analyze, namely that with null "initial condition". After validating the results of the model with these "initial conditions", we will proceed to modify them and see how the quantities of interest change.

## 5.1 Model validation

To begin, the position and velocity inputs used to simulate the behavior of the actuator positioned on the connecting rod of the mechanism are shown. In the model, the actuator's velocity is set and then integrated to find the position. It is important to aim for a velocity function that is "smooth," meaning it does not have sudden changes in velocity that would lead to force spikes within the

contact of the rod-end spheres and make the behavior more unstable, which is not a situation that occurs in reality with the use of an actuator. Similarly, the position will be a function without discontinuities. The position and velocity inputs are shown in Figure 5.1, and as can be seen, they adhere to the considerations just described. Initially, it was decided to verify the system's operation with only the actuator extension phase. After examining the position and velocity inputs of the

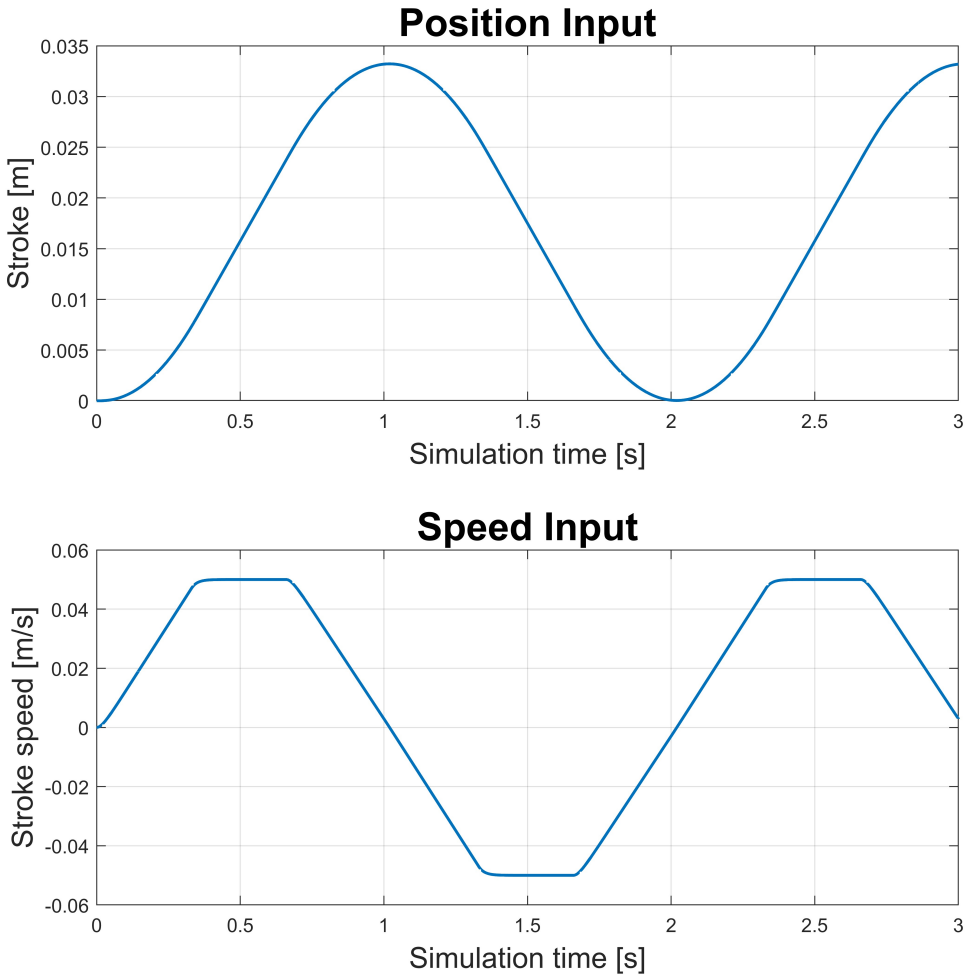


**Figure 5.1:** Position and speed input of the actuator

actuator, the first thing to check is the correct functioning of the contact within the rod-end. It is necessary to see if the contact conditions are correct and if the two bodies behave as "rigid" without intersecting each other. The proper functioning of the contact has already been discussed in the previous chapter; however, for

completeness, a graph showing its behavior is included in this chapter as well. Figure 5.2 illustrates the variation of eccentricity and the magnitude of the contact force exchanged between the spheres of the rod-end. The contact force should be

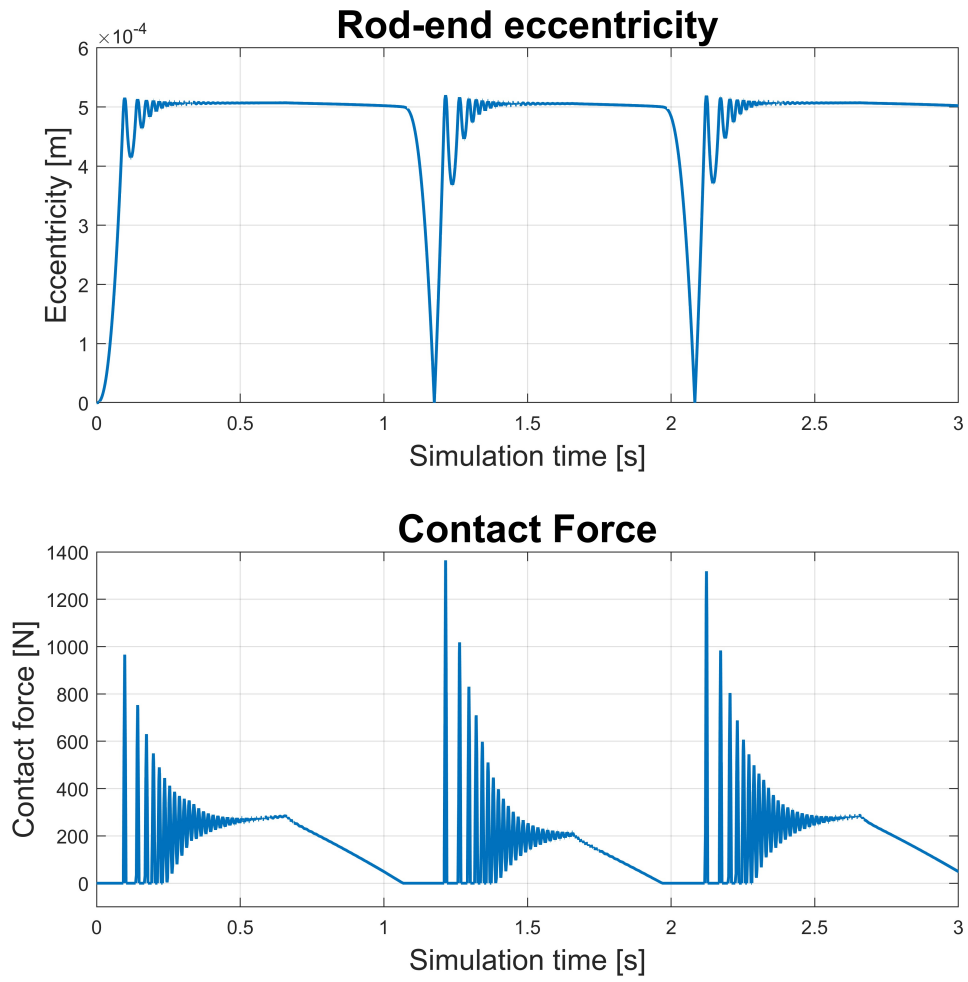


**Figure 5.2:** Eccentricity and contact force during the simulation

present only when the eccentricity between the two sphere centers exceeds the clearance value (equal to 0.0005 meters), and as shown in the figure, this is what happens. Also, from the figure, it can be easily observed that the contact is not constant but intermittent, which is due to the stiffness and damping parameters present in equation number (3.6) used in the contact modeling.

To understand if the model operates correctly, we trace the entire kinematic chain from the actuator extension to the extension of the flight control surface,

which corresponds to a counterclockwise rotation of the same. Starting from the actuator, represented simply by a position input in this case, its extension causes the movement of the outer sphere of the rod-end. The connection between the rod's end link and the outer sphere of the rod-end is schematized with a spring, as seen in the previous chapter. So, first, let's analyze the force trend of the spring, depicted in figure 5.3, where the trend of the position input used is also shown.

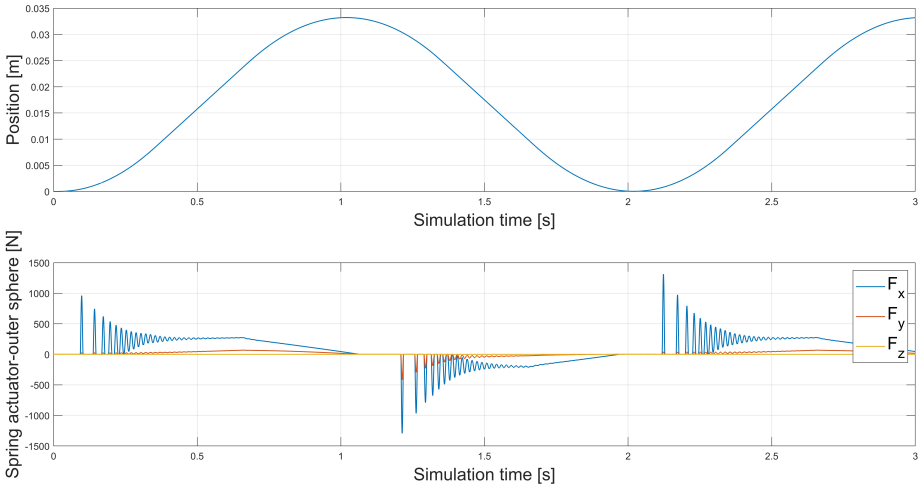


**Figure 5.3:** actuator-outer sphere spring force

As defined within the model, when there is compression, meaning the outer sphere and the end of the rod are brought closer together, the spring force is positive. Conversely, when the spring is extended, the force is negative. Looking at the figure, when the position input increases, it indicates that the actuator is considered to be extending, in this situation, the actuator will displace one end of the spring while the other end remains stationary, as the sphere is not yet in motion. The spring therefore tends to compress, resulting in a positive force that will then drive the movement of the outer sphere of the rod-end. Conversely, during the retraction phase of the actuator, the end of the spring connected to it will move in the opposite direction compared to the previous case. Thus, the spring tends to elongate, generating a negative force that causes the outer sphere to follow the actuator in its movement. As a consequence of initiating the motion of the outer sphere, regardless of whether the actuator is extending or retracting, contact between the two spheres will occur. Once the centers of the spheres surpass an eccentricity equal to the clearance value, contact is established. To understand the motion between the two spheres clearly, a polar plot graph is very useful, as shown in figure 5.4, which illustrates the difference between the positions of the inner and outer spheres. It displays the path on the xy-plane with a z-coordinate

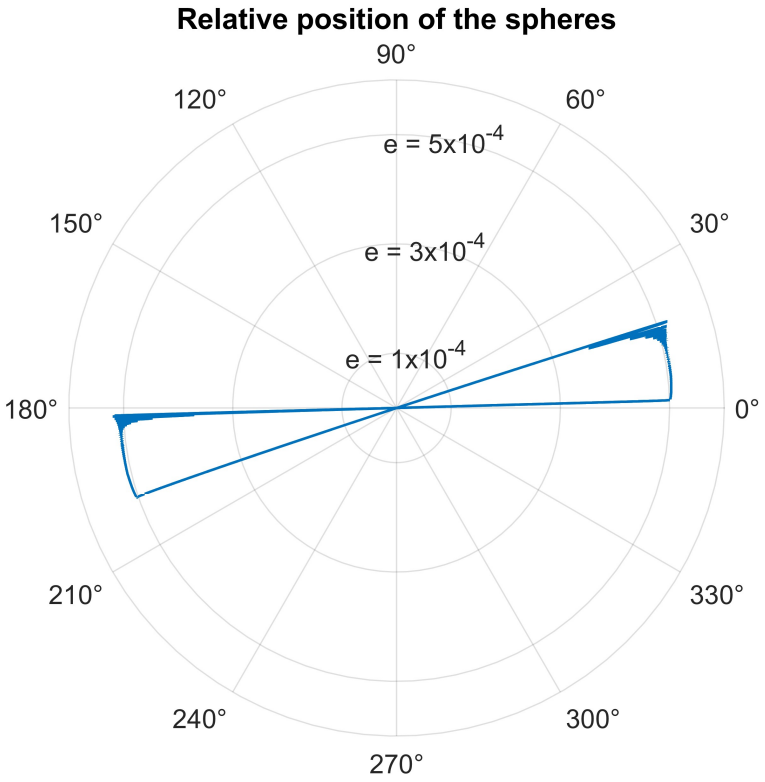


**Figure 5.4:** Polar plot of the relative position of the two spheres

of zero, as the motion of the two spheres occurs only in that plane. From the polar plot, can be immediately infer the relative motion of the two spheres composing the rod-end. The contact is represented by reaching a radial coordinate equal to 0.0005, which corresponds to the clearance value of the rod-end, as mentioned earlier. Additionally, from this plot, it can be observed that the contact between the two spheres always occurs within a certain angular portion of the circular crown of possible contact points. This is a crucial factor to control because the wear of the two spheres will be concentrated in that arc of the circle, leading to localized wear. As operating hours progress, this will result in a change in the trajectory that the rod-end can follow, and thus a less precise positioning of the control surface compared to the initial state. This graph is very illustrative because it also shows the trend of eccentricity, although less detailed than before, and here too, one can understand that the contact is not always continuous. To identify where the most wear is likely to occur, one can calculate a wear indicator as follows: $F_N \times V_{rel}$, where $F_N$ represents the normal force exchanged between the two spheres (i.e., the contact force), while $V_{rel}$ is the relative tangential velocity of

the two spheres (i.e., the speed at which the two spheres slide against each other). By approximately calculating wear as shown earlier and plotting the results on a polar plot, one can visually understand where the wear will be concentrated. The results are shown in Figure 5.5. In the graph, the polar variation of the contact

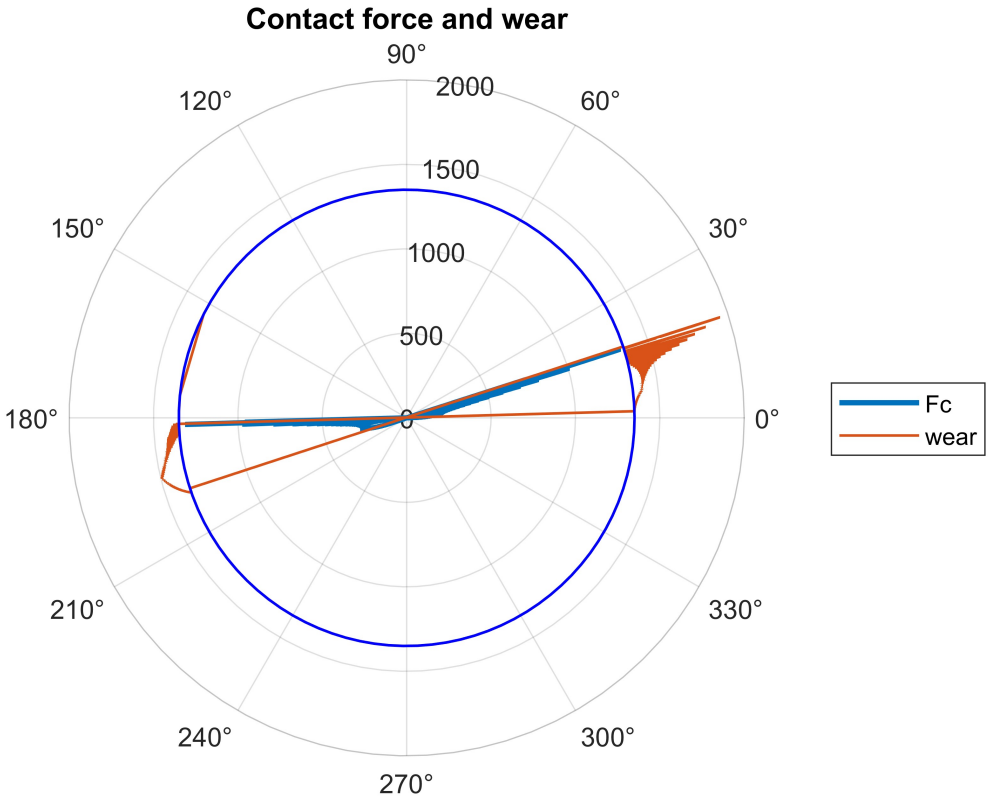


**Figure 5.5:** Contact force and a indicator of wear in a polar plot

force has also been included to show that wear is present only in the area where contact occurs. However, the most significant wear does not necessarily happen near the zone of maximum contact force. In fact, in the elongation phase of the actuator, which is the phase where the contact in the polar plot happen on the left, the maximum wear does not correspond to the maximum contact force, probably because the relative sliding of the two surfaces in that area is very low. While during the return phase of the actuator the maximum wear correspond to the maximum contact force. The polar plot graph shown in Figure 5.4 is also useful for understanding if the contact force is calculated correctly. Below, in Figure 5.6, the trend of the contact force is shown, and in the same figure, a polar plot graph is included where the two phases of actuator extension and retraction are distinctly highlighted with different colors. Throughout the entire extension phase,

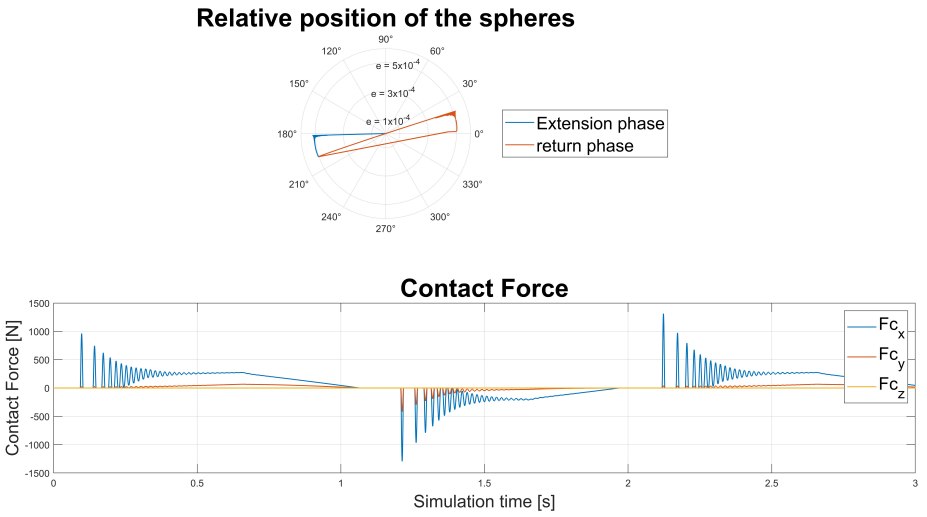


**Figure 5.6:** Andamento contact force

represented by the blue curve in the polar plot graph, one would expect the x and y components of the contact force to be positive, and in fact, this is the case. At the beginning of this phase, the contact force is predominantly along the x-axis, but then the contribution along the y-axis increases as shown in the polar plot, indicating movement towards higher angles. As we move towards higher angles, the influence of the y-axis component increases because it's important to remember that the contact force is always perpendicular to the point of contact between the two spheres.Conversely, during the retraction phase, represented by the red curve, one would expect the contact force to be negative based solely on the polar plot, and this trend is confirmed by observing the contact force graph. Finally, the last component of the kinematic chain to consider is the force exchanged between the inner sphere and the flight control surface, whose connection is also schematized with a spring. In the case of the spring connecting the inner sphere with the flight surface, it generates a positive force when the spring is extended and a negative force when compressed, as defined in the model. Therefore, during the extension phase of the actuator, one would expect the spring force to be negative because the inner sphere will be moved due to contact with the outer sphere, causing the end of the spring to which it is connected to compress. This compression force will then cause the flight control surface to move by a certain angle. Conversely, during the retraction phase of the actuator, the spring will tend to elongate, generating a positive force. The behavior of the spring just described can be verified in Figure 5.7, where the actuator position input trend is also shown to facilitate following the previous discussion. One last parameter that should be shown is the trend of the moments generated by the three-dimensional springs to prevent the sphere

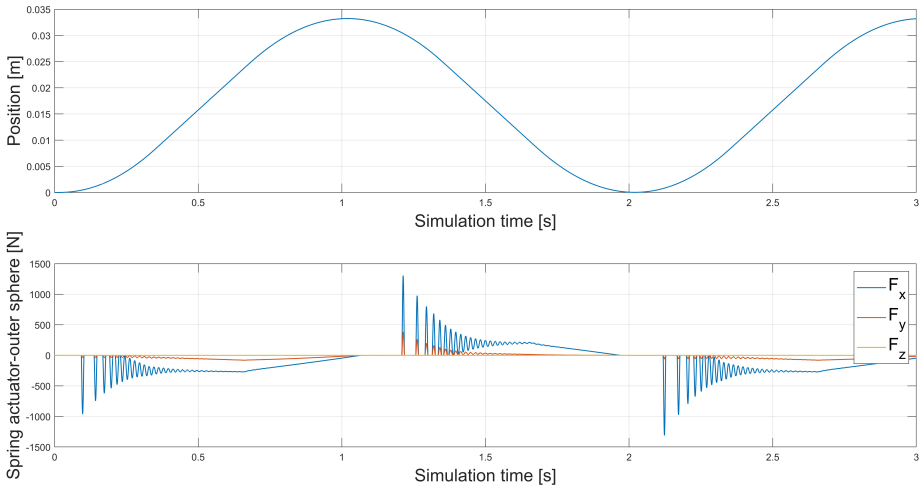


**Figure 5.7:** Inner sphere-surface spring force

from rotating around its own axis. The trend of the moment relative to the spring connected to the outer sphere will be shown in Figure 5.8. The analysis of the graph will be the same for the moment of the spring connected to the inner sphere, so it will be omitted. The figure also depicts the trend of the angle relative to

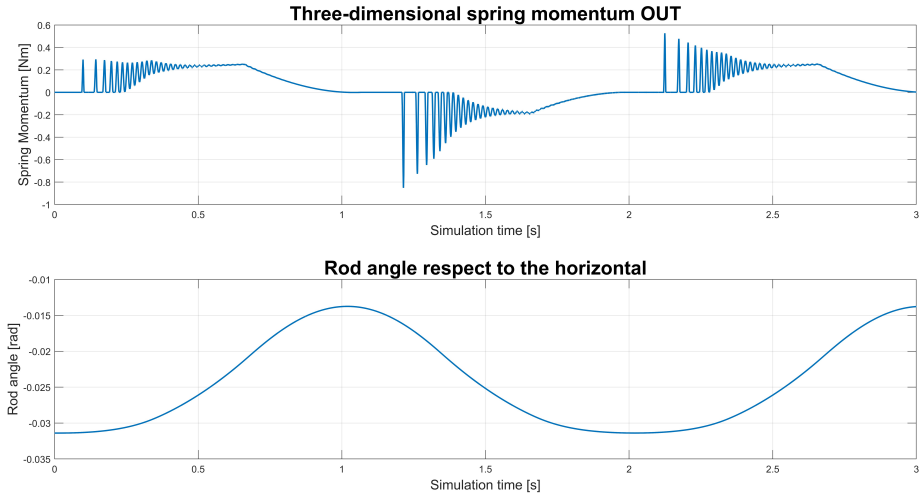


**Figure 5.8:** Outer spring momentum

the horizontal of the rod on which the actuator is positioned. It's important to clarify that a positive moment corresponds to a counterclockwise rotation. From

the graph, it can be observed that an increase in the inclination angle of the rod corresponds to a positive moment of the spring, which generates a counterclockwise rotation. The trend of the moment is correct because, as the inclination angle of the rod increases, if there were no spring, the sphere would remain stationary without rotating around its center of rotation. However, in reality, it should rotate counterclockwise as it is fixed to the rod. In fact, the outer sphere cannot rotate around its own center of rotation, but it must follow the inclination of the rod relative to the horizontal. The opposite reasoning applies when the inclination angle of the rod decreases. In conclusion, it's important to note that despite all the graphs above showing the expected results, the model results are not perfect. There are numerical errors apparent when looking at the components along the axes of the contact force. As you can see, the contact force has a component along the z-axis, which should not exist since the contact is in the plane. This can be considered a numerical error, given the negligible influence of the force along the z-axis; its magnitude is small, and therefore, its impact on the model results will also be minor. With the analysis just completed, we cannot yet declare that the

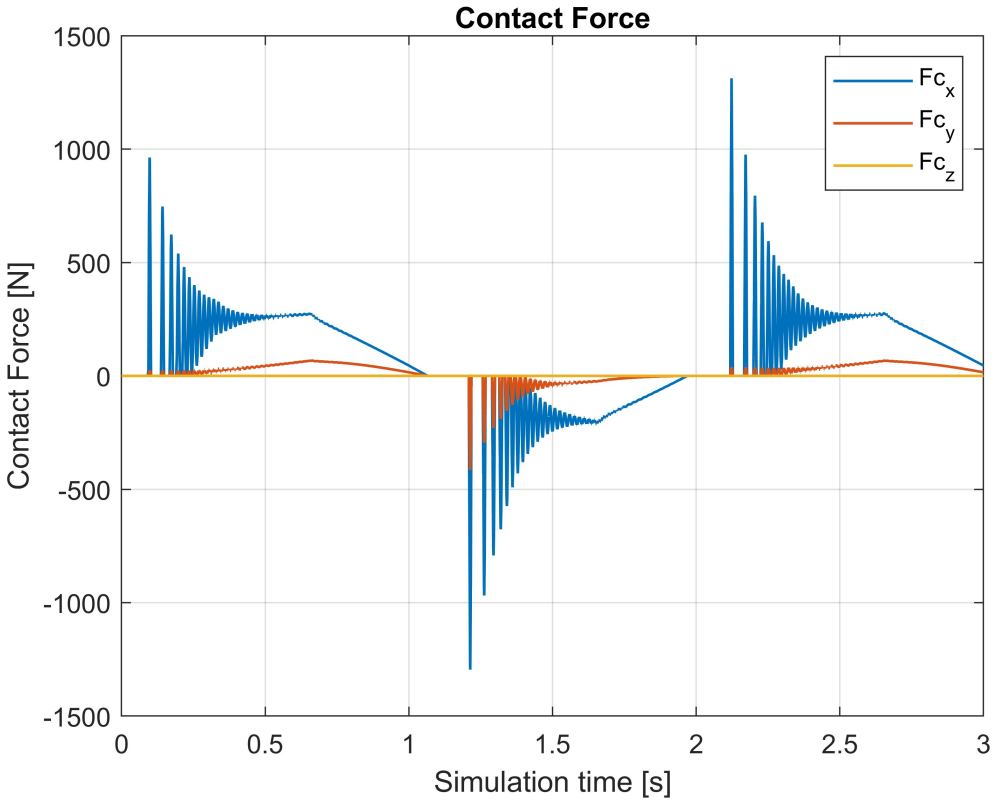


**Figure 5.9:** Contact force along the three axis

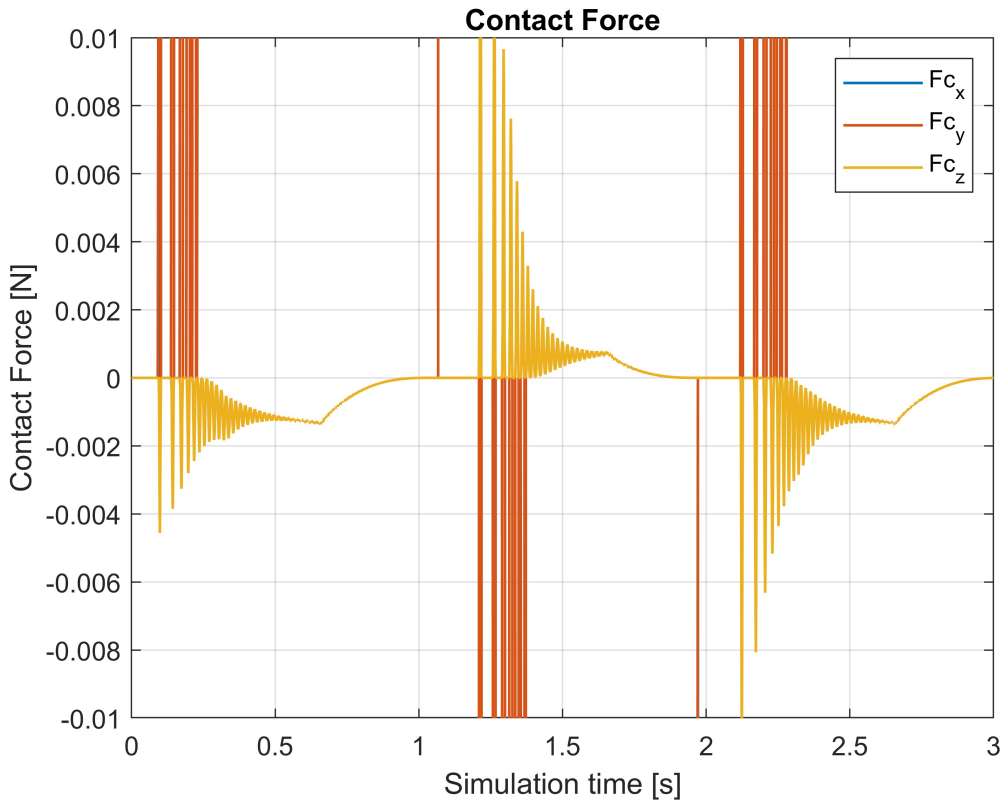


**Figure 5.10:** Zoom of the contact force along the three axis

model works correctly conclusively. Although the obtained results are consistent with expectations and provide a good understanding of the phenomenon under consideration, further evaluation of the model is necessary to confirm its validity and accuracy.

## 5.2 Clearance variation

The first parameter we decided to vary is the clearance within the rod-end. Looking at Figure 5.2, one might expect that decreasing the clearance could negatively affect the behavior of the rod-end. Indeed, from the eccentricity graph, it can be seen that the eccentricity oscillates quite widely, and reducing the clearance might lead to a "bounce" of the inner sphere within the outer sphere. In other words, it could happen that after the inner sphere comes into contact with the outer sphere, it experiences a force so significant that it pushes it into contact with the opposite part of the outer sphere, thus preventing the correct functioning of the mechanism.

However, as observed from the results, this does not occur. In fact, the oscillation of eccentricity decreases as the clearance decreases, as shown in Figure 5.11. With

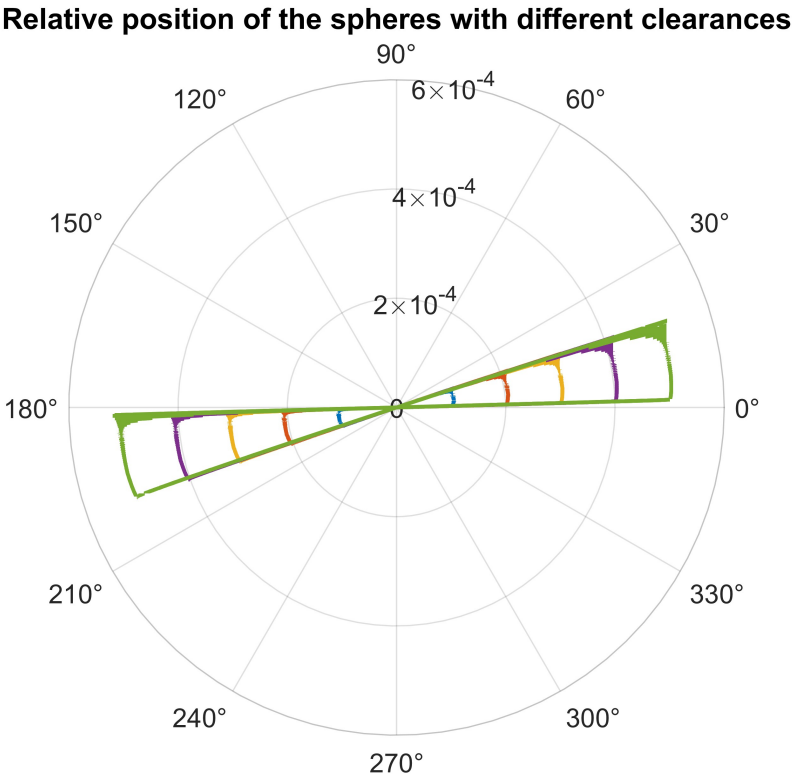


**Figure 5.11:** Polar plot with different rod-end clearances

a smaller clearance, the outer sphere has to travel less distance before reaching contact. Therefore, one would expect the contact to occur earlier compared to a situation with a larger clearance. The reduced time spent before the first contact means that the velocity of the outer sphere is lower as the clearance decreases. This happens because the acceleration of the outer sphere is constant for every value of the clearance before the first contact occurs. Since the contact happens earlier for a smaller clearance, this translates to a lower velocity. In Figure 5.12, you can observe the trend of the acceleration of the outer sphere before contact as the clearance varies. Having a lower velocity of the sphere results in a lower contact force, particularly the damping force component. This is because it is directly dependent on the velocity difference between the two spheres composing the rod-end. In Figure 5.13, the trend of the component of the contact force due to damping is shown. Specifically, the force values obtained at the first contact are highlighted with an arrow as the clearance varies.

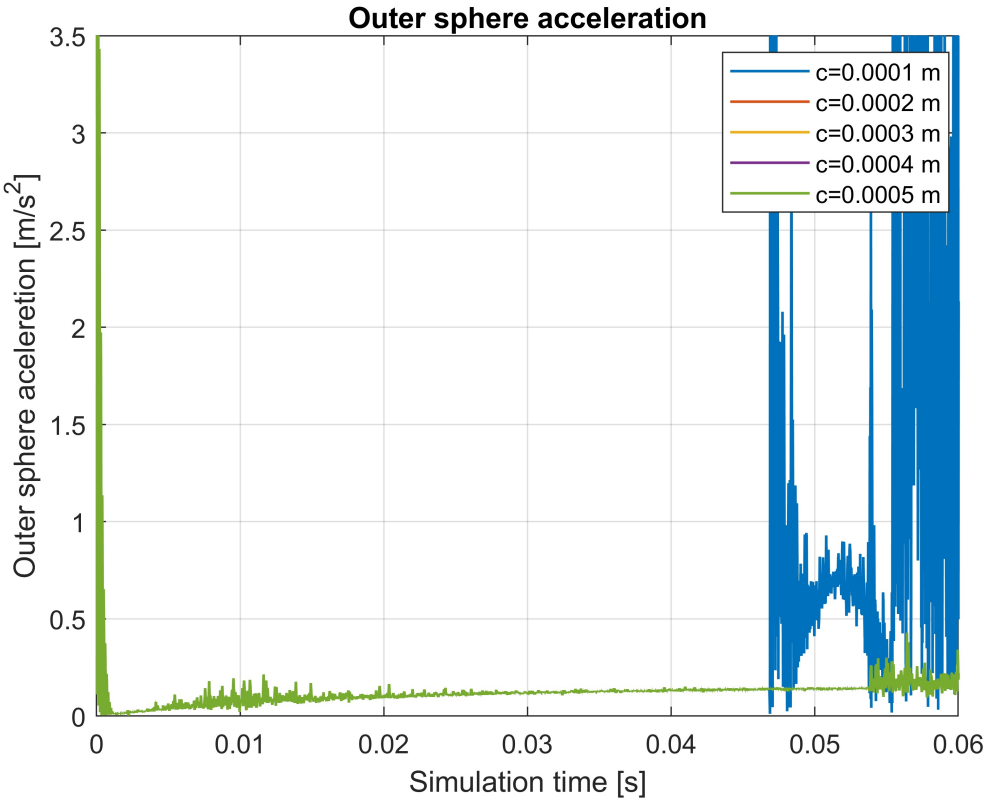


**Figure 5.12:** Outer sphere acceleration before the first contact

Therefore, having a lower damping force also results in a lower contact force and thus a smaller penetration between the two spheres. With less penetration between the two spheres, there will be a smaller oscillation of eccentricity as the clearance of the rod-end decreases. The graph of the contact force is shown in Figure 5.14, where, as with the damping force, the force values due to the first contact are highlighted with arrows as the clearance varies. In combination with the graph showing the contact force, a plot (Figure 5.15) illustrating how the contact force decreases with decreasing clearance is included. In particular, the first peak value of the contact force is considered significant. Additionally, the eccentricity graph is provided in Figure 5.16 for better understanding, although its trend can be partially inferred from the polar plot in Figure 5.11. As a final consideration, it's necessary to examine how the change in clearance reflects on the positioning of the flight control surface. With a decrease in clearance, as one might easily imagine, the outer sphere will come into contact with the inner sphere earlier. Consequently, the angle $\theta$ and hence the position of the flight surface will change earlier (the actuator will need a smaller elongation to establish contact). This can be observed

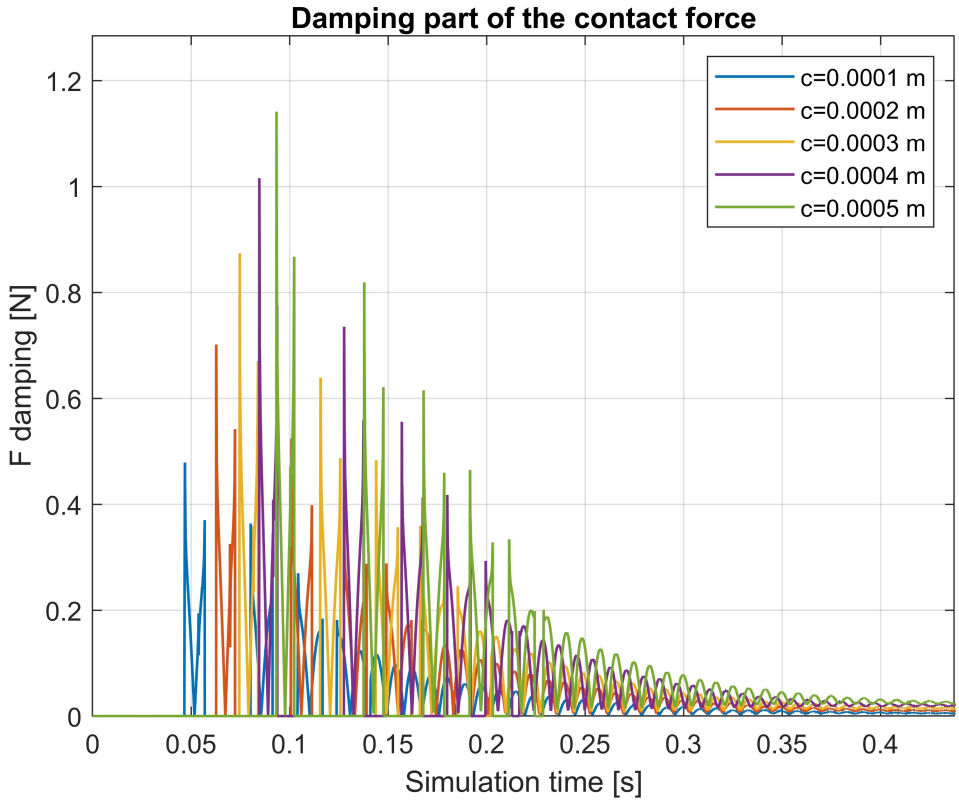


**Figure 5.13:** Forza dovuta allo smorzamento

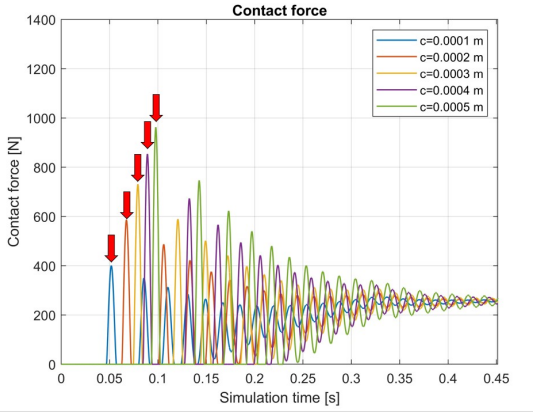


**Figure 5.14:** Contact force with different clearance

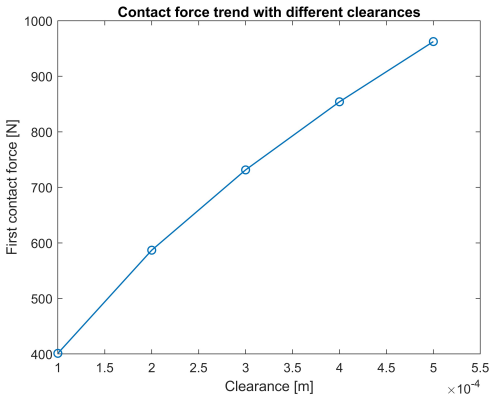


**Figure 5.15:** Trend contact force with different clearance

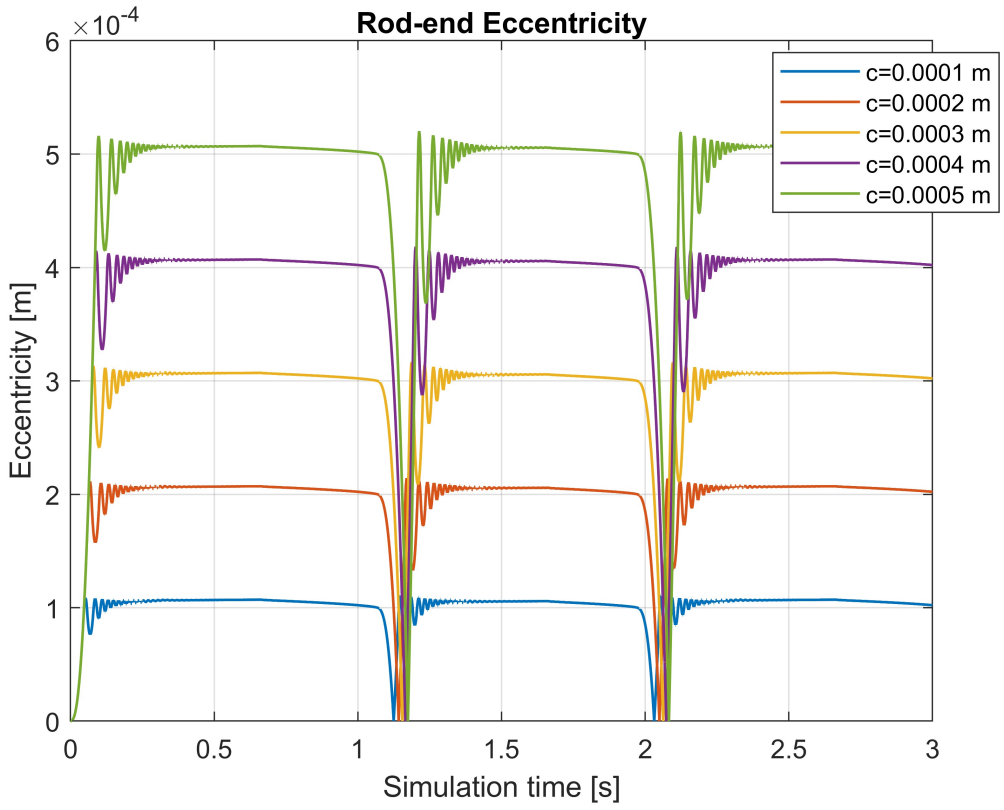


**Figure 5.16:** Rod-end eccentricity with different clearances

in Figure 5.17. It's observed that the situation with smaller clearance will have achieved a greater angle of the flight surface. This is because, having initiated contact earlier, the actuator will have a longer stroke during which the two spheres are in contact, resulting in a greater movement of the inner sphere of the rod-end. This is illustrated in the third graph of Figure 5.17. Similarly, it's evident that in the situation with smaller clearance, the angle $\theta$ decreases earlier compared to situations with higher clearances. Lastly, in the fourth graph of Figure 5.17, it's shown how, upon starting a new ascent phase, the rod-end with less clearance will always have the flight control surface moving first, just as it did at the beginning, thus repeating the described cycle.

## 5.3 "Initial position" variation

Finally, as the last parameter, we decided to vary the initial position of the outer sphere by modifying the "Initial condition" parameter mentioned at the beginning of

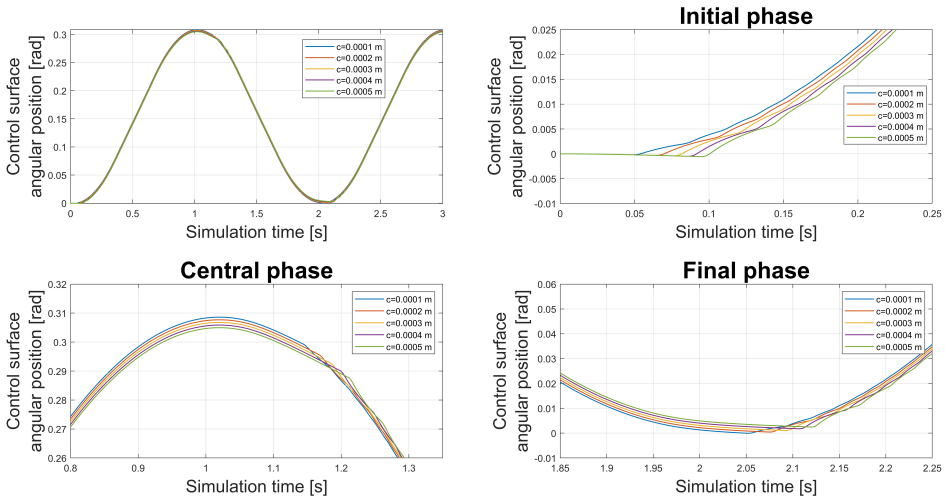


**Figure 5.17:** Surface angle with different clearance

the chapter. By altering the initial position, we simulate the behavior of the rod-end under conditions where the two spheres have not been mounted concentrically, but rather under conditions where there may have been assembly with some errors, for example. The initial position of the outer sphere was varied only along the z-axis exiting the plane to analyze the correct 3D functioning of the model, which so far has been tested only in the xy-plane. The result of varying the initial z-coordinate is shown in Figure 5.18, where it can be observed that the three-dimensionality of the model has been implemented correctly, as the constraint of the sphere is respected. Other figures that can better clarify the 3D behavior of the model are Figure 5.19 and Figure 5.20, where the representation on the xy-plane and the xz-plane of Figure 5.18 is shown. From the 3D decomposition into two planes, it's even clearer how the three-dimensionality of the model has been correctly constructed. From the xy-plane, it can be seen how the trajectory of the inner sphere becomes narrower as the value of the applied initial condition increases. This is quite obvious because as the z-coordinate increases, the radius of the circular crown decreases. From the xz-plane, a particular behavior can be observed as the z-coordinate increases. The trajectory of the inner sphere remains linear, i.e., it stays at the same z-level, until it comes into contact with the outer sphere, where the trajectory bends and tends to follow the curvature of the outer sphere. This is due to the presence of a contact force that is oriented in space, given that the contact between the two spheres does not occur at the z-coordinate equal to the applied "Initial condition."

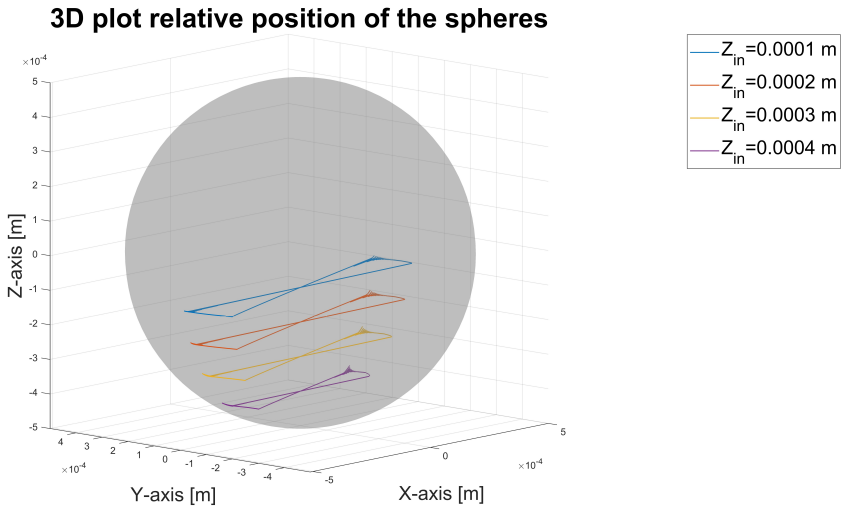


**Figure 5.18:** 3D plot

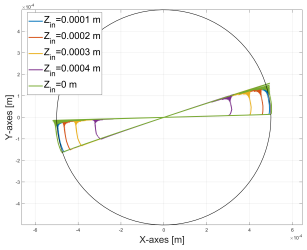


**Figure 5.19:** Contact force with different clearance

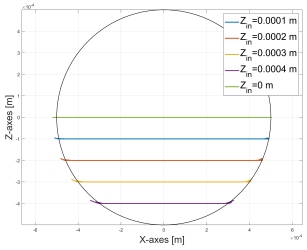


**Figure 5.20:** Trend contact force with different clearance

# Chapter 6

# Actuator model

The actuator model utilized in this thesis has not been subject of study. However, since it has been used in simulations and since there will be results displaying certain parameters, it is necessary to describe at least partially the functioning of the model. In this chapter the actuator model will be discuss briefly, for more specific information refer to the article [15] and [16]. The actuator in question is a hydraulic actuator driven by a jet-pipe servovalve, which is actuated using solenoids. The position of the actuator's rod is measured using an LVDT (Linear Variable Differential Transformer), and subsequently, the sensor feedback is compared with the input given to the system. Upon finding the error, a PI controller is utilized to actuate the servovalve. The complete model of the actuator is depicted in Figure 6.1.

## 6.1 Servovalve

We begin by analyzing the operation of the servovalve in order to proceed as faithfully as possible in how the information is transmitted within the model. The servovalve, by definition, consists of two stages: a pilot stage, which in this case is composed by a torque motor, and a main stage responsible for the movement of the spool. A schematic diagram of the entire valve can be seen in Figure 6.2. As can be seen from the figure, the torque motor is actuated by two solenoids positioned on both sides of the torque motor. When a solenoid is energized, an electromagnetic flux is created, which interacts with the nearby armature of the torque motor and the air gap between them, generating a force that tends to reduce the air gap and thus creating a torque. Specifically, the force generated is called reluctance force and it is given by the following equation:

$$F = \frac{1}{2}\frac{B^2}{\mu}S \tag{6.1}$$

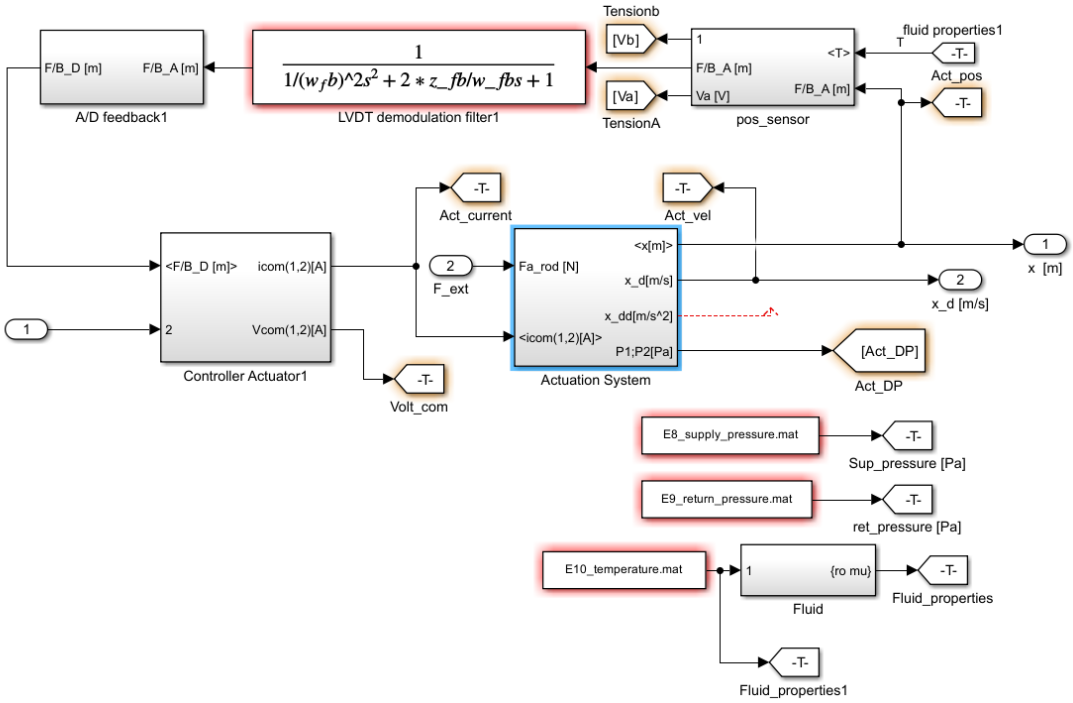


**Figure 6.1:** Simulink actuator model

where $B$ is the magnetic induction, $\mu$ is the permeability, and $S$ is the solenoid's cross-sectional area. The torque generated by the reluctance force will tend to rotate the torque motor by a certain angle, but it must overcome some resisting forces, so a balance in rotation is necessary. In addition to the electromagnetic torque, there is also the torque due to the resistance opposing the feedback wire. The feedback wire is connected at one end to the jet-pipe and at the other end to the spool. In the model, it is represented as a spring, and thus depending on the position of the jet-pipe $X_j$, it will generate a resisting torque. Furthermore, the hinge around which the flapper rotates is modeled with a resisting action, which is schematized as rotational stiffness and damping, this way of modeling the hinge is useful to centering the jet-pipe especially in the presence of clearance. We therefore obtain the following torque equilibrium equation.

$$C_{mg} - k_f x_F - b_f \dot{x_j} - (x_s + x_j)k_W = J_A \ddot{x_j} \tag{6.2}$$

The quantities in the equation can be seen in Figure 6.2. By dividing the rotating mass of the system, we can find the acceleration with which the jet-pipe rotates. Through double integration, we can then find the position $X_j$ of the jet-pipe, which is responsible for the subsequent actuation of the valve spool. When the jet-pipe rotates allow the flux to pass through one of the two different command canal

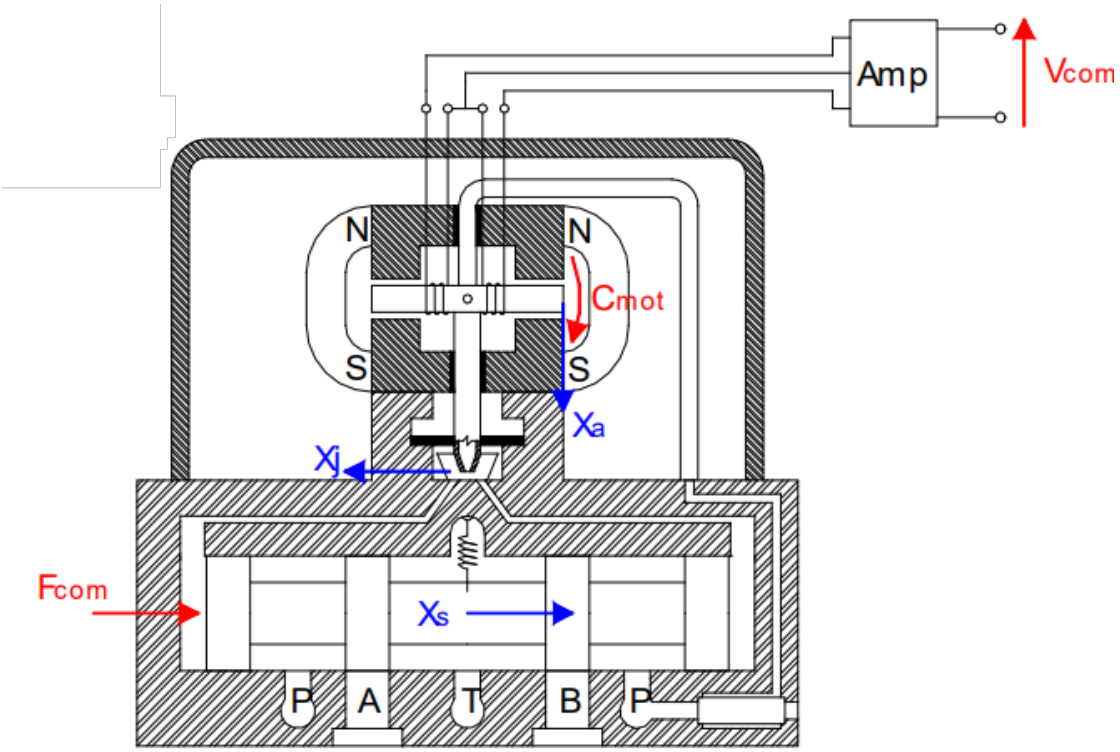


**Figure 6.2:** Servovalve scheme

(figure number 6.3) in order to generate pressure on the right or left spool activation. Once the pressure difference between the two activations of the servovalve spool is

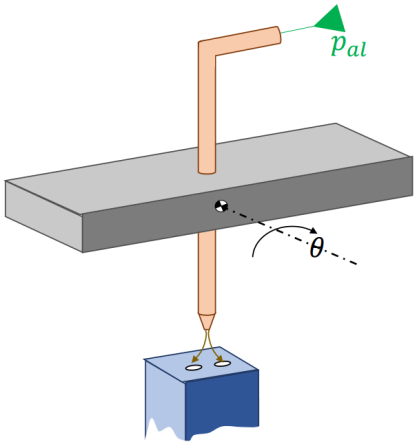


**Figure 6.3:** Jet-pipe scheme

found, it is possible to determine the position of the spool. To find the position of the spool, we need to balance the forces in order to find the spool's acceleration, and consequently its speed and position. Firstly, the spool is acted upon by the pressure from the two activations. In Simulink, the pressure difference is directly multiplied by the area of the spool on which the pressure acts. Similar to the equilibrium for the rotation of the jet-pipe, there is also the force due to the feedback wire, which tends to bring the spool back to its initial position. The resisting force of the feedback wire is schematized as in Equation (6.2). Finally, as shown in Figure 6.4, when the spool is not in its initial position, the flow pass through it from the supply to the load and the flow pass through it from the load to the tank also generate a force on the servo valve spool, as the fluid passing through the servo valve is under pressure. The equation governing the dynamic equilibrium of the spool is therefore as follows:

$$dPA_s - (x_j - x_s)k_W + F_{fl1} + F_{fl2} - F_{fr} = m_s\ddot{x}_s \tag{6.3}$$

where $F_{fl1}$ and $F_{fl2}$ are the forces due to the flow passing through the valve. Now

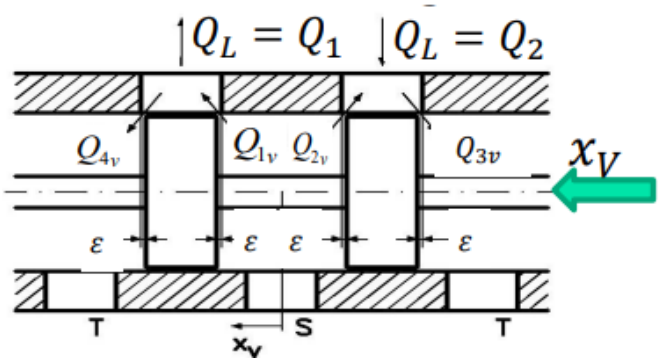


**Figure 6.4:** Spool scheme

that the displacement of the valve spool has been determined, it is necessary to calculate the fluid flow that will flow into the actuator chambers and, conversely, into the tank. In general, the spool is seen as a hydraulic Wheatstone bridge between the supply and the tank, so the pressure drop between the actuator chambers and the discharge or supply generates a flow which is a function of a hydraulic resistance. The hydraulic resistance varies depending on the presence of laminar flow or turbulent flow, but in this case, the hydraulic resistance is calculated as if there were permanently turbulent flow. We can then calculate the flow passing through each port of the spool, and as shown in Figure 6.4, the flow rates into the rear and front chambers of the cylinder will be equal to:

$$Q_1 = Q_{1v} - Q_{4v} \tag{6.4}$$

$$Q_1 = Q_{3v} - Q_{2v} \tag{6.5}$$

where the flow rates $Q_{iv}$ are calculated as follows:

$$Q_{iv} = C_{di} A_i \sqrt{2 \frac{\Delta P_i}{\rho_i}} \tag{6.6}$$

### 6.1.1 Actuator

Once the fluid flow rates into the two chambers of the actuator are obtained, it is possible to calculate the pressure of the fluid acting on the movable surface of the actuator, in order to then determine how much the actuator has extended or retracted. A schematic diagram of the actuator is shown in Figure 6.5. To find the

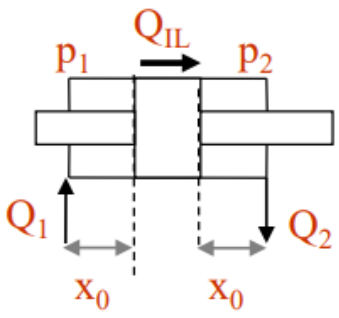


**Figure 6.5:** Actuator scheme

pressure acting on the movable surface of the cylinder, the equation of continuity is applied, which corresponds to:

$$\rho(\sum Q_{IN} - \sum Q_{OUT}) = \frac{dm}{dt} = \frac{d(\rho V)}{dt} = V\frac{d\rho}{dt} + \rho\frac{dV}{dt} \tag{6.7}$$

The volume of the actuator chambers is not constant but varies over time, and it is calculated as follows:

$$V_1 = V_{10} + A_c x \tag{6.8}$$

$$V_2 = V_{20} - A_c x \tag{6.9}$$

where $V_{10}$ and $V_{20}$ are the volumes of the two chambers when the movable surface of the actuator is positioned at zero. The position of the movable surface is considered positive when the actuator extends, and thus when the surface moves to the right; by choosing this direction as positive, the volume surface due to the movement of the movable surface will be added to chamber 1 and subtracted from chamber 2. Furthermore, if we have a fluid with a volume $V$ and pressure $P$, and we reduce

it by an amount $dV$, there will be an increase in pressure $dP$ proportional to the modulus of fluid compressibility $\beta$.

$$\frac{dV}{V} = -\frac{d\rho}{\rho} = -\frac{dP}{\beta} \tag{6.10}$$

So substituting equations (6.8), (6.9), and (6.10) into equation (6.7), we get the following equations respectively for chamber 1 and chamber 2:

$$Q_1 - A_c\dot{x} = \frac{V_1}{\beta}\frac{dP_1}{dt} \tag{6.11}$$

$$-Q_2 + A_c\dot{x} = \frac{V_2}{\beta}\frac{dP_2}{dt} \tag{6.12}$$

From which it is possible to derive the trend of the pressures acting on the movable surface of the actuator respectively of chamber 1 and chamber 2. In the equation, the leakages present in the actuator have been neglected; in fact, part of the fluid can pass through the seal that separates the two chambers, and there may also be leakages external to the actuator. All leakages have been considered in the Simulink model of the actuator, the scheme of this specific part of which is shown in Figure 6.6. Now that we know the pressures in the two chambers, we can perform

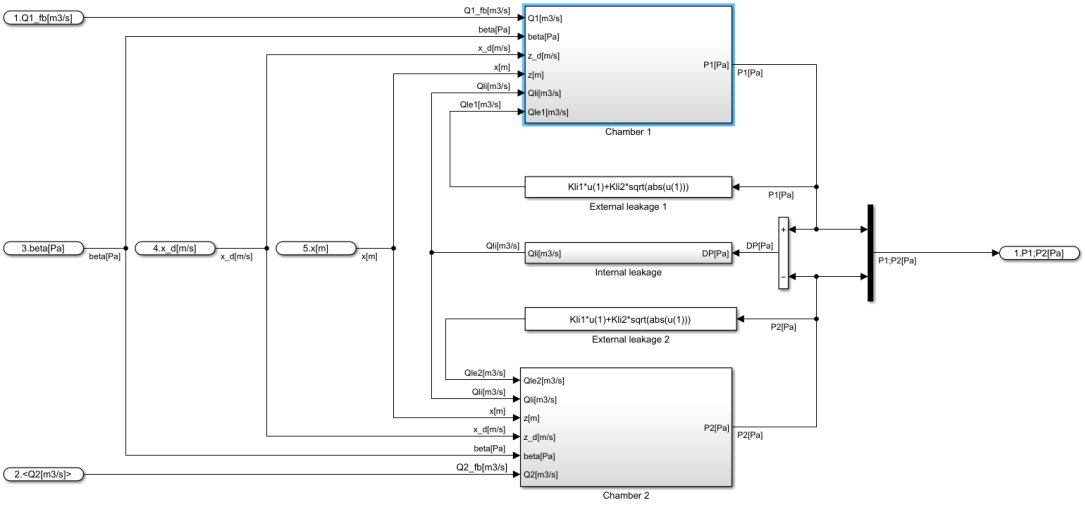


**Figure 6.6:** Simulink scheme where the pressure of the two chamber of the actuator is calculated

the dynamic equilibrium of the actuator. A scheme with the acting forces is shown in Figure 6.7. From the figure, we can derive the dynamic equilibrium, which corresponds to:

$$(P_1 - P_2)A_c - m\ddot{x} - \gamma\dot{x} + F_{ext} = 0 \tag{6.13}$$

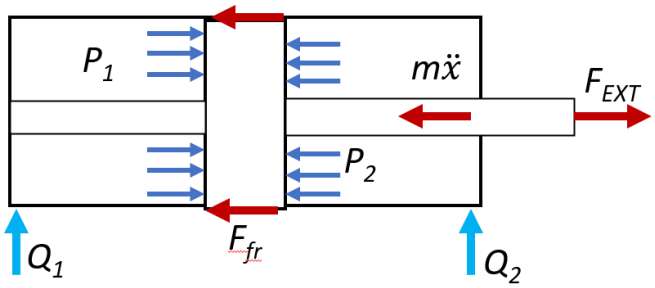


**Figure 6.7:** Actuator forces scheme

where $\gamma$ represents the coefficient of viscous friction. From the equation of equilibrium, we can then obtain the acceleration, and then by integrating, we can find the position of the actuator stem, since it will be the output of the model. The implementation of the dynamic equilibrium of the actuator in Simulink is shown in Figure 6.8.

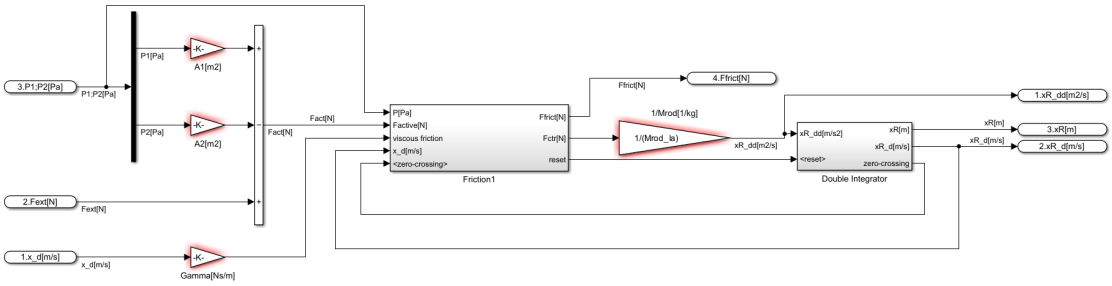


**Figure 6.8:** Simulink implementation of the dynamic equilibrium of the actuator

## 6.2 Actuator calibration

Before performing simulations of the model with the actuator, it is necessary to calibrate it. Actuator has already been calibrated but with a different downstream system, so the procedure needs to be repeated. To calibrate the actuator, the actuator model is isolated, and to simulate it being connected to the actuation system, a parameter called "equivalent mass" is introduced. This parameter simulates the dynamics of the downstream system as if it is connected. The equivalent mass is added to the movable mass of the actuator and is a way to concentrate the mass and inertia of the flight control surface directly at the end of the actuator. To do this, it is necessary to find the transmission ratio of the crank-rocker mechanism used to move the flight surface. The transmission ratio found for the mechanism in this

thesis, with the data shown in Chapter 4, is shown in Figure 6.9. As can be seen

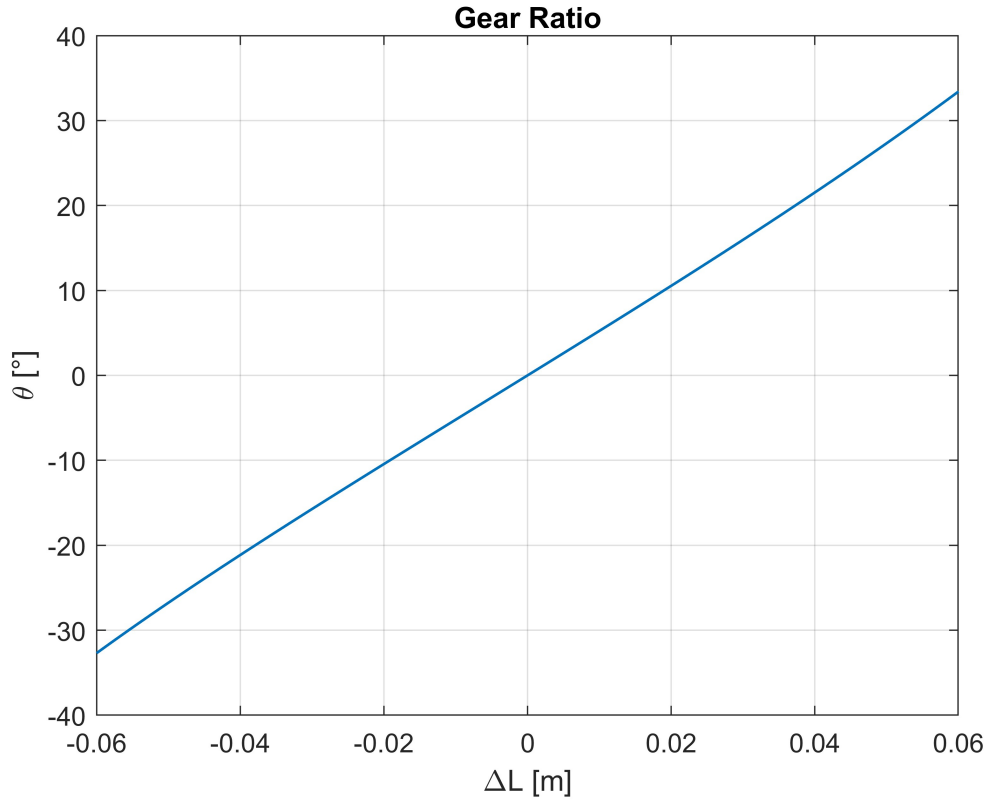


**Figure 6.9:** Gear Ratio

from the figure the transmission ratio is not a constant, in fact the figure doesn't show a straight line. This means that an average value of the transmission ratio will be used to find the equivalent mass, an approximation that will not significantly affect the results given the nearly linear behavior of the transmission ratio graph. Once the equivalent mass is calculated using the average transmission ratio just found, the actuator calibration can proceed. In this thesis, the Ziegler-Nichols method is used for calibration, which consists of the following steps: a step input position is applied to the system, and the proportional gain is increased until an overshoot is obtained in the system's output. Once the overshoot is achieved, the integral gain is increased to reduce the steady-state error of the system. In this work, the values of the integral and proportional gains obtained are respectively 0.02 and 2 A/m. The response obtained with the mentioned gains is shown in Figure 6.10.

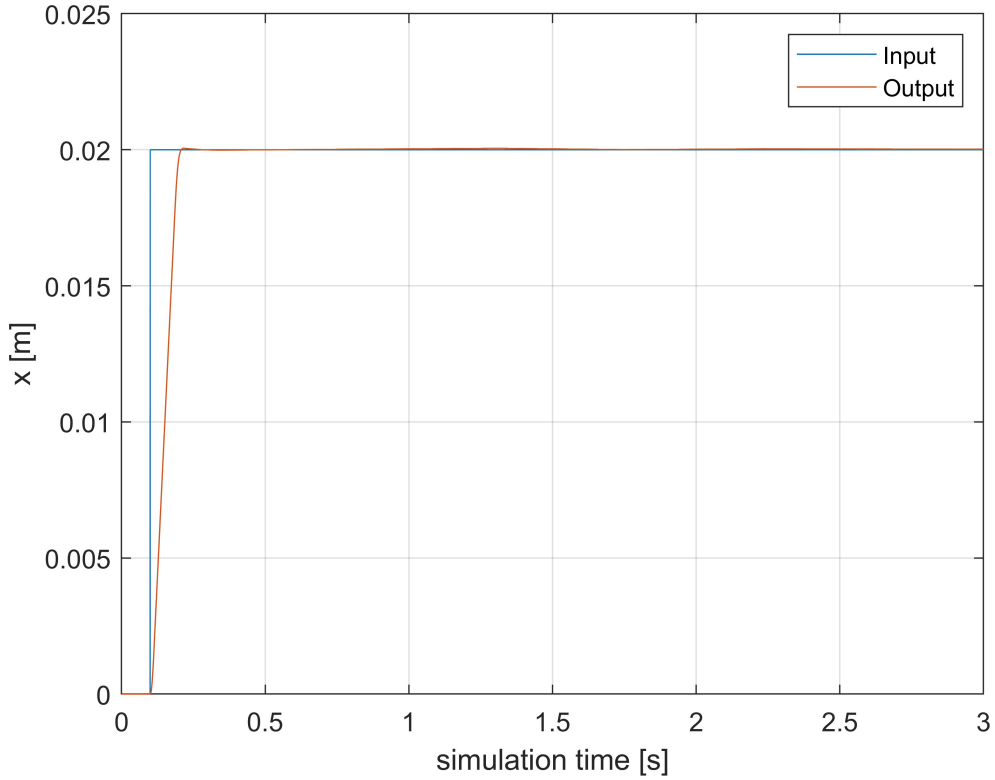


**Figure 6.10:** Actuator calibration

## 6.3 Results with the actuator model

The first step after calibrating the actuator is to verify that the results returned by the rod-end model are compatible with those of the model with both actuator and rod-end. Indeed, since the rod-end model has already been validated, it will serve as a verification function for the correct operation of the model with the implementation of both the actuator and the rod-end. To do this, the same position input is provided to both the rod-end model and the model with the actuator inserted, in order to have the most accurate comparison possible. Since the input required by the actuator model is position while for the rod-end model it is velocity, the position and velocity input trends are shown in Figure 6.11 to demonstrate that they are indeed equal to each other.

No significant difference can be observed between the inputs, so the analysis of comparison between the two models proceeds. The first graph chosen to be displayed in Figure 6.12 shows the trend of eccentricity and contact force. This graph is shown because it is the most significant for the correct operation of the

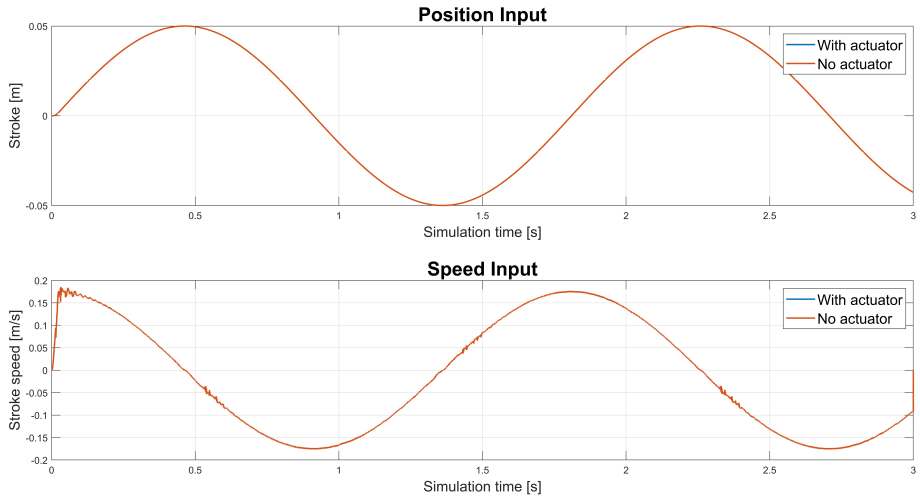


**Figure 6.11:** Position and speed input with and without the actuator

model, and as can be seen, the trend of the model with the actuator reflects the trend of the model without it. It can be noticed that with the insertion of the

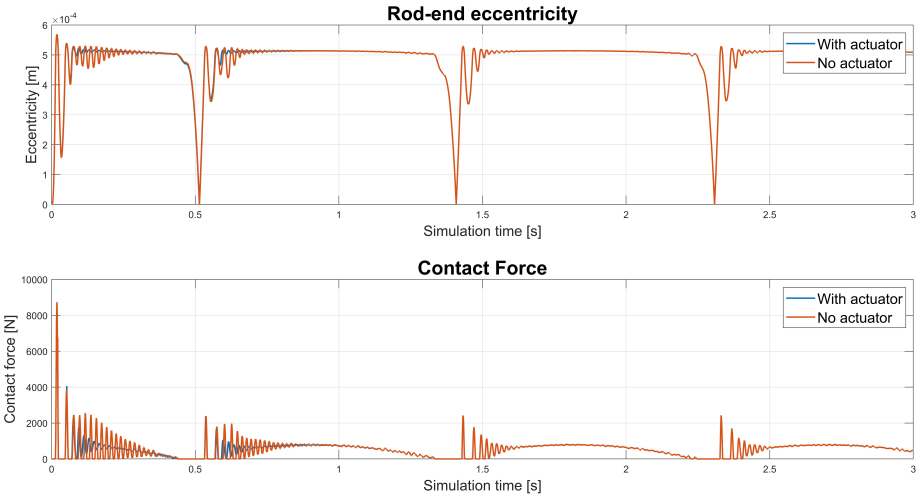


**Figure 6.12:** Eccentricity and contact force with and without the actuator

actuator, the eccentricity and consequently the contact force exhibit less oscillation. This is due to the presence of the actuator, which plays a significant damping role within the entire system. The damping effect of the actuator can also be observed in the forces of the three-dimensional springs of the mechanism. Indeed, both the

spring connected to the outer sphere and the spring connected to the inner sphere exhibit a more damped force. In both cases, at the top of the graphs, one can observe how the trend of the three components respects the direction of the force. The graphs of the force of the outer spring and the inner spring are respectively shown in Figure 6.13 and 6.14. As a final graph, a polar plot showing the reciprocal

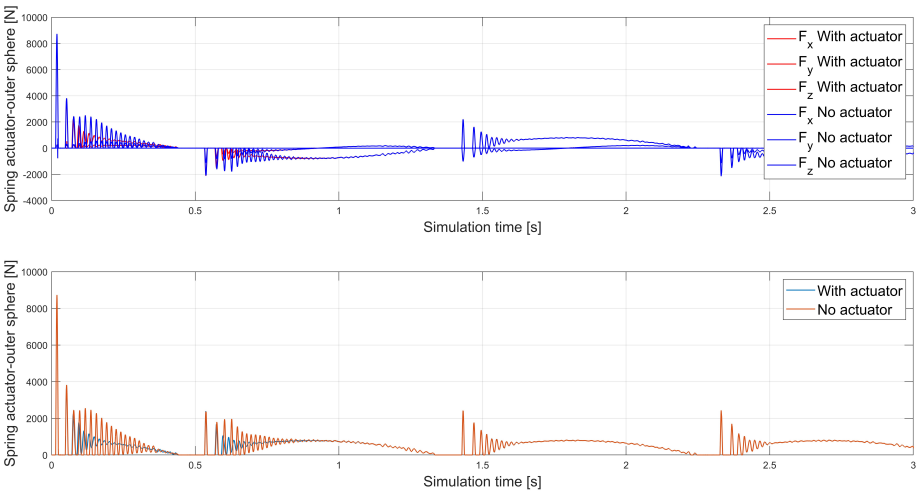


**Figure 6.13:** Outer spring force with and without the actuator

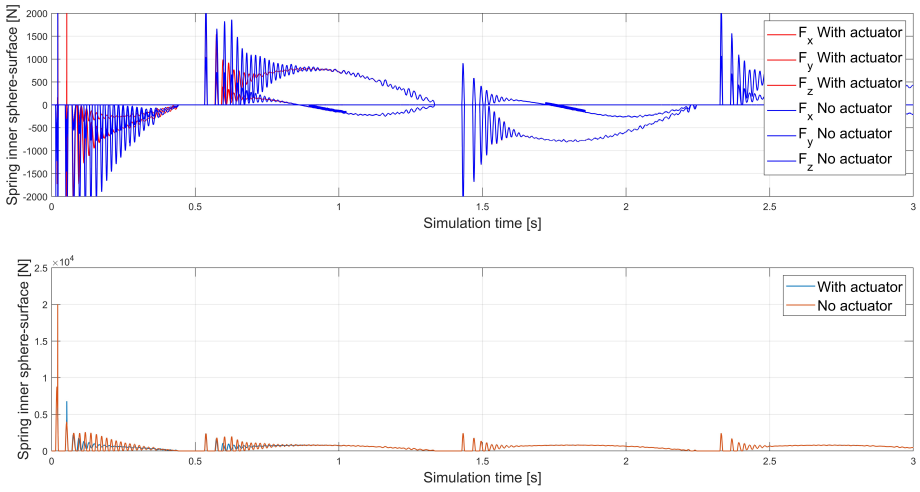


**Figure 6.14:** Inner spring force with and without the actuator

position of the two spheres is included in Figure 6.15. Once again, the behavior of

the model with the actuator adheres to the expected trends. Therefore, it can be concluded that the implementation of the actuator in the model with the rod-end has been successful. After verifying the correctness of the actuator implementation

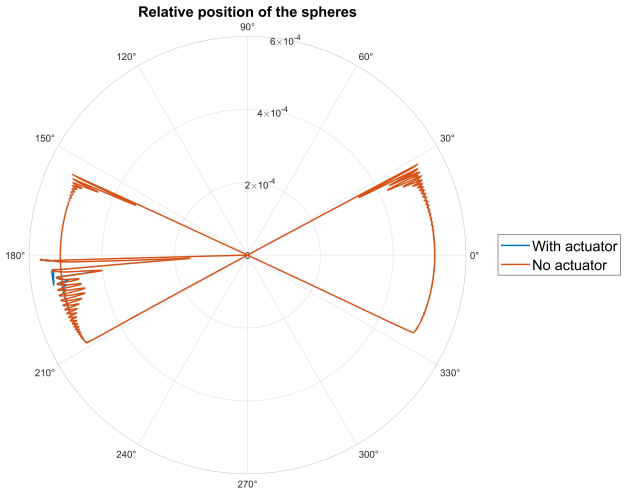


**Figure 6.15:** polar plot with and without the actuator

with the rod-end model, analyses can be conducted varying certain parameters such as clearance or the application of a force on the flight surface.

### 6.3.1 Analysis of the model as the rod-end clearance varies

This analysis has already been conducted for the rod-end alone in Chapter 5, therefore, this section will examine different quantities. Given the presence of the actuator in this section, we will discuss how the variation of clearance affects actuator-related quantities such as pressure, flow rate, etc. To perform the analysis varying the clearance, we decided to proceed backward with the flow of information. That is, instead of starting from the information of the controller, we start from the actual result of the entire system, which is generating a movement of the rod due to a pressure difference between the two chambers of the actuator. Therefore, the first trend shown is that of the pressure in the rear chamber of the cylinder, which is the pressure that generates the movement of the rod, shown in Figure 6.16. The pressure in the rear chamber increases during the extension phase of the actuator and decreases during the retraction phase. From the figure, it is evident how the pressure trend is influenced by the clearance value of the rod-end. With smaller clearance values, there are also lower pressures during the extension phase. This is due to a smaller contact force in the presence of smaller clearance, as seen in Chapter 5. Therefore, with a smaller contact force between the two spheres,

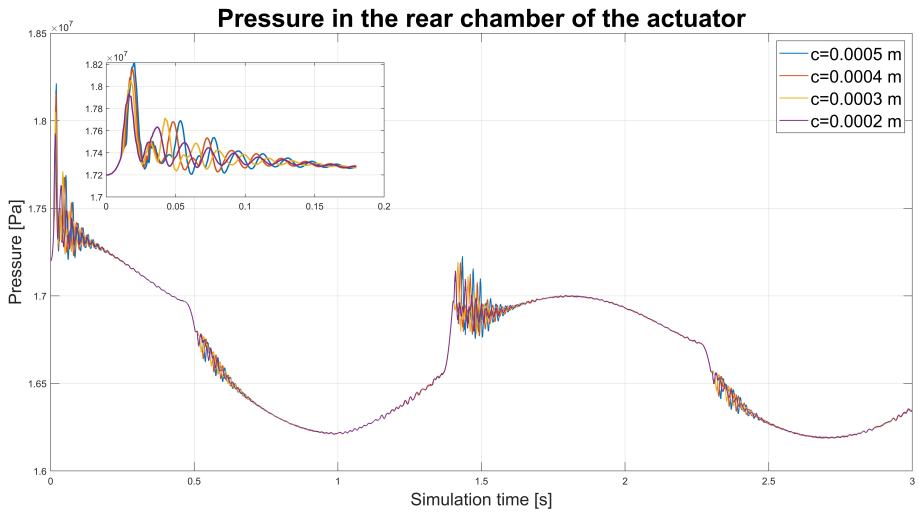


**Figure 6.16:** Rear chamber pressure

a lower pressure is required to allow the rod to extend. In Figure 6.17, you can observe the trend of the external force acting on the actuator rod, which is also influenced by the rod-end clearance. Indeed, the external force acting on the rod is simply the transposition of the contact force between the two spheres observed by the actuator. The external force in the figure is negative during the extension phase of the actuator, while it is positive for the retraction phase. The trend of

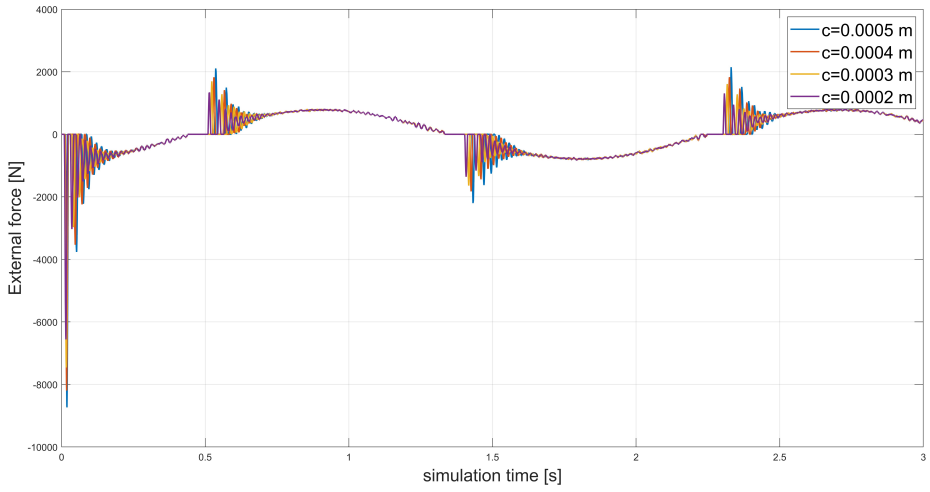


**Figure 6.17:** Actuator external force

the pressure acting in the front chamber of the actuator is also influenced by the rod-end clearance in the same way as the pressure in the rear chamber, but the influence of the clearance becomes more evident during the retraction phase of the rod. In this phase, the pressure in the front chamber can be considered as "driving." The trend of the pressure in the front chamber of the actuator can be seen in Figure 6.18, while Figure 6.19 shows the trend of both pressures, with the pressure in the front chamber represented by the dashed line. This representation allows us to immediately see the pressure difference responsible for the movement of the rod. The increase in pressure in the two chambers of the actuator is due to

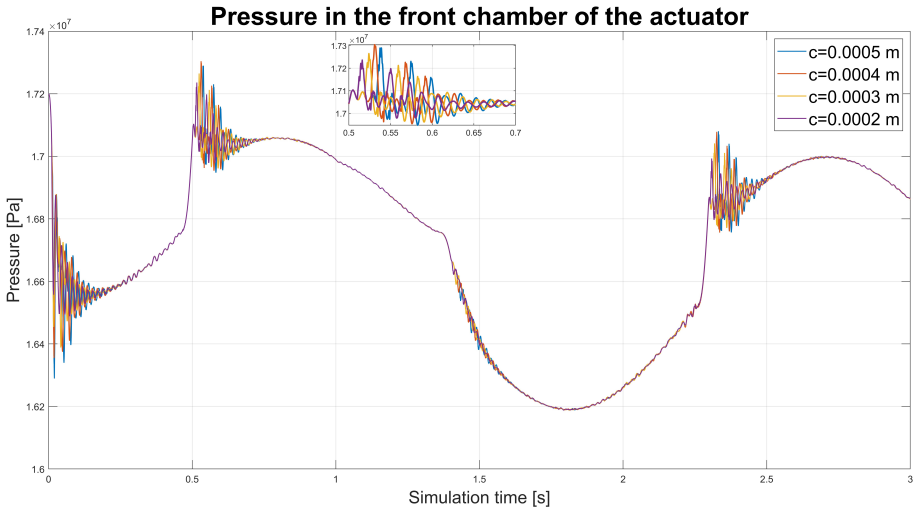


**Figure 6.18:** Front chamber pressure

the flow directed by the spool of the servovalve towards the actuator chambers or towards the reservoir. The trend of the flow towards the rear chamber is shown in Figure 6.20, where it can be seen that the flow increases during the extension phase while becoming negative, meaning the flow direction changes, during the retraction phase because the fluid will move from the actuator chamber to the system reservoir. There is not a significant difference in the flow trend with varying rod-end clearance. This is because liquids are nearly incompressible, so even a small increase in fluid volume results in a considerable increase in pressure in the actuator chamber. The trend of the flow in the front chamber of the actuator is opposite to that obtained for the rear chamber. As shown in Figure 6.21, the flow will be positive during the retraction phase of the actuator, meaning the flow will go into the chamber, while it will be negative during the extension phase of the actuator. Finally, the last parameter analyzed in this study is the position of the spool of the servovalve, the trend of which is shown in Figure 6.22. Just like for the flow rates, there are no substantial differences in the spool position as the rod-end

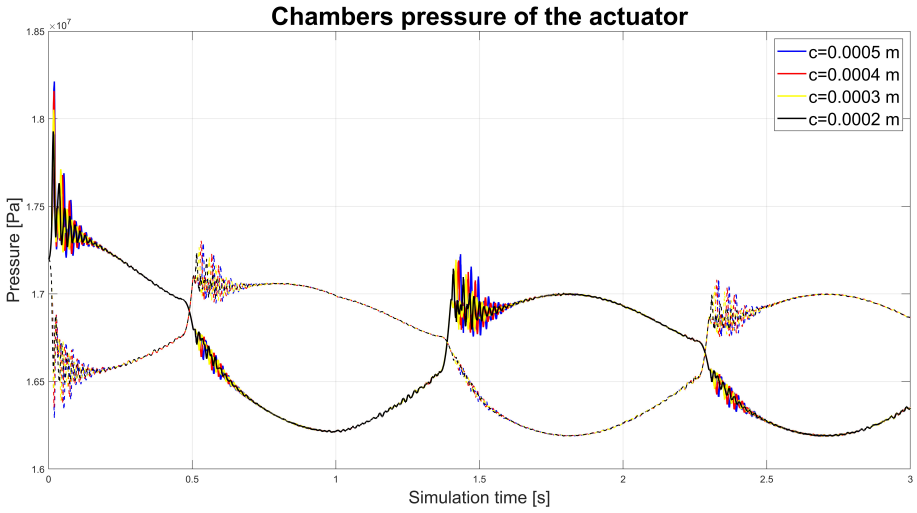


**Figure 6.19:** Chambers pressure of the actuator

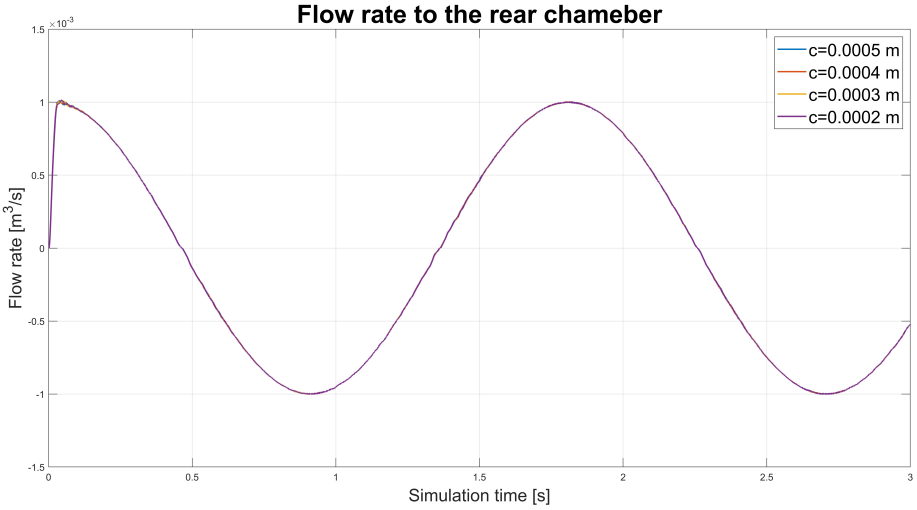


**Figure 6.20:** Flow rate in the rear chamber

clearance varies, which is expected since the flow rate does not vary significantly. Indeed, the position of the spool defines the flow rate. Therefore, if the flow rate varies only slightly, the spool position will also vary only slightly. From the figure, it can be observed that positive spool positions occur during the extension phase of the actuator's rod, while negative spool positions occur during the retraction phase. Thus, the trend of the spool position closely follows the trend of the flow rate into the rear chamber of the actuator.

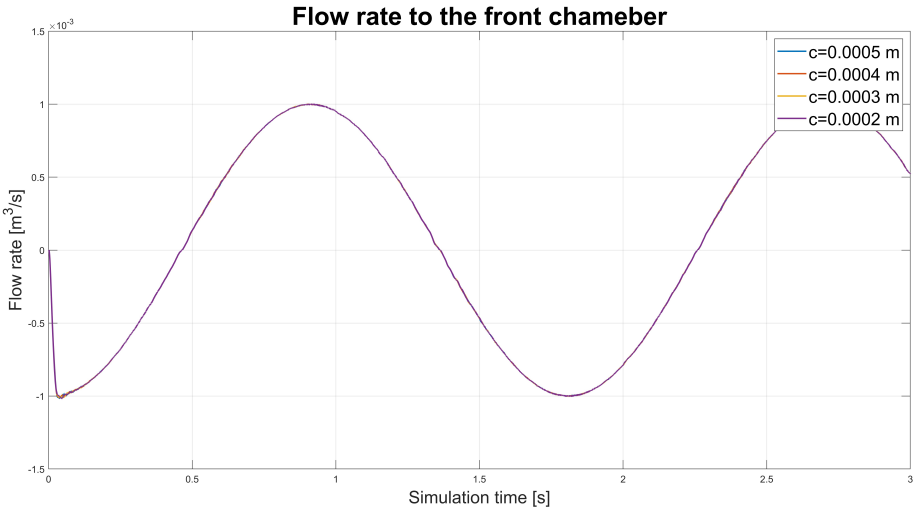


**Figure 6.21:** Flow rate in the front chamber

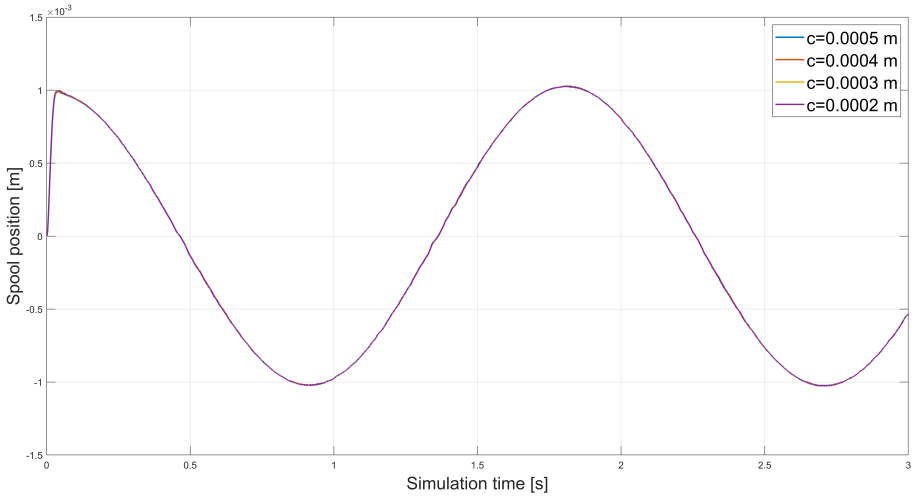


**Figure 6.22:** Servovalve spool position

### 6.3.2 Analysis as the applied force varies

The last analysis of the results that we decided to propose concerns the variation of the external force applied to the flight surface. So far, all the results have been obtained assuming that there is no air pressure on the flight surface. To have a more realistic simulation, it is necessary to simulate its influence as well. This analysis was not performed previously with only the rod-end model because most of

the damping in the system is due to the presence of an actuator. Therefore, without it, you would get a more unstable behavior that is harder to analyze. In reality, instead of applying a force, a moment was applied to the flight surface, first with a constant value to simplify the situation. Then, a moment proportional to the angle of the surface was applied. Applying a moment proportional to the angle of the flight surface is certainly more realistic because the air pressure generated will vary based on its inclination. First of all, it is necessary to show the trend of the position and velocity of the actuator, whose trends can be seen in Figure 6.23. The position output is very similar as the force varies. If you were to zoom in on the curve, you would see that as the applied moment increases, the maximum position reached by the actuator decreases. However, this is a minimal difference, approximately three orders of magnitude less than the actuator extension measurement. For the velocity trend, you can see that as the applied moment increases, there is more disturbance present at the beginning of the simulation. This is because the applied moment was applied in a step function, so the system needs time to settle. Immediately after, it

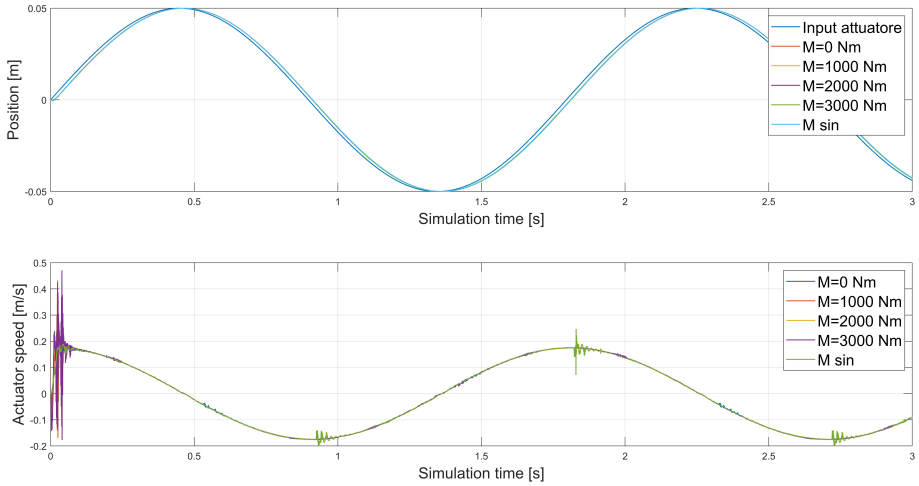


**Figure 6.23:** Actuator position and speed with different momentum

is useful to look at the trend of the contact force. In Figure 6.24, you can see the trend of the magnitude of the contact force for simplicity. However, this is sufficient to get a clear idea of the influence of the applied moment. From the figure, it can be seen that the contact force is always present when a constant external moment is applied. This is because the application of the moment causes the flight surface to tend to rotate clockwise, immediately bringing the inner sphere into contact with the outer sphere and remaining in contact until the end of the simulation. Even when the actuator transitions from the extension phase to the retraction phase, contact between the two spheres persists. This is because the moment has a greater

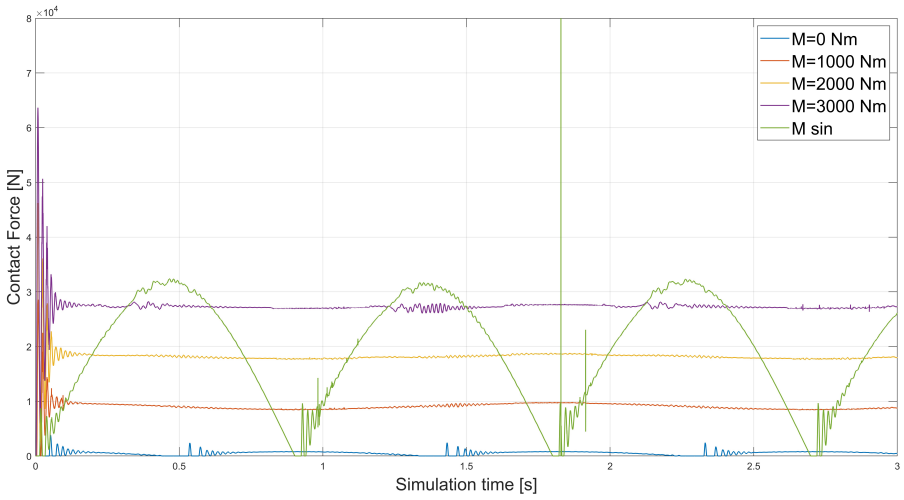


**Figure 6.24:** Contact force magnitude with different momentum

influence than the inertial force, which would tend to separate the two spheres during the motion reversal. The behavior just described does not occur with the moment applied proportionally to the angle of the surface. In this case, the two spheres remain in contact even after the motion reversal of the actuator. However, when the angle reaches zero, meaning the surface is in a horizontal position, the sign of the applied moment reverses. Consequently, the inner sphere moves in the opposite direction to come into contact with the outer sphere on the other half. The trend of the sinusoidal applied moment can be seen in Figure 6.25, from which the sign reversal of the moment is evident. Specifically, the applied moment always tends to counteract the deployment of the surface. Thus, if the surface rotates clockwise from the rest position, the applied moment will be counterclockwise and negative. Conversely, if the surface rotates counterclockwise, the moment will be clockwise and positive. All that has just been described is confirmed by the polar plot in Figure 6.26, which shows the relative position of the two spheres. This plot confirms the continuous presence of contact between the two spheres in the case of a constant applied moment. At higher applied moments, the only difference is the presence of greater eccentricity between the two spheres, which was also deducible from Figure 6.24, corresponding to greater penetration of the two bodies. In the case of applying a sinusoidal moment, the behavior of the rod end becomes clear when the applied moment changes sign. Indeed, it can be seen that the contact between the two spheres occurs in the other half of the outer sphere. The trend seen in the polar plot is confirmed by examining the force of the spring connected to the inner sphere and the force of the spring connected to the outer sphere in their three components. Looking at the trend of the force of the spring connecting the actuator

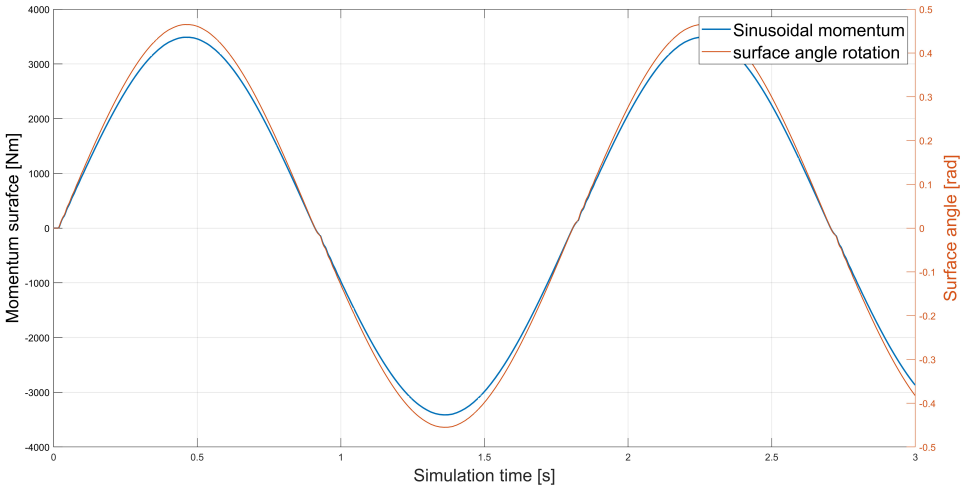


**Figure 6.25:** Sinusoidal momentum applied to the control surface

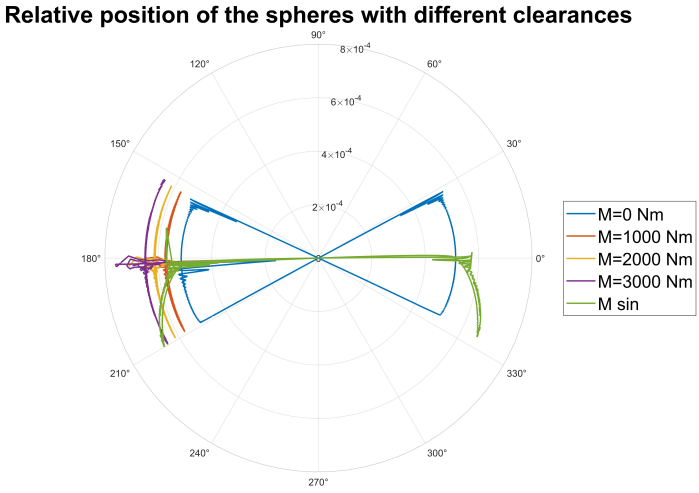


**Figure 6.26:** Polar force with different momentum

to the outer sphere in Figure 6.27 (the graph shows the trend obtained in one of the tests performed with different moments; otherwise, it would be difficult to read), it can be observed that the component along the x-axis of the force is always positive, while the component along the y-axis changes sign when the contact between the two spheres occurs in the upper half of the polar plot. The fact that the force along the x-axis is always positive also means that the spring is always compressed. The trend of the force of the spring connecting the inner sphere to the flight surface

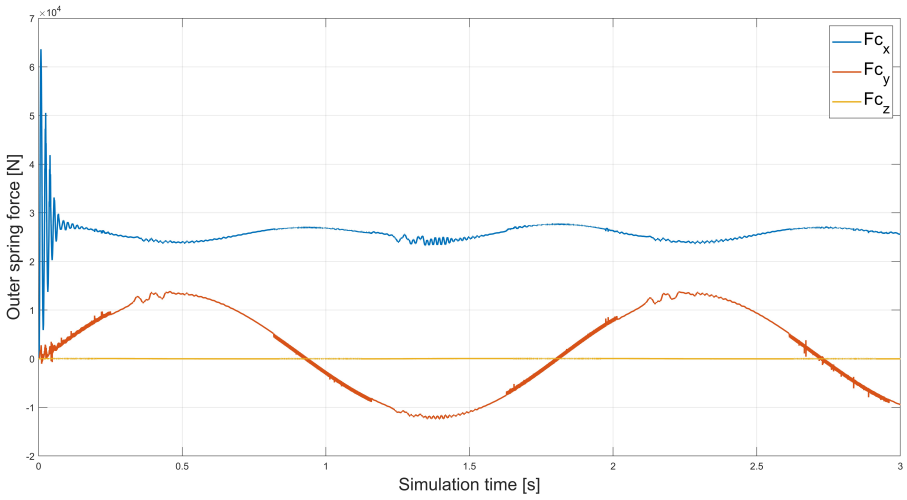


**Figure 6.27:** Actuator spring force with constant momentum

follows a behavior similar to that of the previous spring. However, the component along the x-axis will always be negative because, in this case, the compression of the spring is described by a negative force. The trend of the force can be observed in Figure number 6.28. In the final analysis, we present the graphs showing where

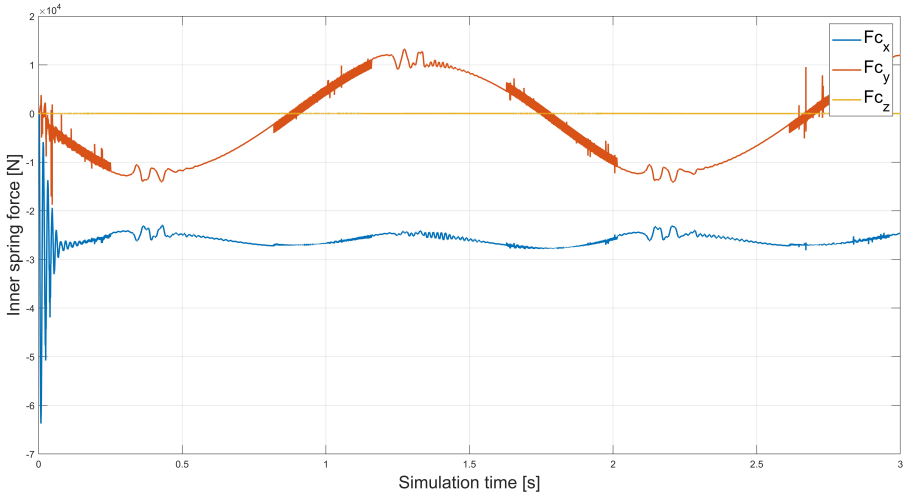


**Figure 6.28:** Surface spring force with constant momentum

the wear in the rod-end is localized. Unlike what was seen in Chapter 5, the wear in the presence of an external force will be located differently. With a constant

external moment, the wear is only localized in the left part of the polar plot, as the contact between the two spheres is present only in that area. The trend of wear can be seen in figure number 6.29. The trend of the contact force and the wear

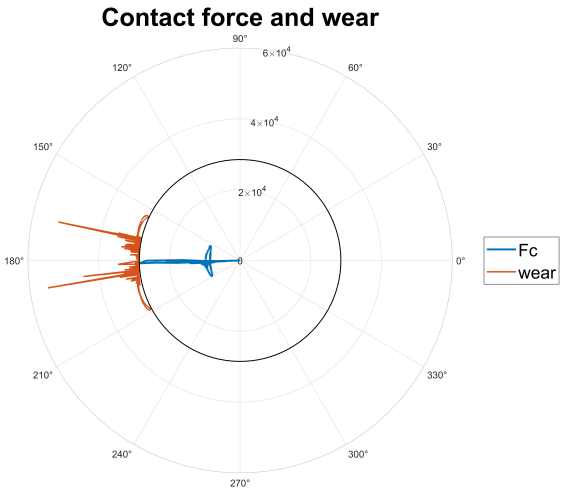


**Figure 6.29:** Polar plot with contact force ad a wear indicator

indicator is shown for only one constant moment value because the trend would be the same; only the magnitude of the contact force and consequently of the wear indicator would change. However, the maximum value of the contact force, as for the wear, would be located at the same theta coordinate on the polar plot. It is interesting to note that in this case, as in the case of Chapter 5, the maximum wear would not occur at the point where the contact force is maximum.

# Chapter 7

# Conclusion

Rod-ends play a crucial role in actuating flight control surfaces, thus modeling them is essential. Creating a model of the rod-end using any software is highly beneficial during testing. Initially, during experimentation, simulating the behavior of the mechanical component virtually proves invaluable, enabling the prompt identification of major errors and preventing the placement of a rod-end on the test bench that is already known not to meet test requirements. The aim of this thesis is to provide a model that simulates the behavior of the rod-end in such scenarios. The rod-end model developed for this thesis can be deemed universal, as only a few input parameters need to be altered to obtain a model of a rod-end with dimensions different from those used in the results section of this paper. The entire actuation part, including the connecting rod-crank mechanism with the two three-dimensional springs, is non-standardized in flight control surface actuation systems. However, the model's creation allows for the straightforward adjustment of the kinematic equations describing the position and velocity of the connecting rod and crank endpoints. The actuator is controlled by a jet-pipe valve, though control with a flapper-nozzle valve is easily implementable by merely substituting the jet-pipe equations with the flapper-nozzle equations. In light of this, the created model can be considered nearly "universal," except for a few modifications required based on the actuation system used to analyze the rod-end's behavior. With that said, undoubtedly, the model can undergo numerous improvements. This thesis serves as a continuation of a previous thesis where the rod-end model was two-dimensional, whereas in this thesis, a decision was made to model it in three dimensions for increased realism. Similar to the previous thesis, this one can also be expanded in various aspects. A critical aspect lacking in this model is a more accurate estimation of wear within the rod-end. The results section only includes a rudimentary method for wear calculation. To enhance the model, a more in-depth wear calculation could be developed, determining the amount of material removed and the specific area within the two bodies comprising the rod-end most affected.

For even more precise modeling, finite element contact modeling could be useful, providing real-time updates on wear and thus variable rod-end track geometry. A more thorough wear calculation is undoubtedly a development that could and should be pursued, as many breakdowns occur due to significant rod-end wear, leading to the removal of the solid lubricant layer and resulting in metal-to-metal contact.

# Appendix A

# Contact force

In this Appendix the article written by Lankarani e Nikravesh is analyzed; the contact force is one of the most important things of this thesis so it seemed necessary to delve deeper into the topic. In this thesis it has be chosen this contact force model because describe the contact in a more detailed manner as a trade-off, there is a higher computational costs.

The subject of the article is a so-called external impact, that is when two foreign bodies collide with each other. During the impact of the bodies there is an energy transfer process which is model using a parameter called "coefficient of restitution". This article follows the approach that the contact forces act in a continuous way. This means that the impact forces should be added to the equation of motion of the body, which is what is done in this thesis. The development of this contact force model starts from the Hertz contact model adding a damping contribute; the dissipated energy during the impact it is assumed to be due that an hysteretic damping intrinsic of the material of the two bodies which dissipate energy in the form of heat. Below there are the logical and mathematical steps leading to the definition of $\mu$ the "hysteresis damping factor".

As an example, in the discussion, is considered the contact between two sphere, as it is shown in the figure A.1; the two spheres have a velocity $V_i^{(-)}$ and $V_j^{(-)}$ at

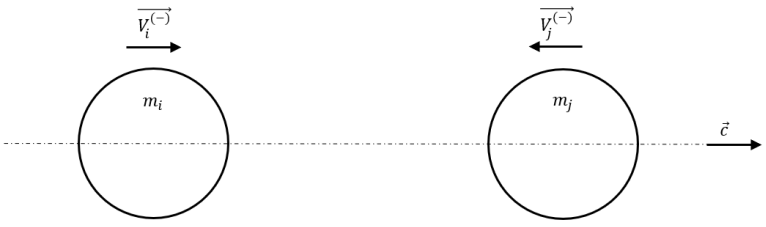


**Figure A.1:** Impact between two spheres

the time $t^{(-)}$ which is the instant immediately before the contact and a velocity $V_i^{(+)}$ and $V_j^{(+)}$ at the time $t^{(+)}$ immediately after the contact. The kinetic energy balance before and after the contact yields the energy loss during impact.

$$\begin{aligned}\Delta T &= T^{(-)} - T^{(+)} \\ &= \frac{1}{2}m_i\left\{\left[V_i^{(-)}\right]^2 - \left[V_i^{(+)}\right]^2\right\} + \frac{1}{2}m_j\left\{\left[V_j^{(-)}\right]^2 - \left[V_j^{(+)}\right]^2\right\}\end{aligned} \tag{A.1}$$

The coefficient of restitution is defined as "the ratio of relative departure velocity to the relative approach velocity of the spheres in the direction of impact" which in term of equation is:

$$e = -\frac{V_i^{(+)} - V_j^{(+)}}{V_i^{(-)} - V_j^{(-)}} \tag{A.2}$$

The linear momentum along the direction of contact is conserved due to the contact force is internal to the system.

$$m_i[V_i^{(-)} - V_i^{(+)}] + m_j[V_j^{(-)} - V_j^{(+)}] = 0 \tag{A.3}$$

So using the three equation number A.1, A.2 and A.3 the three unknown quantities $V_i^{(+)}$, $V_j^{(+)}$ and $\Delta T$ can be easily found:

$$V_i^{(+)} = \frac{1}{m_i + m_j}\left[\Big(m_i - em_j\Big)V_i^{(-)} + (1+e)m_jV_j^{(-)}\right] \tag{A.4}$$

$$V_j^{(+)} = \frac{1}{m_i + m_j}\left[\Big(m_j - em_i\Big)V_j^{(-)} + (1+e)m_iV_i^{(-)}\right] \tag{A.5}$$

$$\Delta T = \frac{m_im_j}{2(m_i + m_j)}\left[V_i^{(-)} + V_j^{(-)}\right]^2\Big(1 - e^2\Big) \tag{A.6}$$

To perform this contact model formulation it should be evaluate the indentation velocity $\dot{\delta}$ at any time during all the period of contact. Considering for now only the first phase of the contact and so only the compression phase the two spheres at the end of this phase have the same velocity; a part of the initial kinetic energy of the two sphere is transformed into elastic strain energy and another part is transformed into the kinetic energy of both the spheres moving towards with the same velocity, so the energy balance is as follows:

$$T^{(-)} = T^{(m)} + U^{(m)} \tag{A.7}$$

where $U^{(m)}$ is the maximum strain energy stored. The equation number A.7 is so:

$$\frac{1}{2}m_i\left[V_i^{(-)}\right]^2 + \frac{1}{2}m_j\left[V_j^{(-)}\right]^2 = \frac{1}{2}(m_i + m_j)\left[V_{ij}^{(m)}\right]^2 + U^m \tag{A.8}$$

Equalizing the equation number A.4 and A.5 the instantaneous velocity at the end of the compression phase became:

$$V_{ij}^{(m)} = \frac{1}{m_i + m_j}\left[m_j V_j^{(-)} + m_i V_i^{(-)}\right] \tag{A.9}$$

Now substituting all the expression in the equation number A.7 the maximum strain energy stored became:

$$U^{(m)} = \frac{m_i m_j}{2(m_i + m_j)}\left[\dot{\delta}^{(-)}\right]^2 \tag{A.10}$$

The absorbed strain energy is equal to the work done during all the compression phase by the contact force which for simplicity is considered equal to the Hertz contact force model and became:

$$U^{(m)} = \frac{K}{n+1}\delta_m^{n+1} \tag{A.11}$$

Now equalizing the equation number A.10 and A.11 it can be found the initial indentation velocity:

$$\left[\dot{\delta}^{(-)}\right]^2 = \frac{2(m_i + m_j)K}{m_i m_j (n+1)}\delta_m^{n+1} \tag{A.12}$$

Knowing the indentation velocity for each time during the contact is possible to calculate also the energy loss by the damping function of the this new contact force model. In this analysis it's assumed that the dissipated energy during the contact is small compared to the strain energy, this leads to have the restitution coefficient close to unity and it can be also assumed that the indentation velocity can be approximate by the same expression during the two phase of the contact. So the dissipated energy can be evaluated form the work done by the damping component of the contact force and it's expressed in the following way:

$$\Delta T = \oint D\,\dot{\delta}\,d\delta = \oint \mu\,\delta^n\,\dot{\delta}\,d\delta \tag{A.13}$$

Making all the proper calculus the energy loss formulation became:

$$\Delta T \approx \frac{4\mu}{3(n+1)}\left[\frac{2(m_i + m_j)K}{m_i m_j (n+1}\right]^{1/2}\left[\delta_m\right]^{3(n+1)/2} \tag{A.14}$$

The maximum indentation can be expressed in term of the initial indentation velocity and the equation of the energy loss became:

$$\Delta T \approx \frac{2\mu m_i m_j}{3K(m_i + m_j)}\left[\dot{\delta}^{(-)}\right]^3 \tag{A.15}$$

Finally from the previous equation it can be found $\mu$ the "hysteresis damping factor" comparing the equation with the equation number A.6 which is equal to:

$$\mu = \frac{3K(1-e^2)}{4\dot{\delta}^{(-)}} \tag{A.16}$$

which is the expression used in the chapter number 4.

# Bibliography


[1] Wayne Scraba. «"CRITICAL COMPONENTS" "What You Need To Know About Rod Ends  Spherical Bearings"». In: () (cit. on p. 7).

[2] Antonio Carlo Bertolino, Andrea De Martin, Giovanni Jacazio, and Massimo Sorli. «Design and Preliminary Performance Assessment of a PHM System for Electromechanical Flight Control Actuators». In: *Aerospace* (2023) (cit. on p. 7).

[3] Massimo SORLI Alberto BACCI Dott Andrea DE MARTIN. «High-fidelity modeling of degraded rod-end for flight control actuators-analysis and preliminary PHM study». POLITECNICO DI TORINO DEPARTMENT OF MECHANICAL and AEROSPACE ENGINEERING, 2020 (cit. on p. 7).

[4] Zhanshan Wang, Yulin Yang, Xiping Liu, and Shijun Huang. «Design and movement trail analysis of a life testing machine for self-lubricating rod end spherical plain bearing of a helicopter». In: *Journal of Advanced Mechanical Design, Systems and Manufacturing* (2016) (cit. on p. 8).

[5] Edward J Nagy. «Wear-indicating rod-end bearing». In: (1976) (cit. on p. 10).

[6] Zhang Shuai, Cui Yongcun, Hu Zhonghui, Yang Xiaomin, Li Yan, and Deng Sier. «Thermal-stress-wear coupled characteristics of oil seal in airframe rod end-bearing». In: (2021) (cit. on p. 10).

[7] Byung Chul Kim, Dong Chang Park, Hak Sung Kim, and Dai Gil Lee. «Development of composite spherical bearing». In: *Composite Structures* (2006) (cit. on p. 10).

[8] Osman Asi and Önder Yeşil. «Failure analysis of an aircraft nose landing gear piston rod end». In: *Engineering Failure Analysis* (2013) (cit. on p. 11).

[9] Evaldas Narvydas, Romualdas Dundulis, and Nomeda Puodžiūnienė. «Rod End Stress Analysis for Hydraulic Cylinder of Live Floor Conveying System». In: *Mechanics* (2020) (cit. on p. 11).

[10] Qiang Tian, Paulo Flores, and Hamid M. Lankarani. *A comprehensive survey of the analytical, numerical and experimental methodologies for dynamics of multibody mechanical systems with clearance or imperfect joints*. 2018 (cit. on p. 13).

[11] Heinrich Hertz, Philipp Lenard, Hermann von Helmholtz, et al. *Gesammelte Werke: Vol. 1: Schriften vermischten Inhalts*. 1895 (cit. on p. 15).

[12] H M Lankarani and P E Nikravesh. *A Contact Force Model With Hysteresis Damping for Impact Analysis of Multibody Systems*. 1990 (cit. on p. 17).

[13] Antonio Carlo Bertolino, Massimo Sorli, F Braghin, Di Milano, and G Figliolini. *High Fidelity Model of Ball Screws to Support Model-based Health Monitoring*. 2020 (cit. on p. 17).

[14] N. Jeremy Kasdin and Derek A. Paley. *Engineering Dynamics: A Comprehensive Introduction*. Princeton University Press, 2011 (cit. on p. 27).

[15] Andrea De Martin, Andrea Dellacasa, and Giovanni Jacazio. «HIGH-FIDELITY MODEL OF ELECTRO-HYDRAULIC ACTUATORS FOR PRIMARY FLIGHT CONTROL SYSTEMS». In: () (cit. on p. 67).

[16] Sylvain Autin, Andrea De Martin, Giovanni Jacazio, Jérôme Socheleau, and George Vachtsevanos. «Results of a feasibility study of a prognostic system for electro-hydraulic flight control actuators». In: *International Journal of Prognostics and Health Management* (2021) (cit. on p. 67).